NASA/TM—2006-213966

High-Strain-Rate Compression Testing of Ice

Mostafa Shazly and Vikas Prakash
Case Western Reserve University, Cleveland, Ohio

Bradley A. Lerch
Glenn Research Center, Cleveland, Ohio

January 2006

The NASA STI Program Office . . . in Profile

Since its founding, NASA has been dedicated to the advancement of aeronautics and space science. The NASA Scientific and Technical Information (STI) Program Office plays a key part in helping NASA maintain this important role.

The NASA STI Program Office is operated by Langley Research Center, the Lead Center for NASA's scientific and technical information. The NASA STI Program Office provides access to the NASA STI Database, the largest collection of aeronautical and space science STI in the world. The Program Office is also NASA's institutional mechanism for disseminating the results of its research and development activities. These results are published by NASA in the NASA STI Report Series, which includes the following report types:

- TECHNICAL PUBLICATION. Reports of completed research or a major significant phase of research that present the results of NASA programs and include extensive data or theoretical analysis. Includes compilations of significant scientific and technical data and information deemed to be of continuing reference value. NASA's counterpart of peer-reviewed formal professional papers but has less stringent limitations on manuscript length and extent of graphic presentations.

- TECHNICAL MEMORANDUM. Scientific and technical findings that are preliminary or of specialized interest, e.g., quick release reports, working papers, and bibliographies that contain minimal annotation. Does not contain extensive analysis.

- CONTRACTOR REPORT. Scientific and technical findings by NASA-sponsored contractors and grantees.

- CONFERENCE PUBLICATION. Collected papers from scientific and technical conferences, symposia, seminars, or other meetings sponsored or cosponsored by NASA.

- SPECIAL PUBLICATION. Scientific, technical, or historical information from NASA programs, projects, and missions, often concerned with subjects having substantial public interest.

- TECHNICAL TRANSLATION. English-language translations of foreign scientific and technical material pertinent to NASA's mission.

Specialized services that complement the STI Program Office's diverse offerings include creating custom thesauri, building customized databases, organizing and publishing research results . . . even providing videos.

For more information about the NASA STI Program Office, see the following:

- Access the NASA STI Program Home Page at ***http://www.sti.nasa.gov***

- E-mail your question via the Internet to help@sti.nasa.gov

- Fax your question to the NASA Access Help Desk at 301–621–0134

- Telephone the NASA Access Help Desk at 301–621–0390

- Write to:
  NASA Access Help Desk
  NASA Center for AeroSpace Information
  7121 Standard Drive
  Hanover, MD 21076

NASA/TM—2006-213966

High-Strain-Rate Compression Testing of Ice

Mostafa Shazly and Vikas Prakash
Case Western Reserve University, Cleveland, Ohio

Bradley A. Lerch
Glenn Research Center, Cleveland, Ohio

National Aeronautics and
Space Administration

Glenn Research Center

January 2006

Acknowledgments

The authors would like to acknowledge financial support from NASA Glenn Research Center under NASA Contract Number NNC05VA03P. The authors would also like to thank E.M. Schulson and the Ice Research Laboratory at Dartmouth College, Hanover, New Hampshire, for providing ice samples, microstructural analysis of the ice specimens, and many helpful discussions.

Available from

NASA Center for Aerospace Information
7121 Standard Drive
Hanover, MD 21076

National Technical Information Service
5285 Port Royal Road
Springfield, VA 22100

Available electronically at http://gltrs.grc.nasa.gov

High-Strain-Rate Compression Testing of Ice

Mostafa Shazly and Vikas Prakash
Department of Mechanical and Aerospace Engineering
Case Western Reserve University
Cleveland, Ohio 44106–7222

Bradley A. Lerch
National Aeronautics and Space Administration
Glenn Research Center
Cleveland, Ohio 44135

Summary

In the present study a modified split Hopkinson pressure bar (SHPB) was employed to study the effect of strain rate on the dynamic material response of ice. Disk-shaped ice specimens with flat, parallel end faces were either provided by Dartmouth College (Hanover, NH) or grown at Case Western Reserve University (Cleveland, OH). The SHPB was adapted to perform tests at high strain rates in the range 60 to 1400 s^{-1} at test temperatures of –10 and –30 °C. Experimental results showed that the strength of ice increases with increasing strain rates and this occurs over a change in strain rate of five orders of magnitude. Under these strain rate conditions the ice microstructure has a slight influence on the strength, but it is much less than the influence it has under quasi-static loading conditions. End constraint and frictional effects do not influence the compression tests like they do at slower strain rates, and therefore the diameter/thickness ratio of the samples is not as critical. The strength of ice at high strain rates was found to increase with decreasing test temperatures. Ice has been identified as a potential source of debris to impact the shuttle; data presented in this report can be used to validate and/or develop material models for ice impact analyses for shuttle Return to Flight efforts.

Introduction

Since the catastrophic breakup of the Space Shuttle Columbia, NASA has been active in classifying potentially deleterious debris sources and their destructive capability due to impact. Ice has been identified as one of the potential sources of debris. In order to better understand the severity of ice impacts on aero frames and structures, and to obtain the high-strain-rate behavior of ice, an experimental investigation was undertaken at Case Western Reserve University (CWRU, Cleveland, OH) in close collaboration with researchers at the NASA Glenn Research Center (Cleveland, OH). The key question under investigation was how the dynamic compressive strength of ice varies with the relevant loading rates. Besides providing fundamental information on the dynamic properties of ice, the data from the present study can also be used to validate and/or develop new material models for ice impact analyses for the Shuttle Return to Flight efforts.

There is a large amount of work in the literature characterizing the compressive and tensile strength (refs. 1 to 6), and the fracture toughness (refs. 5 to 9) of ice either in single-crystal or polycrystalline forms. However, most of these studies have focused on the mechanical behavior in the creep and quasi-static deformation regimes. At higher strain rates, relatively few studies exist, and these typically only cover the strain rate regime from 10 to 100 s^{-1} (refs. 10 to 12). However, in events such as ice-structure interactions, ice drilling and crushing, and high-speed ice impacts, the strain rates in ice are much higher than those considered in the studies thus far. Moreover, results of studies conducted at strain rates of 10 to 100 s^{-1} (refs. 10 to 12) show counterintuitive results, at least based on the known strain-rate behavior of common structural materials. The studies by Dutta (ref. 10) and Dutta et al. (ref. 12) suggest that the strength of ice at high strain rates is lower than that obtained in the quasi-static deformation regime (strain rates between 10^{-2} and 10^{-3} s^{-1}). The study by Jones (ref. 11), however, does not show the same trend in

the behavior of ice with increasing strain rates. Although results of these studies (refs. 10 and 12) show ice following the behavior known as the "brittle to ductile behavior" at strain rates higher than 10^{-3} s^{-1} (ref. 13), they do not explain the increase in impact forces measured at the higher impact velocities (ref. 14). Additionally, extrapolations of the quasi-static compressive strength to higher strain rates do not provide clear trends as to whether the strength of ice increases, decreases or remains the same as the strain rate increases from the quasi-static to the dynamic range. Moreover, the quasi-static results indicated that the strengths were highly microstructural dependent, and it was unknown if this trend would continue in the high-strain-rate regime. These issues are addressed in the current work.

The findings are described in this report. The report and raw test sample data files have been placed on the Orbiter TPS Impact Testing Data Archive Web site at NASA Johnson Space Center. The link for the Web site is http://hitf.jsc.nasa.gov/hitfpub/archive/home.cfm. The data can be found under the "series 50" option "Characterization of ice used for impact testing."

A list of the symbols used in this report has been placed in appendix A to aid the reader.

Experimental Work

In an effort to explore the strength of ice at elevated strain rates, an experimental study was conducted at CWRU in close collaboration with scientists at NASA Glenn. In this study, the conventional split Hopkinson pressure bar (SHPB) was modified to accommodate low-temperature testing of ice at elevated strain rates. Disk-shaped ice specimens, with end faces that are flat and parallel, were provided by Dartmouth College (Hanover, NH) and/or grown at CWRU. The effects of strain rate, sample size, test conditions, and temperature on the strength of ice were investigated.

Low-Temperature Split Hopkinson Pressure Bar Facility

A split Hopkinson pressure bar (SHPB) was employed to conduct the high-strain-rate compression tests. A schematic of the SHPB facility at CWRU is shown in figure 1. The facility comprises a striker bar, an incident bar, and a transmitter bar. All the bars are made from 19.05-mm-diameter high-strength 7075–T6 aluminum alloy having a nominal yield strength of 500 MPa. Striker bars with lengths of 75 and 152 mm were used in the present study. The incident and transmitter bars were approximately 1.8 m long. The striker bar is accelerated using an air-operated gas gun. A pair of BLH SPB3–18–100–U1 semiconductor strain gages (Vishay Intertechnology, Inc., Malvern, PA) are strategically attached to the incident and transmitter bars and are used in combination with a Wheatstone bridge circuit connected with a Tektronix 5A22N differential amplifier (Tektronix, Inc., Beaverton, OR) and a Tektronix TDS 420 digital oscilloscope to monitor the strain pulses during the test. The impact velocity of the striker bar was varied between 2 m/s and 14 m/s so as to obtain strain rates in the range 60 s^{-1} to 1400 s^{-1}. The theory and analysis of SHPB is described in the following section. To better understand the failure process of ice, a high-speed camera, Hadland IMACON 200,[1] with a maximum framing rate capability of 200 million frames per second was used to image the failure process.

To conduct the low-temperature experiments, a cooling chamber (figs. 1 to 3) was designed and built at CWRU. The chamber was built from acrylic plates having a thickness of 31.75 mm to maximize insulation efficiency and maintain the subzero temperatures in the chamber. A 3/8-in. standard copper tube was shaped in a coil form and immersed in liquid nitrogen in a Dewar (fig. 3). One end of the coil was connected to a nitrogen gas or air tank while the other end is shaped into a larger coil to surround the SHPB bars and the ice specimen in the cooling chamber. The coil carries the cooled air to the cooling chamber and helps to maintain it at the desired subambient temperatures. The temperature inside the chamber was monitored by a 0.015-in.-diameter chromel-alumel wire placed in close proximity to the specimen. Circulation of the cooled air within the cooling chamber helps to maintain a uniform temperature. The test temperatures were –10 and –30 °C.

[1] Hadland Photonics, Ltd. (Tring, UK) was acquired by DRS Technologies, Inc. (Parsippany, NJ) and is now DRS Hadland, Ltd.

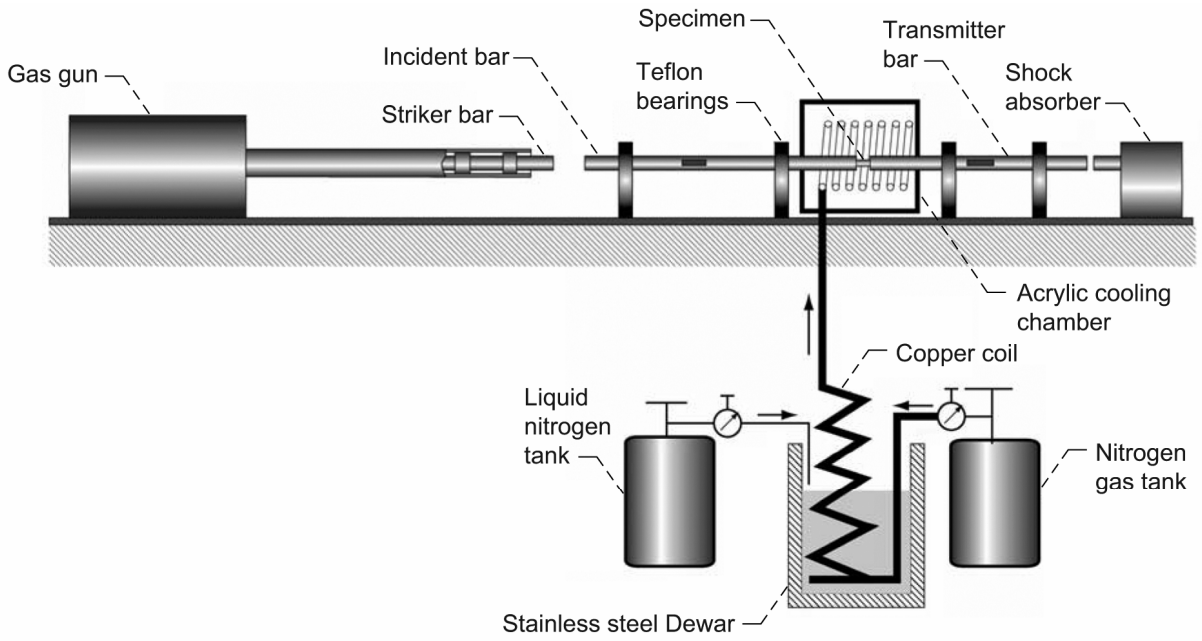

Figure 1.— Low-temperature split Hopkinson pressure bar (SHPB) facility at Case Western Reserve University. Teflon is a trademark of DuPont, Wilmington, DE.

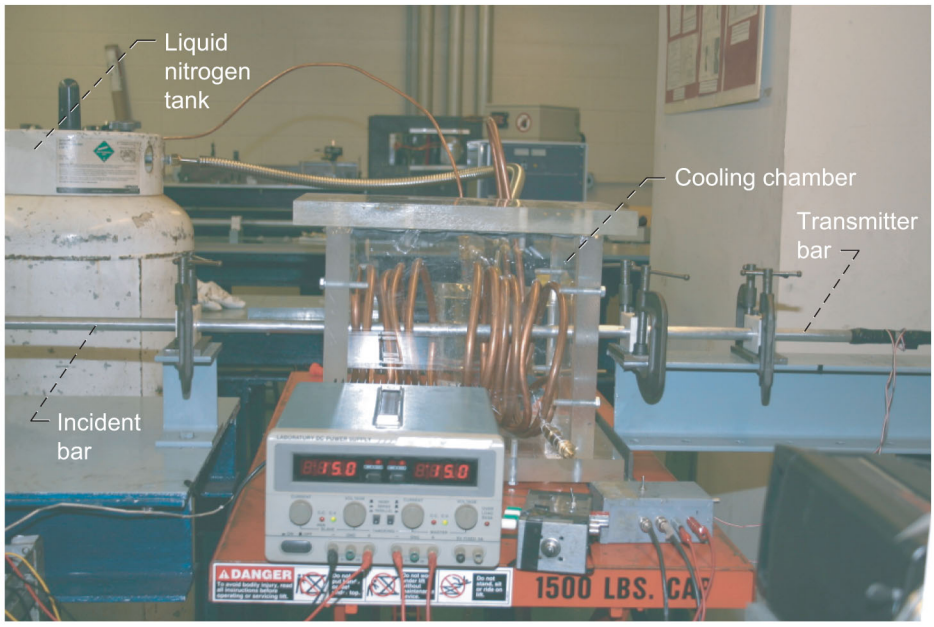

Figure 2.—Cooling chamber assembly along with SHPB setup.

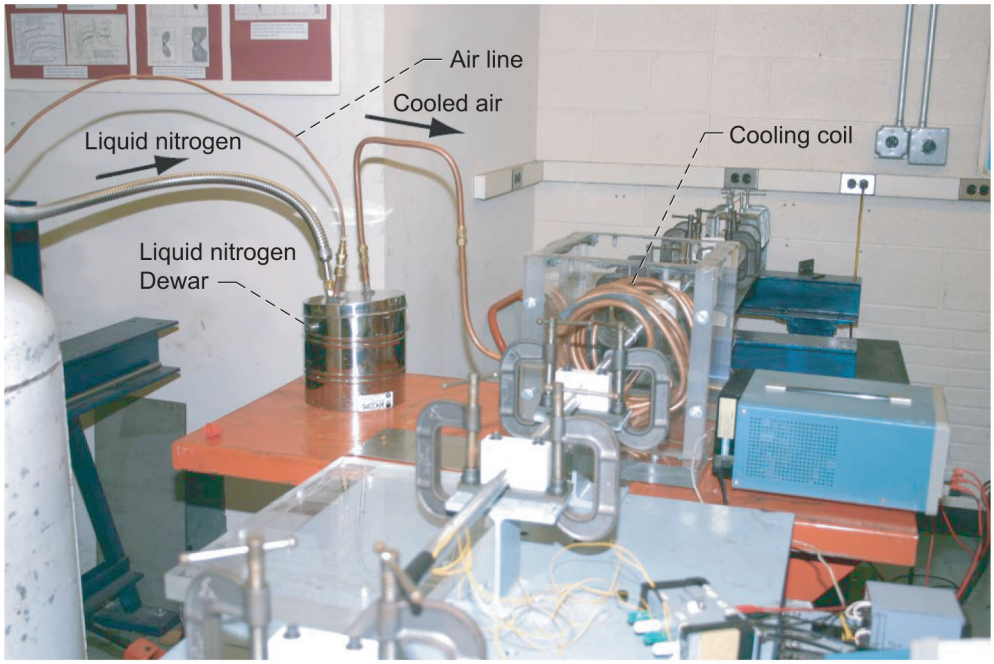

Figure 3.—Cooling chamber assembly showing flow of air and liquid nitrogen.

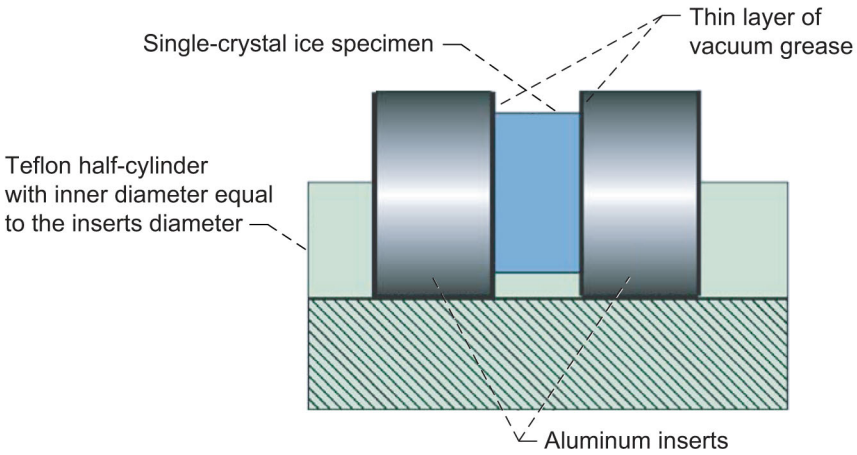

Figure 4.—Ice specimen and aluminum insert assembly prior to testing. Teflon is a trademark of DuPont, Wilmington, DE.

In all experiments, copper pulse shapers were employed to promote attaining dynamic equilibrium conditions within the specimen; these dynamic equilibrium conditions are essential to achieve constant strain rates during the dynamic deformation process. The thickness of the copper shim that was employed was approximately 0.25 mm. The shape of the shim was a square, with lateral dimensions depending on the strain rate that was desired. For experiments performed on premachined single-crystal ice specimens, the specimen was placed between two aluminum inserts (see fig. 4) of the same material and diameter as the bars used in the SHPBs. Inserts were held by a Teflon (DuPont, Wilmington, DE) fixture for ease of handling. The procedure for assembly is shown in figure 5. The assembly of the ice disk and the inserts was transported from the freezer to the test rig in a cryocontainer. A thin layer of vacuum grease was used between the ice specimen and the inserts in order to minimize friction, and hence the end constraint, during testing and also to hold the ice sample in place during mounting between the SHPB bars. Stress-strain curves are presented for the tests, where stress and strain are represented as engineering values.

Figure 5.—Procedure for ice specimen pre-assembly with SHPB inserts. (a) Two aluminum inserts are positioned on Teflon (DuPont, Wilmington, DE) half-cylinder. (b) Ice specimen is taken out with tweezers and placed between inserts. (c) Final assembly.

Theory of SHPB

The theory behind the SHPB operation relies on the one-dimensional wave analysis (ref. 15). The governing equation for wave propagation in a thin long rod is given by the second order partial differential equation

$$\frac{\partial^2 u}{\partial x^2} = \frac{1}{c_b}\frac{\partial^2 u}{\partial t^2} \tag{1}$$

where u is displacement, x is axial position along the sample, t is time, and $c_b = \sqrt{E/\rho}$ is the longitudinal wave speed expressed in terms of Youngs modulus E and density ρ of the bar.

The solution of this equation by D'Alembert (ref. 16) is given by

$$u(x,t) = \mathrm{f}(x - c_b t) + \mathrm{g}(x + c_b t) \tag{2}$$

where the functions f and g represent pressure waves traveling to the right and the left, respectively.

The strain ε and displacement rate $\dot{u}$ are then simply the derivative of the displacement with respect to x and t, respectively; that is,

$$\varepsilon = \mathrm{f}' + \mathrm{g}' = \varepsilon_i + \varepsilon_r \tag{3}$$

and

$$\dot{u} = c_b\left(-\mathrm{f}' + \mathrm{g}'\right) = c_b\left(-\varepsilon_i + \varepsilon_r\right) \tag{4}$$

In equations (3) and (4) ε_i and ε_r are the incident and reflected strain signals, respectively.

Figure 6 illustrates the displacements and forces generated on the specimen by the test. In view of equation (4), the displacement of the left end of the sample u_1 is given by

$$u_1 = c_b \int_0^t \left(-\varepsilon_i + \varepsilon_r\right) \mathrm{d}t \tag{5}$$

The transmitted wave system and the displacement of the right end of the sample u_2 are given by

$$u_2(x,t) = \mathrm{h}(x - c_b t) \tag{6}$$

where h is a wave traveling to the right.

Similarly, the transmitted strain signal ε_t is given by

$$\varepsilon_t = \mathrm{h}'(x - c_b t) \tag{7}$$

and

$$\dot{u} = -c_b\, \mathrm{h}'(x - c_b t) = -c_b \varepsilon_t \tag{8}$$

The displacement u_2 is then given by

$$u_2 = -c_b \int_0^t \varepsilon_t \, \mathrm{d}t \tag{9}$$

In view of equations (5) and (9), the average strain in the specimen ε_s is given by

$$\varepsilon_s = \frac{u_2 - u_1}{T_o} = \frac{c_b}{T_o} \int_0^t \left(-\varepsilon_t + \varepsilon_i - \varepsilon_r\right) \mathrm{d}t \tag{10}$$

where T_o is the original specimen thickness.

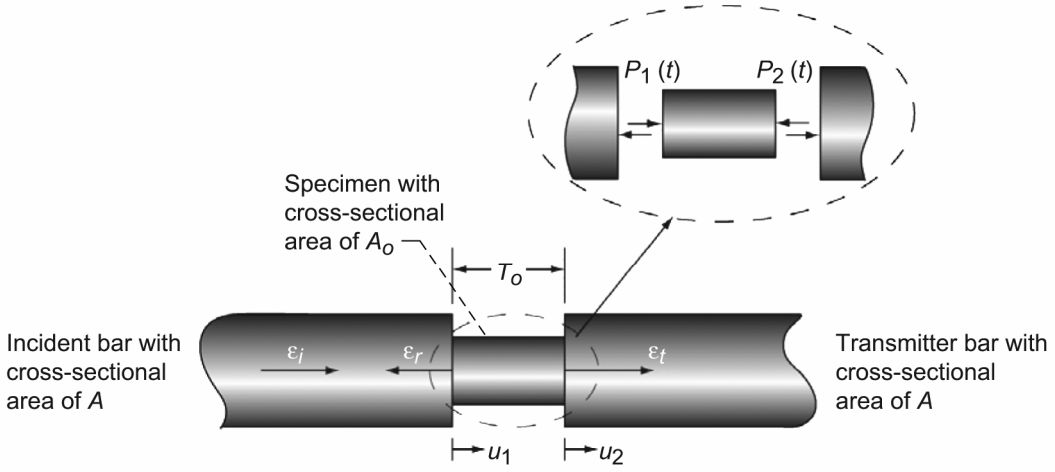

Figure 6.—Displacements u and forces P generated during SHPB test. T_o is original specimen thickness. ε_i, ε_r, and ε_t are incident, reflected, and transmitted strain signals, respectively.

The forces P_1 and P_2 on the left and the right faces of the specimen, respectively, are given by

$$P_1 = AE(\varepsilon_i + \varepsilon_r) \tag{11a}$$

$$P_2 = AE\varepsilon_t \tag{11b}$$

where A is the cross-sectional area of the incident and transmitted bars. After a few reverberations, the wave propagation effects within the specimen become negligibly small, such that $P_1 = P_2$.

It then follows that $\varepsilon_i + \varepsilon_r = \varepsilon_t$, so that the strain rate, strain, and stress in the specimen are given by

$$\dot{\varepsilon}_s(t) = \frac{2c_b}{T_o}\varepsilon_r \tag{12}$$

$$\varepsilon_s(t) = -\frac{2c_b}{T_o}\int_0^t \varepsilon_r \, \mathrm{d}t \tag{13}$$

$$\sigma_s(t) = \frac{P_1}{A_o} = \frac{P_2}{A_o} = \frac{AE\varepsilon_t(t)}{A_o} \tag{14}$$

where A_o is the original cross-sectional area of the specimen.

In a typical SHPB experiment, the strain gage stations attached to the incident and transmitted bars record the incident signal ε_i, the reflected signal ε_r, and transmitted signal ε_t. An in-house MATLAB program (The Mathworks, Inc., Natick, MA) is then used to filter the high-frequency noise and construct the stress-strain data from the raw data. The input parameters to the program are elastic properties of the incident and transmitted bars (Young's modulus and density), the dimensions of the specimen (diameter and thickness), and the shunt calibration of the strain gage stations.

Ice Specimen Geometry and Specimen Preparation Procedures

The ice specimens used in the present study were either single-crystal ice provided by the Ice Research Laboratory at Dartmouth College or polycrystalline ice samples grown at CWRU. The samples provided by Dartmouth College were machined out of cylinders of ice manufactured by Ice Culture, Inc. (Hensall, Ontario, Canada). The nominal diameter of the disk samples was in the range 17.5 to 18.5 mm. Although the specimens were not exactly cylindrical, the diameter was calculated based on the specimen weight and measured thickness. The specimens had a thickness of 5.0 to 9.0 mm, and the impact faces were milled parallel to within 0.076 mm. The samples were shipped from Dartmouth College to CWRU in containers packed with dry ice and stored upon arrival in a freezer at –15 °C.

The ice specimens made at CWRU were grown between two flat aluminum inserts, as shown in figure 7. The inserts were spaced at a predetermined distance and then were wrapped with masking tape. Next, a small hole was made in the masking tape to act as a water feeder to fill the compartment between the two inserts. The hole also acted as a breather to drain overflowed water during freezing. The whole assembly was then placed inside a freezer at the desired temperature. The subsequent ice nucleation and growth process required approximately 30 min. before the samples were taken out of the freezer for testing. De-ionized sodium-free water was used to make the ice samples. Due to the high conductivity of the aluminum inserts, ice crystals initiated simultaneously from the faces of the aluminum inserts and grew towards the center of the compartment, as illustrated schematically in figure 7. This growth process resulted in a clear but noticeable interface in the midplane of the ice specimens; the effect of this interface on the dynamic compression strength of ice is expected to be negligible. However, as a result of the

midplane porosity these samples were very weak in tension. Longer specimens made by following this technique split at the midplane during handling, as shown in figure 8.

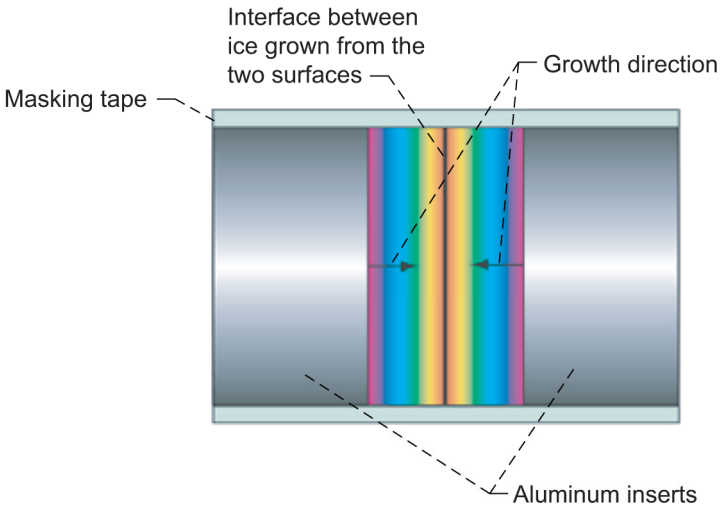

Figure 7.—Freezing process in ice specimen assembly created at Case Western Reserve University.

Figure 8.—Long ice specimens failed at midplane upon handling.

Experimental Results

Microstructure of Ice Specimens

The microstructure of the ice supplied by Dartmouth College was single crystalline containing a lot of subgrain boundaries (ref. 1). Figure 9 shows the birefringent pattern of a typical ice disk providing evidence that the disks were essentially single crystalline. No effort was made to orient the ice (i.e., relate the crystal structure to the axes of the disk sample). It has been shown (ref. 17) under quasi-static compression loading that the orientation of single-crystal ice can affect the strength by as much as a factor of 3. The birefringent pattern for each single-crystal ice sample tested in the present study is shown in appendix B.

The ice samples grown at CWRU were multigrained structures as shown in figure 10. Ice crystals nucleated on the aluminum inserts creating small equiaxed grains up to a diameter of 1.5 mm. As freezing continued, the grains grew from both sides with final freezing occurring at the midpoint. This created a zone of small bubbles in the middle, which appeared as a cloudy area. The ice at the ends of the sample was clear. The grain size of the growth grains was large, being approximately 3 mm in diameter and 5 mm in length for the longest grain. Transverse sections (fig. 10(b)) indicated that the large grains had an extensive substructure.

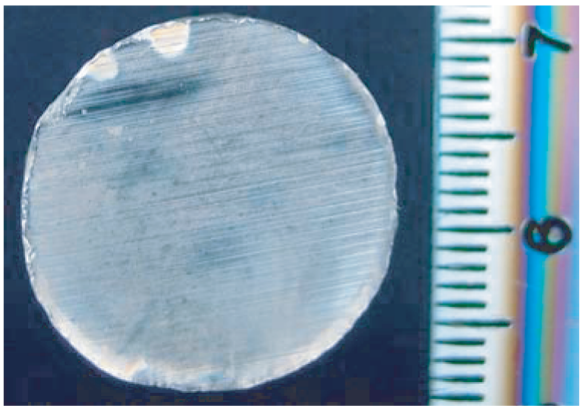

Figure 9.—Single-crystal ice specimen obtained from Dartmouth University (Hanover, NH). Scale in millimeters.

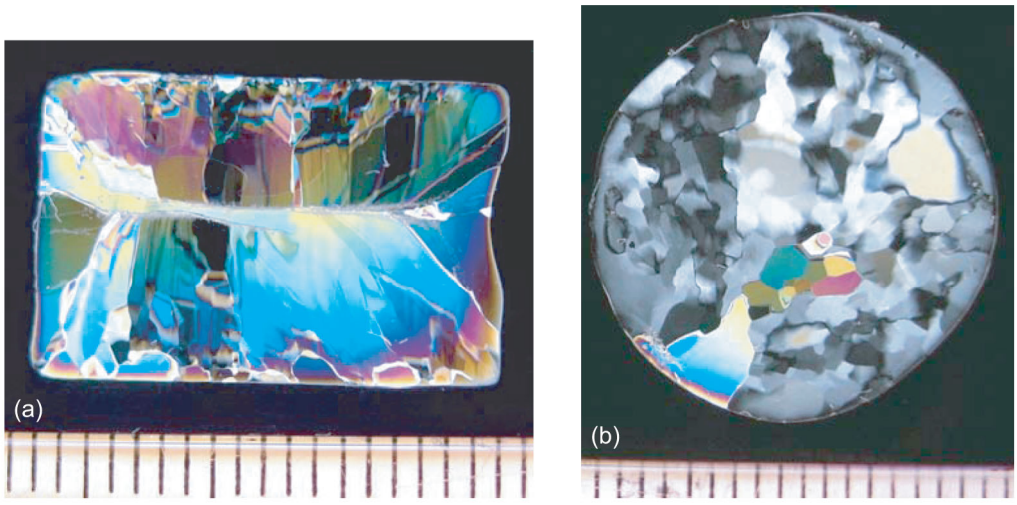

Figure 10.—Structure of multigrained ice specimen from Case Western Reserve University (Cleveland, OH). Scale in millimeters. (a) Longitudinal section. (b) Transverse section.

Stress Equilibrium and Nearly Constant Strain Rate Experiments

Based on the available literature (ref. 18), ice has an average Young's modulus of 10.0 GPa and an approximate density of 1000 kg/m^3. These values give a longitudinal elastic wave speed of 3162 m/sec. As pointed out by Davies and Hunter (ref. 19), the stress state equilibrates within the specimen after approximately π reverberations of the stress pulse within the specimen, that is

$$t_{\text{equil}} = \frac{\pi T}{C} \tag{15}$$

where T is the specimen thickness and C is the longitudinal wave speed in ice.

In view of equation (15), for the experiments conducted in the present study, the 8-, 5-, and the 2.3-mm-thick ice specimens will require approximately 8, 5, and 2.3 μs, respectively, to reach equilibrium conditions. Based on this analysis, the times for the attainment of maximum stress in the ice specimens is always greater than those required to reach an equilibrium state of stress within the specimen. This condition was facilitated by using copper pulse shapers to shape (increase) the rise time of the incident pulse. In the present study, annealed copper shims of various sizes were used as the copper pulse shapers. The size of the shim was determined by trial and error depending on the impact velocity and the type of ice being tested. In the first trial, a test was run with an arbitrary pulse shaper size. The transmitted signal was then used to optimize the pulse shaper by matching the slopes of the incident signals (resulting from impacting the incident bar with different pulse shapers placed between the incident and striker bars) with the transmitted signal of the first test.

Figure 11 shows results of pulse shaper size optimization for impact velocities of 2.6 and 5 m/s. In figure 11(a), an initial trial on a 3- by 3- by 0.25-mm pulse shaper showed that the slope of the input signal is lower than that of the transmitted signal. Incremental increases in the pulse shaper dimensions (keeping the same thickness) were performed to increase the longitudinal impedance of the pulse shaper, to make it appear stiffer, and also to reduce the magnitude of plastic flow upon impact. Two sets of experiments were performed at the larger dimensions to assure such behavior. For the case of the higher impact velocity, a thinner pulse shaper of 0.13 mm was the first choice as it is expected to show less plastic flow and a steeper input signal should be obtained. This trial was unsuccessful and the previous thickness of 0.25 mm was then used but with larger lateral dimensions. Similarly, two trials were performed for the same dimensions for verification. It is clearly shown in figure 11 that for a given pulse shaper material the required dimensions of the pulse shaper depend on the impact speed.

Since ice is a brittle material (particularly in these ranges of temperatures and strain rates), the failure strains are less than 1 percent. Since the strain rate starts at zero in the beginning of the test and must increase during loading, there is little time to establish a constant value of strain rate before the samples break. Achieving a degree of constant strain rate loading was maximized through the use of pulse shapers. The average strain rate listed in the tables represents an average value taken near the maximum load (i.e., at fracture). The strain rate can vary by as much as 200/sec during this time. Nonetheless, given the small failure strains in ice, it is the best that could be achieved. Similar difficulties have been observed in other brittle materials such as ceramics (refs. 20 and 21) and rocks (ref. 22).

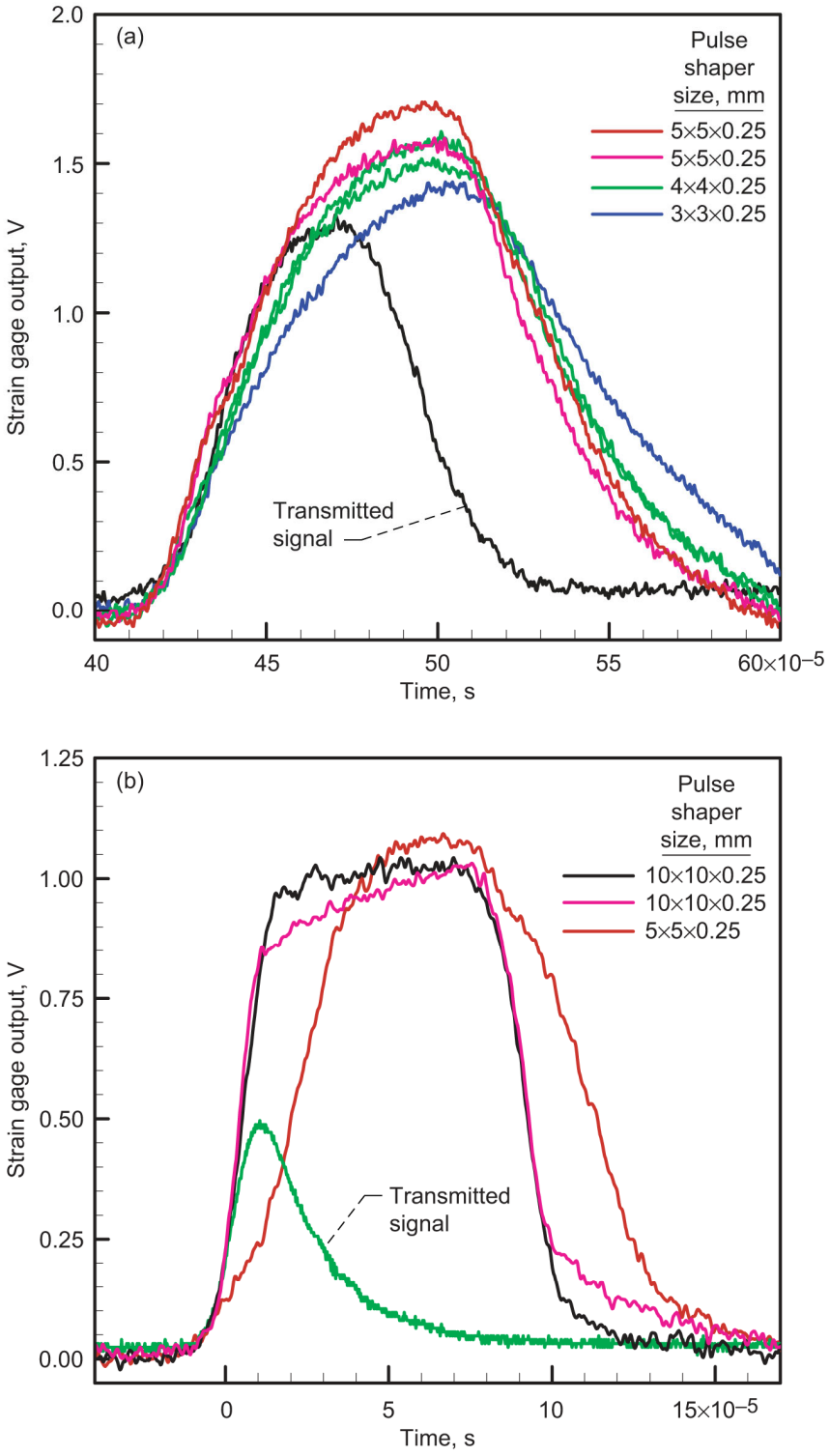

Figure 11.—Pulse shaper optimization at two impact velocities by trial and error method to match the slopes of incident and transmitted signals. (a) 2.6 m/s. (b) 5.0 m/s.

Experiments Performed at –10 °C

Single-crystal ice: 6SX series.—The first series of experiments was conducted on single-crystal ice specimens (6SX series). Tables I and II summarize the experimental parameters and results for this set of experiments, respectively. Strain gage signals, stress and strain-rate versus strain profiles, stress versus time diagrams, and the high-speed camera photographs for this series of experiments are provided in appendix B.

TABLE I.—EXPERIMENTAL PARAMETERS FOR 6SX EXPERIMENT SERIES[a]

Test number	Specimen		Shunt voltage		Chamber temperature, °C	Camera settings		Striker bar length, mm	Pulse shaper size, mm
	Diameter, mm	Length, mm	Gage 1, mV	Gage 2, mV		Delay, μs	Interframe time, μs		
6SX–3	18.62	5.49	14.7	64	–11.3	210	5	76.2	10×10×0.25
6SX–4	18.49	5.36	70	65	–11.0	210	10	152.4	No shaper
6SX–6	18.42	5.77	29	130	–11.4	---	---	152.4	10×10×0.25
6SX–7	18.52	5.26	29	130	–9.3	---	---	152.4	10×10×0.25
6SX–8	18.39	5.54	29	130	–12.1	---	---	152.4	10×10×0.25
6SX–9	18.37	5.38	70	65	–11.0	210	8	152.4	5×5×0.25
6SX–11	18.31	5.46	29	65	–12.0	210	8	152.4	9×9×0.25
6SX–12	18.38	5.05	14.5	68	–11.0	---	---	76.2	10×10×0.25

[a]The excitation voltages for gages 1 and 2 were 15 V for each test. Gages 1 and 2 are the strain gages attached to the incident and transmitted bars of the SHPB apparatus, respectively.

TABLE II.— EXPERIMENTAL RESULTS FOR 6SX EXPERIMENTS SERIES

Test number	Striker bar velocity, m/s	Average strain rate, s^{-1}	Maximum stress, MPa	Strain at maximum stress ($\times 10^{-3}$)	Time at maximum stress, μs
6SX–3	10.0	882	33.5	8.3	21.7
6SX–4	2.9	130	20.7	5.0	56.5
6SX–6	4.8	260	24.8	7.8	39.7
6SX–7	4.6	460	22.0	5.9	30.0
6SX–8	4.8	425	26.7	4.04	23.3
6SX–9	3.8	90	23.4	6.5	84.4
6SX–11	5.8	611	23.7	6.37	23.4
6SX–12	14.3	1122	34.7	7.7	15.7

Figure 12 summarizes the stress-strain behavior of single-crystal ice tested at –10 °C. A striker bar of length 150 mm was employed in all experiments except 6SX–8 and 6SX–12, where a striker bar of length 75 mm was used. By employing proper pulse shaping, a near constant strain rate was achieved in the specimens during the dynamic deformation process. For the shorter length striker bar the strain accumulated in the ice specimen was less than that obtained with a longer striker bar, and consequently, the specimen in experiment 6SX–8 did not yield or fail during the loading pulse, and significant elastic recovery is evident in figure 41 in appendix B. High-speed photography was employed in experiments 6SX–4, 6SX–9, and 6SX–11 to better understand the dynamic deformation and failure processes in ice. These studies revealed that the drop in peak stress was associated with the formation of a single dominant crack in the ice specimen. The first evidence of cracking was observed in frames 5, 12, and 4, respectively, with the loads being close to their peak levels. After attainment of the peak stress a large number of axial cracks were observed in the sample. The number of these microcracks was observed to increase as the deformation proceeded, eventually leading to complete fragmentation of the specimen. At

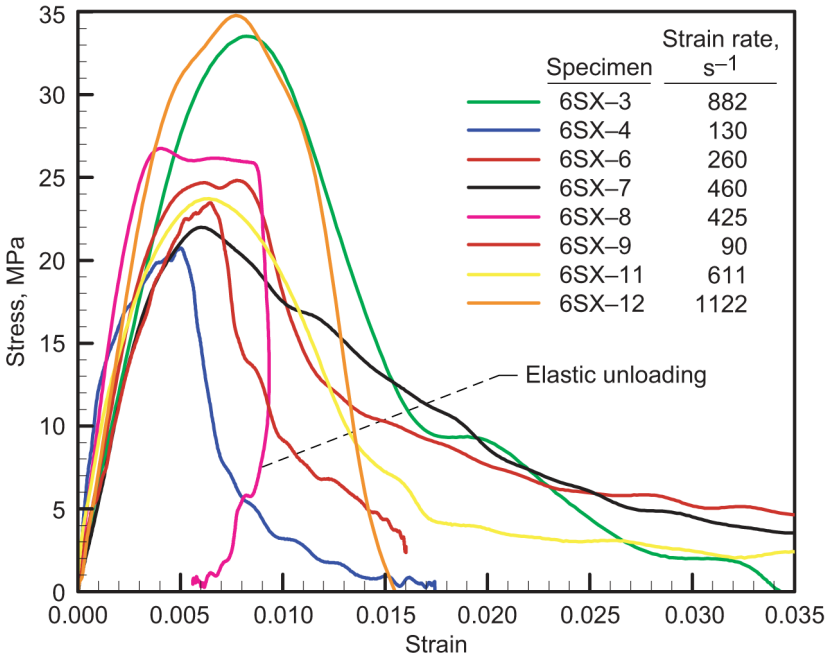

Figure 12.—Stress-strain curves at different strain rates for single-crystal ice 6SX experiment series.

relatively higher impact speeds (e.g., experiment 6SX–3), cracking in the specimen was observed to initiate during the rise time of the loading pulse well before the attainment of the peak stress levels. Moreover, the peak stress levels attained in these experiments were much higher than those obtained in the case of the lower impact velocity experiments, and no evidence of catastrophic load drop was observed in the transmitted strain gage signal after the attainment of peak stress levels. The peak stress was followed by a relatively large tail, with the post peak stress levels indicating the stress still carried by the pulverized and/or fragmented ice after failure.

CWRU-grown ice: HMD series.—In this series of experiments, the multigrained home grown ice samples were evaluated under test conditions similar to those employed during testing of the 6SX series of experiments, except that no vacuum grease was used between the specimen faces and bar inserts. In the 6SX series, for the highest strain rate experiments the maximum stress (failure stress) was attained at a time comparable to the equilibrium time. Therefore, in order to attain higher strain rates with failure times greater than the corresponding equilibrium times, thinner specimens than those used in the 6SX series of experiments were employed. Three different thicknesses of 5.5, 2.3, and 0.89 mm were tested. Table III summarizes the experimental parameters, while table IV summarizes the experimental results for this series of experiments. Strain gage signals, stress and strain-rate versus strain profiles, stress versus time diagrams, and the high-speed camera photographs for this series of experiments are provided in appendix C.

TABLE III.—EXPERIMENTAL PARAMETERS FOR HMD EXPERIMENT SERIES[a,b]

Test number	Specimen length,[c] mm	Shunt voltage		Chamber temperature, °C	Camera settings		Pulse shaper size, mm
		Gage 1, mV	Gage 2, mV		Delay, μs	Interframe time, μs	
HMD003	5.5	69	67	–9.8	---	---	9×9×0.25
HMD006	5.5	70	70	–10.0	---	---	No shaper
HMD008	5.5			–11.0	210	8	No shaper
HMD016	5.5			–12.2	210	5	5×5×0.25
HMD010	2.3			–10.2	210	8	No shaper
HMD011				–11.5	210	8	5×5×0.25
HMD014				–9.7	---	---	5×5×0.25
HMD018				–10.0	210	5	No shaper
HMD019				–9.0	---	---	5×5×0.25
HMD022	0.89			–11.0	---	---	5×5×0.25
HMD024	0.89			–10.1	---	---	5×5×0.25
HMD027	0.89			–10.1	---	---	5×5×0.25

[a]Excitation voltages for gages 1 and 2 were 15 V for each test. Gages 1 and 2 are the strain gages attached to the incident and transmitted bars of the SHPB apparatus, respectively.
[b]Striker bar length was 152.4 mm for each test.
[c]Specimen diameter was 19 mm for each test.

TABLE IV.—EXPERIMENTAL RESULTS FOR HMD EXPERIMENT SERIES

Test number	Striker bar velocity, m/s	Average strain rate, s^{-1}	Maximum stress, MPa	Strain at maximum stress ($\times10^{-3}$)	Time at maximum stress, μs
HMD003	6.0	770	22.7	10.9	27.7
HMD006	2.18	140	9.5	2.5	36.0
HMD008	2.0	92	11.7	4.1	59.5
HMD016	4.38	180	17.8	4.2	43.1
HMD010	2.3	312	14.6	11.1	53
HMD011	4.5	225	23.0	8.1	44
HMD014	7.4	740	23.5	6.2	21.6
HMD018	2.57	408	13.2	8.3	35.0
HMD019	4.57	397	15.1	6.5	28.7
HMD022	4.44	672	26.1	30.5	57.8
HMD024	4.53	740	22.0	16.6	33.0
HMD027	4.27	550	29.0	29.7	82

In this series of experiments the onset of cracking is observed to occur close to the peak stress level. This behavior is similar to that observed for the case of the 6SX series of experiments at comparable impact speeds. Cracking is evident in frame numbers 8, 8, 7, and 6 for experiments HMD016, HMD010, HMD011, and HMD018, respectively, while no cracking was observed for experiment HMD008, as shown in the high-speed camera photographs in appendix C. For the thinner 2.3-mm specimens, multiple cracks were seen to propagate simultaneously. This is in contrast with the single cracks that form in the thicker 5.5-mm samples.

The stress-strain diagrams for the different thickness specimens at multiple strain rates are shown in figures 13 to 15. In all cases except for experiments HMD008 and HMD027, the ice specimens were observed to fracture; in the case of experiments HMD008 and HMD027, evidence of elastic unloading is observed. For comparison the average failure strains for both single and polycrystalline ice under static loads was approximately $3\pm0.5\times10^{-3}$ (ref. 1). The strain at maximum stress is observed to increase as the specimen thickness decreases, as shown in table IV. The average strain at maximum stress for specimens with 5.5, 2.3, and 0.89 mm thickness are $5.42\pm3.73\times10^{-3}$, $8.04\pm1.94\times10^{-3}$, and $25.6\pm7.8\times10^{-3}$, respectively. It should be pointed out that the magnitude for the strains at failure for the 5.5-mm-thick specimens are comparable to those obtained for the single-crystal ice specimens (6SX series) with the

same specimen thickness. Again, the peak stress decreases as the strain rate decreases. The curves also exhibit a long tail after the attainment of maximum stress, which approaches some sizable stress as the sample thickness decreases and the strain rate increases, for example, 10 MPa for 0.89 mm thickness and 740 s^{-1} (fig. 15). Note that 10 MPa is the approximate compression strength of hard ice observed in quasi-static tests (ref. 1).

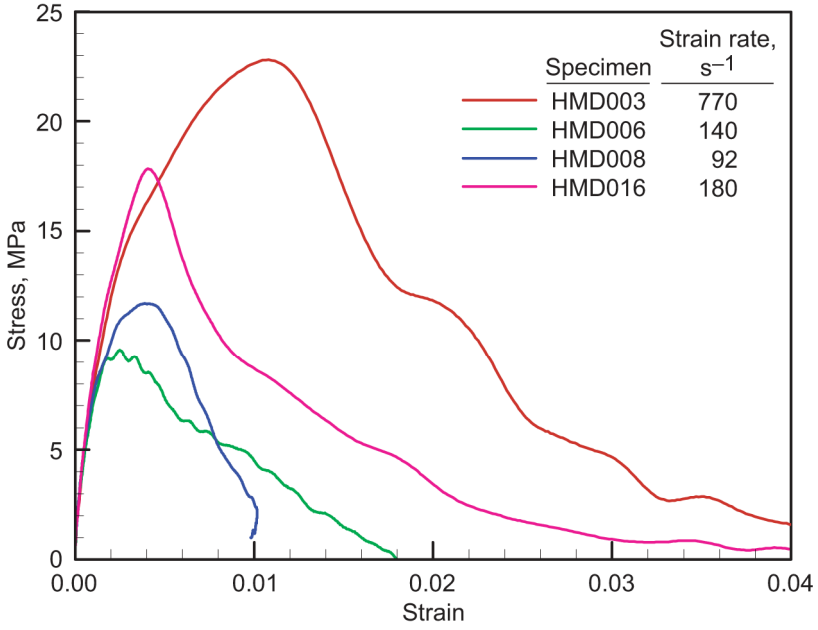

Figure 13.—Stress-strain curves at different strain rates for HMD experiment series for 5.5-mm-thick multigrained specimens.

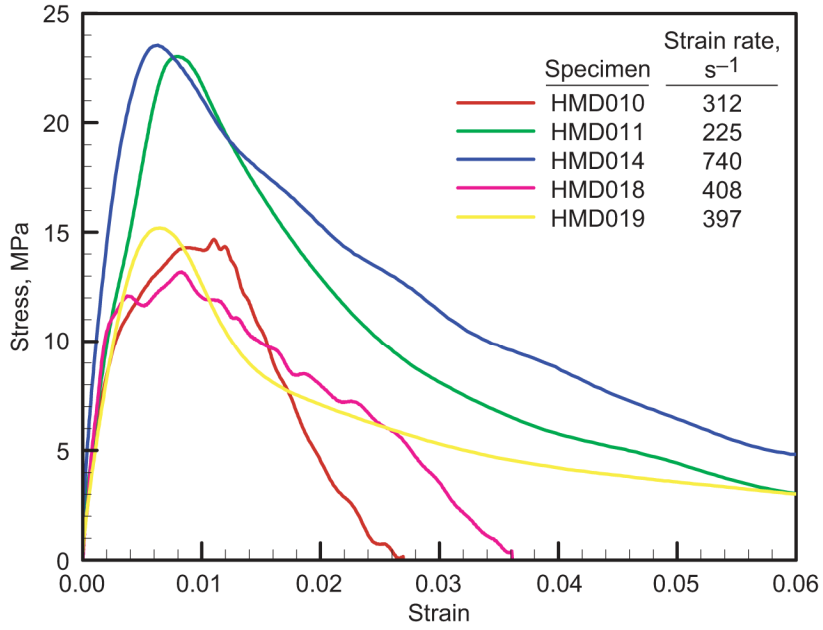

Figure 14.—Stress-strain curves at different strain rates for HMD experiment series for 2.3-mm-thick multigrained specimens.

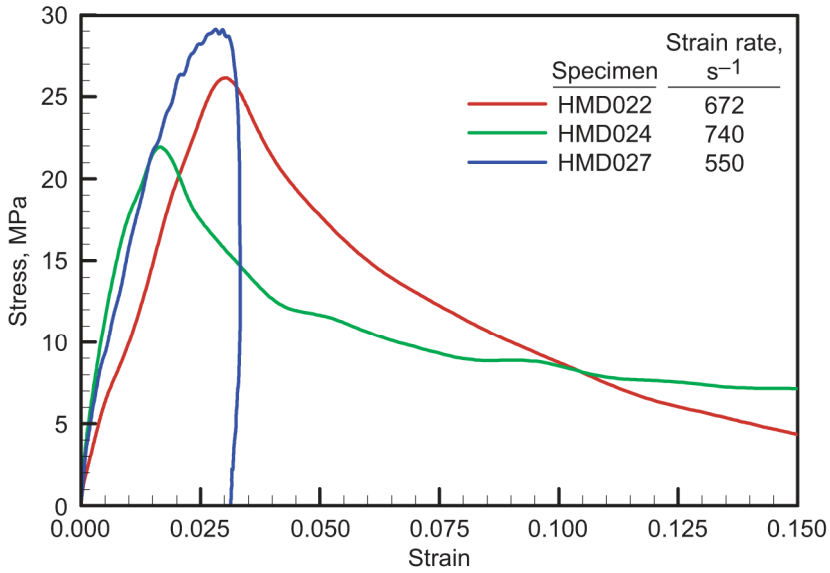

Figure 15.—Stress-strain curves at different strain rates for HMD experiment series for 0.89-mm-thick multigrained specimens.

Effect of constrained ends: 14SX series.—Next, a series of experiments was conducted to understand the effect of end constraint on the measured dynamic failure strength of ice. In these series of experiments single-crystal ice specimens (14SX series) supplied by Ice Research Lab at Dartmouth College were used. In order to create relatively strong end constraint conditions, a thin layer of water was sprayed on precooled aluminum inserts and the ice sample was set on this layer. The assembly was then kept in the freezer for at least 10 min to allow the specimen to freeze to the inserts. These specimens were then tested in the SHPB at strain rates similar to those employed in the previous experiments having less end constraint. The experimental parameters for this set of tests are summarized in table V, while the experimental results are summarized in table VI. Strain gage signals, stress and strain-rate versus strain profiles, and stress versus time diagrams for this series of experiments are provided in appendix D.

TABLE V.—EXPERIMENTAL PARAMETERS FOR 14SX EXPERIMENT SERIES WITH CONSTRAINED ENDS[a,b,c]

Test number	Specimen		C-axis orientation with respect to vertical, deg	Chamber temperature, °C	Pulse shaper size, mm
	Diameter, mm	Length, mm			
14SX–02	17.46	5.66	50	–11.5	5×5×0.25
14SX–03	17.46	5.74	45	–10.3	5×5×0.25
14SX–06	17.46	5.74	40	–10.3	5×5×0.25
14SX–07	19.0[d]	5.89	47	–10.0	5×5×0.25
14SX–09	19.0[d]	5.92	45	–10.5	9×9×0.25
14SX–18	19.0[d]	8.69	0	–11.0	5×5×0.25

[a]Excitation voltages for gages 1 and 2 were 15 V for each test. Gages 1 and 2 are the strain gages attached to the incident and transmitted bars of the SHPB apparatus, respectively.
[b]Shunt voltages for each test were 67 mV for gage 1 and 68 mV for gage 2.
[c]Striker bar length was 152.4 mm for each test.
[d]Grown from 17.0 mm.

TABLE VI.—EXPERIMENTAL RESULTS FOR 14SX EXPERIMENTS SERIES WITH CONSTRAINED ENDS

Test number	Striker bar velocity, m/s	Average strain rate, s^{-1}	Maximum stress, MPa	Strain at maximum stress ($\times 10^{-3}$)	Time at maximum stress, μs
14SX–02	5.3	318	14.7	2.6	24.0
14SX–03	3.9	200	21.8	8.1	55.8
14SX–06	3.5	139	17.3	4.8	52.5
14SX–07	3.3	187	10.8	3.9	36.2
14SX–09	5.2	278	24.0	4.4	31.2
14SX–18	3.3	80	19.0	3.9	56.6

Figure 16 shows the stress-strain diagrams for this series of experiments. The strain at maximum stress for the constrained end condition is observed to be somewhat less than that obtained for single-crystal ice specimens (6SX) tested with the unconstrained end condition (i.e., with vacuum grease between the specimen faces and the bars). Moreover, the times at which the maximum stress occurs are greater than those observed in the case of the 6SX series. However, the maximum stress is the same in both cases.

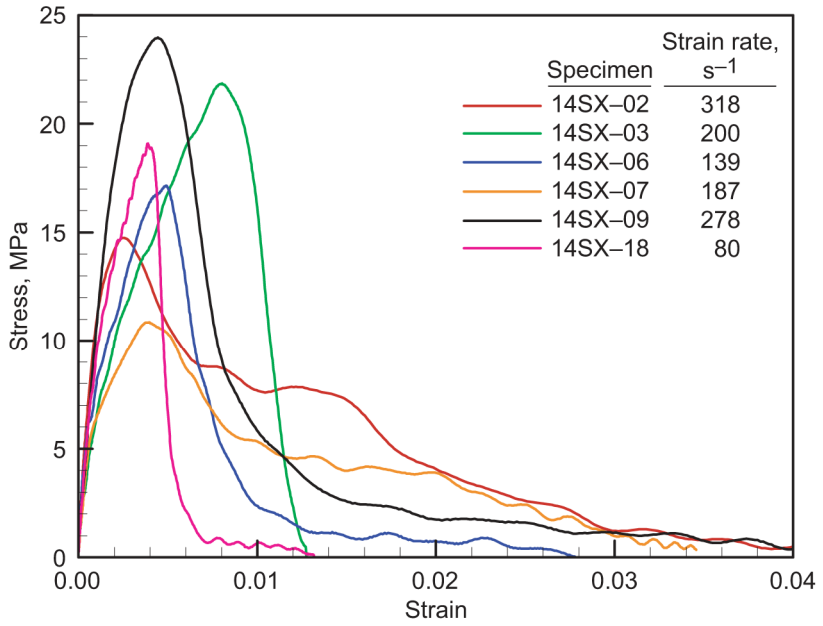

Figure 16.—Stress-strain curves at different strain rates for 14SX experiment series multigrained specimens with constrained ends.

Experiments Performed at –30 °C

Previous studies on ice have shown the failure strength to be temperature dependent (refs. 1 to 9). However, at elevated strain rates the strength has been reported to be temperature independent (ref. 12). In the present study, experiments were conducted at –30 °C on ice specimens grown at CWRU following procedures similar to those described earlier. Specimens with thicknesses of 5.8, 2.3, and 0.89 mm were grown and evaluated. The experimental parameters for this set of experiments are summarized in table VII, while the experimental results are summarized in table VIII. Strain gage signals, stress and strain-rate versus strain profiles, and stress versus time diagrams for this series of experiments are provided in appendix E. Figures 17 to 19 show the stress-strain diagrams for this series of experiments with specimen thicknesses of 5.8, 2.3, and 0.89 mm, respectively. While all other specimens that were evaluated failed during the tests, specimens utilized in Test 1 and Test 16 did not fail as evident by the elastic unloading curves (see figs. 98 and 116 in appendix E for strain gage signals in which the reflected signals showed positive and negative strain rate profiles). Once again the maximum stress is observed to have a positive correlation with strain rate. Also, specimens with 0.89 mm thickness show a distinct post failure plateau in the stress versus strain curves and maintain a stress level as high as 20 MPa in the post peak-stress strain regime, as shown in figure 19. The average strain at maximum stress for the specimens with a 5.8 mm thickness was $6.10\pm1.67\times10^{-3}$, for specimens with 2.3 mm thickness $10.33\pm1.87\times10^{-3}$, and for specimens with 0.89 mm thickness $38.17\pm9.15\times10^{-3}$. These strain values are slightly higher when compared with the same specimen thickness samples tested at –10 °C, which were $5.42\pm3.73\times10^{-3}$ for specimens with a 5.5 mm thickness, $8.04\pm1.94\times10^{-3}$ for specimens with a 2.3 mm thickness, and $25.6\pm7.8\times10^{-3}$ for specimens with a 0.89 mm thickness. Again the times corresponding to the maximum stress are larger than the equilibrium time and comparable to those for the specimens tested at –10 °C. The most important observation is that the maximum stresses for samples tested at –30 °C were higher than for specimens tested at –10 °C (compare figs. 17 to 19 with 13 to 15).

TABLE VII.—EXPERIMENTAL PARAMETERS FOR EXPERIMENTS PERFORMED AT –30 °C[a]

Test number	Specimen length,[b] mm	Excitation voltage		Shunt voltage		Chamber temperature, °C	Pulse shaper size, mm
		Gage 1, V	Gage 2, V	Gage 1, mV	Gage 2, mV		
1	5.8	15	15	67	68	–30.0	5×5×0.25
5	↓	15	15	29	29	–28.7	11×11×0.25
6	↓	7.5	7.5	14.4	36	–33.8	12×12×0.25
8	↓	↓	↓	↓	↓	–31.8	12×12×0.25
9	↓	↓	↓	↓	↓	–31.9	13×13×0.25
10	↓	↓	↓	↓	↓	–30.0	13×13×0.25
11	2.3	↓	↓	↓	↓	–29.7	11×11×0.25
12	2.3	↓	↓	↓	↓	–32.9	11×11×0.25
14	2.3	↓	↓	↓	↓	–31.7	13×13×0.25
16	0.89	↓	↓	↓	↓	–33.0	11×11×0.25
17	.89	↓	↓	↓	↓	–33.0	12×12×0.25
19	.89	↓	↓	↓	↓	–30.0	12×12×0.25
20	.89	↓	↓	↓	↓	–32.0	12×12×0.25

[a]The striker bar length was 152.4 mm for each test.
[b]Specimen diameter was 19 mm for each test.

TABLE VIII.—EXPERIMENTAL RESULTS FOR EXPERIMENTS PERFORMED AT –30 °C

Test number	Striker bar velocity, m/s	Average strain rate, s^{-1}	Maximum stress, MPa	Strain at maximum stress ($\times 10^{-3}$)	Time at maximum stress, μs
1	4.1	62	23	6.0	83.0
5	7.0	209	39.35	8.8	45.0
6	7.0	290	35.4	5.1	24.3
8	6.8	214	36.8	6.8	39.4
9	8.9	426	31.7	3.8	22.6
10	10.0	580	34	6.1	20.3
11	7.2	323	38.4	11.1	40.1
12	6.8	250	39.6	8.2	44.4
14	7.4	502	36	11.7	28.0
16	7.4	596	44.3	46.5	43.4
17	9.3	978	54	40.7	49.1
19	8.7	842	53.7	40.4	61.4
20	10.0	1441	58.4	25.1	25.4

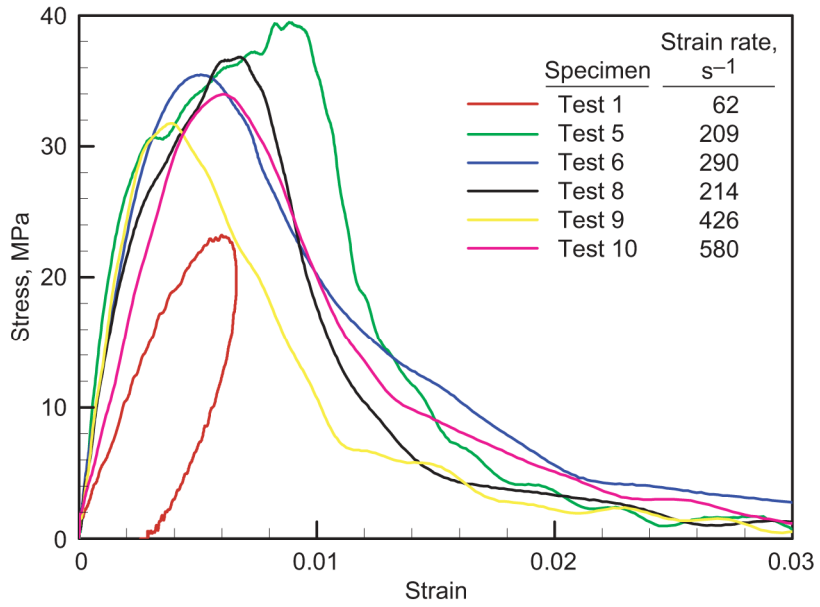

Figure 17.—Stress-strain curves at different strain rates for experiment series performed at –30 °C with 5.8-mm-thick multigrained specimens.

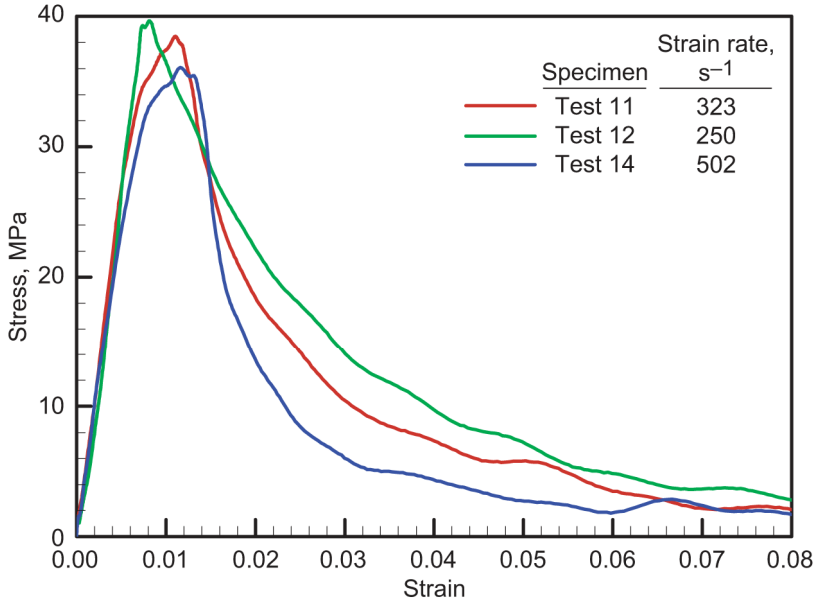

Figure 18.—Stress-strain curves at different strain rates for experiments series performed at –30 °C with 2.3-mm-thick multigrained specimens.

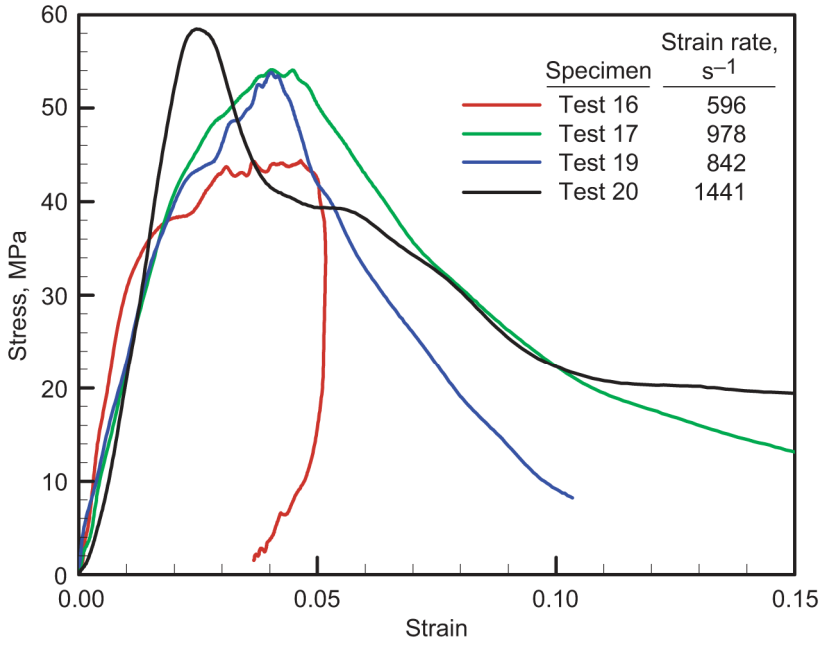

Figure 19.—Stress-strain curves for experiments series performed at –30 °C with 0.89-mm-thick multigrained specimens.

Discussions

The experimental results for maximum (failure) stress as a function of the average strain rate and the strain at maximum stress as a function of the specimen thickness are summarized in figures 20 and 21, respectively. From figure 20, it is clear that both single-crystal and the CWRU-grown polycrystalline ice have a positive strain rate dependency. This behavior is contradictory to other SHPB data (refs. 10 and

12) that is available in the literature in the strain rate regime of 10 to 100 s^{-1}; however, it correlates well with data obtained from lower strain rate testing on servo hydraulic machines at strain rates up to 10 s^{-1} (ref. 11). This behavior of positive strain rate dependency is similar to other brittle materials such as ceramics and rocks. For example, Macor glass ceramic (Corning Incorporated, Corning, NY) showed a positive strain rate dependency over a wide range of strain rates from 10^{-6} to 3000 s^{-1} (ref. 20), silicon carbide showed the positive strain rate dependency at strain rates higher than 250 s^{-1} (ref. 21), and granite showed the same behavior over a strain rate range of 100 to 600 s^{-1} (ref. 22). Moreover, as seen from figure 20, no clear evidence of specimen size effects on the failure strength can be deduced from the experimental results, but there is a specimen size effect on the strain at maximum stress as shown in figure 21.The peak stress reported in the work by Dutta et al. (ref. 12) was 6.53±1.44 MPa and 6.77±3.23 MPa at –10 °C under quasi-static and dynamic loading conditions, respectively. These values are two to three times less than those obtained in the present study. It must be noted that the specimens used in the study by Dutta et al. (ref. 12) had a thickness of 76 mm, which according to Davies and Hunter (ref. 19) requires about 75 μs to achieve stress equilibrium. However, the representative strain gage signals showed a failure time of approximately 80 μs, which is close to the time required for the specimens to reach equilibrium. Unfortunately, representative stress and strain-rate versus strain diagrams were not provided in their report, and so a judgment on uniform deformation conditions within the specimens can not be made with certainty. It should be noted that the values (6.53 MPa) obtained in their static tests agree well with the static strengths determined by Schulson et al. (ref. 1). Surprisingly, strains at peak stress under dynamic loading in their work were less than 2×10^{-3} as indicated in the representative stress strain diagrams of the SHPB experiments (though no values were tabulated as for the quasi-static experiments). These values, however, follow the trend of the dependency of strain at maximum stress on the specimen size in the present study as shown in figure 21.

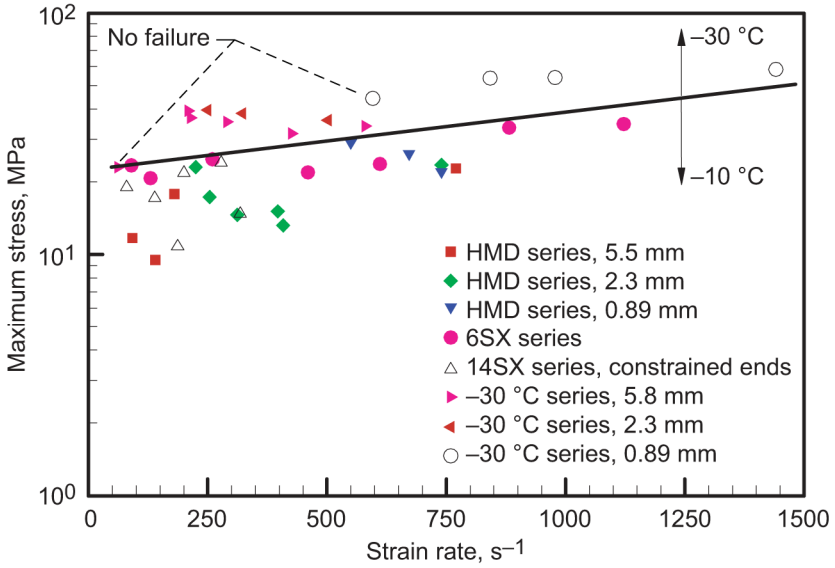

Figure 20.—Failure stress versus strain rate for SHPB ice specimens of different thicknesses.

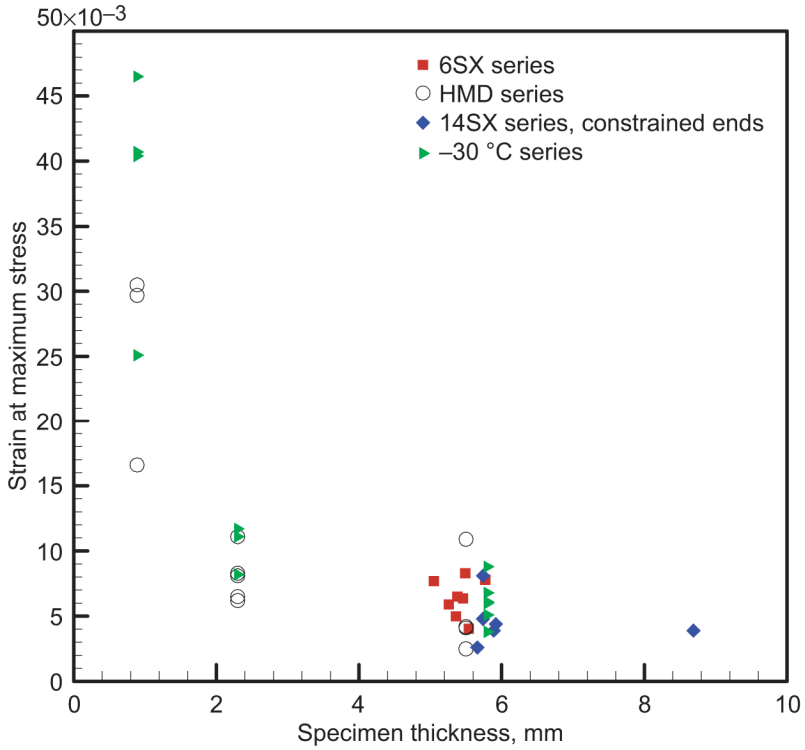

Figure 21.—Strain at maximum stress versus thickness for SHPB ice specimens of different test series.

The log-log plot in figure 22 gives a more conventional look at the strain rate effects on ice for experiments conducted at –10 °C. Included in the plot are the data from this report as well as the quasi-static data from Schulson et al. (ref. 1). The plot shows a clear, positive strain rate dependence over the range of strain rates of .01 to 1400 s^{-1} (over 5 orders of magnitude). There are two lines plotted in this figure to represent the relationship. The blue line represents the regression taken on the quasi-static data only (ref. 1) and extrapolated (dashed line) to the higher strain rates. This line over-predicts the strength at higher strain rates. A better fit is given by the orange solid line, which uses only the polycrystalline data over all strain rates (HMD series in present work). The equation is similar to that given by Schulson et al. (ref. 1) (blue line) and Jones (ref. 11) (pink line) and has the higher degree of correlation ($R^2 = 0.737$). The line is continuous with no jogs. Jones (ref. 11) had previously reported a jogged line as shown by the black line. Thus the strength of ice has a steady increase with increasing strain rate, and the relationship given by the orange line is preferred. This is a more satisfying relationship based on common sense expectations. This behavior also provides more confidence in extrapolating this relationship to still higher strain rates that are more typical of the ice impact events.

Schulson et al. (ref. 1) has shown a strong relationship of microstructure and strength. In their work single crystals were found to be the strongest followed by columnar-grained polycrystals followed by columnar grains loaded at an angle to the columns. While the difference in strength is not as large at the high strain rates, there is still evidence in stratification as can be observed in figure 20. The single-crystal samples are slightly stronger than the polycrystalline samples. A more systematic study is needed to better define this effect.

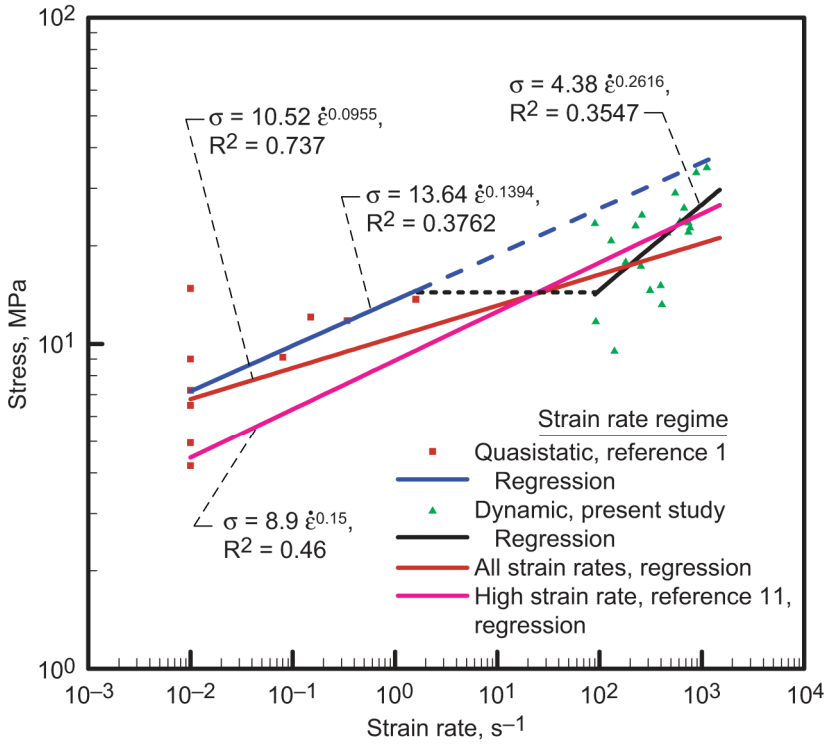

Figure 22.—Comparison of strain rate effects for multigrained ice specimens tested at –30 °C under different strain rate regimes.

One important consequence of this testing involves the postfracture behavior of the ice. It can be observed in the stress-strain curves that the sample still carries some load even after the sample breaks. This load is sizable and in most cases is larger than the quasi-static compression strength. This "tail strength" is dependent on sample thickness and strain rate, being higher for thinner samples and larger strain rates. This is because the shards of ice do not have the opportunity to fall out of the fixture, and thus end up maintaining some load. That is, the sample is no longer a coherent structure, but consists of fragmented ice. Similar behavior has been observed both during drop tower tests at NASA Langley Research Center and impact tests at NASA Glenn. During these tests the ice projectiles fragment upon impacting a load cell, but still impart a load due to the continued momentum of the ice particles. These results suggest that during modeling of impact events, more than just the initial impact load is required to define a state of damage. In fact, in the ballistic ice model used for RTF, the ice impact is treated first as a structure and then as a fluid to account for this continued momentum transfer (Dr. Kelly Carney, 2005, NASA Glenn Research Center, Cleveland, OH, personal communication).

Since the ice samples are thin to ensure stress equilibrium, concerns were raised about end effects playing a large role in the specimen stress distribution. End effects would result from high frictional effects at the sample ends constraining the radial displacement of the sample during loading. These effects should be more severe on a thinner sample than a thicker sample. In fact, this is precisely the reason why there are minimum sample thickness/diameter (T/*D*) ratios given for quasi-static compression testing for metals in ASTM Standard E9–89 (ref. 23). Here, the problem is approached for the ice by showing that frictional effects at high strain rates are minimal. Also, a finite element analysis was performed to show the uniformity of stress distribution within the samples.

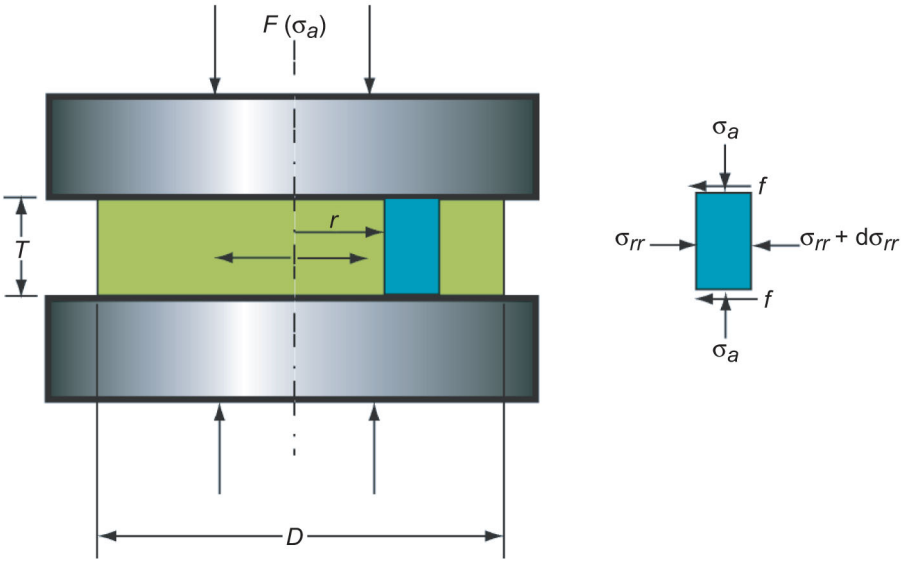

Figure 23.—Forces acting on material element in compression test, where T and D are specimen thickness and diameter, respectively; r is radial distance; $F(\sigma_a)$ is force of the axial stress; f is frictional stress; σ_{rr} is radial stress; and σ_a is axial stress.

The analysis of uniform uniaxial compression of solid cylinders under frictional forces (ref. 24) in figure 23 shows that the radial stress σ_{rr} is given by

$$\sigma_{rr} = f\frac{D}{T}\left(1-\frac{2r}{D}\right) \tag{16}$$

where f is the frictional stress and is assumed to be constant across the cross-sectional area of the specimen.

The radial stress σ_{rr} is minimized by decreasing the frictional stresses and/or the specimen diameter/thickness ratio D/T. Recent experimental work on ice frictional behavior with different materials (refs. 25 and 26) showed that the kinetic coefficient of friction is reduced by a factor of 10 as the sliding velocity changes from 10^{-5} m/s to 0.1 m/s. In the present study, assuming constant volume, the radial velocity of the outside radius of the specimen is given by

$$\frac{\mathrm{d}r(t)}{\mathrm{d}t} = \frac{r_o\dot{\varepsilon}(t)}{\left[1-\varepsilon(t)\right]^{3/2}} \tag{17}$$

where r_o is the original sample radius, and ε and $\dot{\varepsilon}$ are the instantaneous average strain and strain rate in the specimen, respectively. For the case of the experiment conducted at the lowest strain rate 62 s^{-1} and an initial diameter of 19.0 mm, the radial component of the particle velocity at the outside diameter of the specimen at the peak stress is approximately 0.6 m/s. This velocity would reduce the kinetic friction coefficient for ice from approximately 0.06 (ref. 25) by a factor of 10, thus negating the effects of friction. The axial stress distribution for two specimen thicknesses (1 and 5 mm) are shown in figures 24 and 25 for the cases without and with friction, respectively. The externally applied load is 25 MPa, which is magnified by the bar to specimen cross-sectional area ratio to be approximately 31 MPa on the specimen. In accordance with equation 16, the radial stress in the specimen increases as the height of the specimen is decreased, and decreases as we move away from the center of the specimen to its outer periphery. Furthermore, it is noted from figures 24 and 25 that the axial stress distribution is reasonably uniform within the thickness of the sample, more so in the case of the thicker sample; the axial stress gradient becomes steeper near the edge of the sample where the stress concentration is the highest. These

distributions of axial and radial stress within the specimen are conducive to the failure of the ice in shear, especially in the outer periphery of the specimen where the axial stress concentration is the highest. Moreover, these results suggest that the thinner specimens should fail at much lower load levels when compared to the thicker specimens employed in the present study. However, the experimental results of the present study indicate that the thinner and the thicker specimens fail at nearly similar load levels during the dynamic deformation process. This observed behavior can only be explained if the material strain-rate strengthening effects in the thin ice specimens dominate the aforementioned geometric weakening effects, and this reiterates the fact that the strength of ice is positively rate sensitive over the strain rate regime employed in the present experiments.

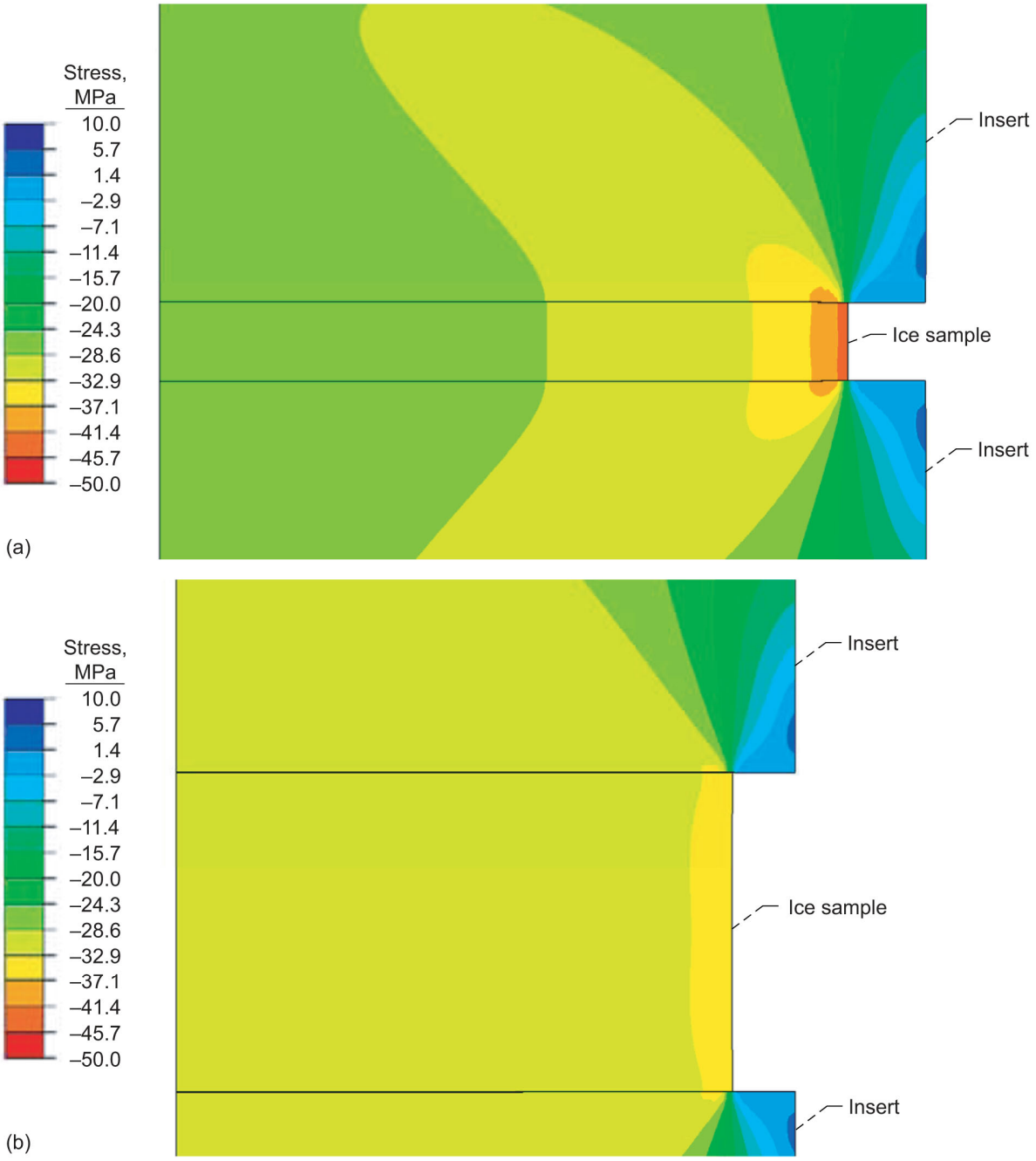

Figure 24.—Axial stress distribution in ice specimens under frictionless conditions. (a) 1-mm-thick specimens. (b) 5-mm-thick specimens.

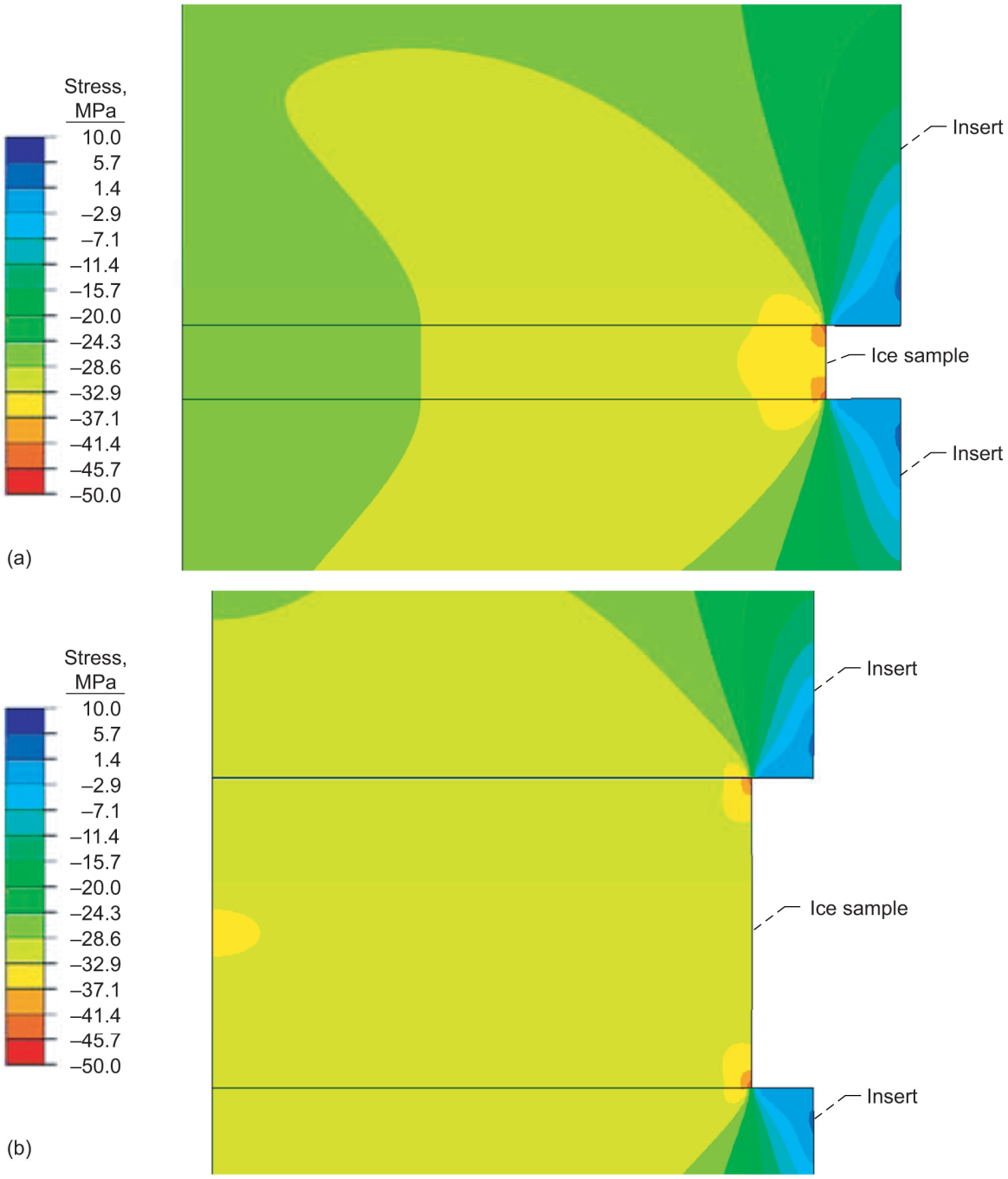

Figure 25.—Axial stress distribution in ice specimens under coefficient of friction of 0.1. (a) 1-mm-thick specimens. (b) 5-mm-thick specimens.

As suggested in figure 20, the presence of the end constraint at the specimen-bar interface has a negligible effect on the measured dynamic failure strength of ice. This is, however, contradictory to observations in quasi-static compression experiments (refs. 1 and 27), where constrained ends were understood to affect both the mechanical strength and the failure modes. A possible explanation for this behavior could be attributed to the rupture of the interface between the ice disk and the bars (shown schematically in fig. 26) in the early stages of loading. However, more work is still needed to explore this effect completely.

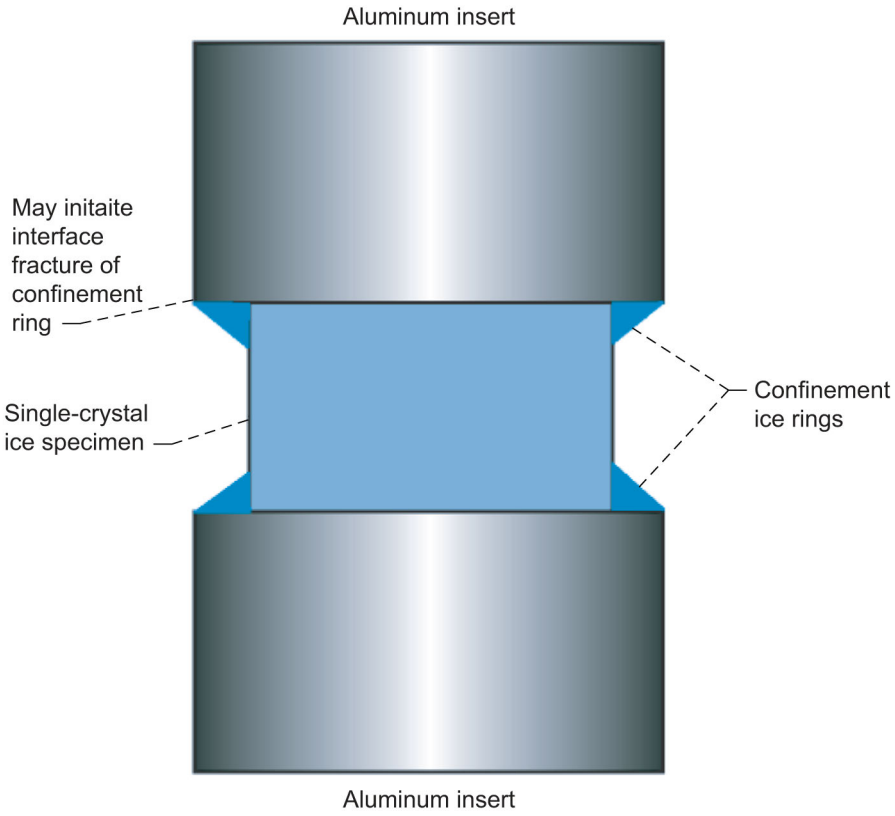

Figure 26.—Formation of edge constraint on specimens tested to determine the effect of end constraint on failure strength.

Summary of Results

In the present study a modified split Hopkinson pressure bar apparatus was developed to investigate the high-strain-rate behavior of ice. Ice was shown to have a positive strain rate sensitivity in the strain rate range of 90 to 1400 s^{-1}. Specimen size, within the range studied, was found to have little or no effect on the failure strength. The test temperature was observed to have a strong effect on the failure strength with ice behaving stronger as the test temperature was decreased. The effect of specimen end constraint on failure strength during high-rate deformation of ice was found to be negligible. Results of previous experimental studies to investigate the effects of end constraint at quasi-static loading rates are contrary to those obtained at higher loading rates in the current study. Also, the results of the present study are in contradiction with previous high-strain-rate investigations, where ice was reported to show a negative strain rate sensitivity at strain rates of 10 s^{-1} and higher.

References

1. Schulson, Erland M.; Iliescu, Daniel; and Fortt, Andrew: Characterization of Ice for Return-to-Flight of the Space Shuttle. Part 1—Hard Ice. NASA CR—2005-213643—PART1, 2005.
2. Haynes, F.D.: Effect of Temperature on the Strength of Snow-Ice. CRREL–78–27, 1978.
3. Currier, J.H.; and Schulson, E.M.: The Tensile-Strength of Ice as a Function of Grain-Size. Acta Metall., vol. 30, no. 8, 1982, pp. 1511–1514.

4. Schulson, E.M.: The Structure and Mechanical Behavior of Ice. JOM, vol. 51, no. 2, 1999, pp. 21–27.
5. Dempsey, J.P.; et al.: Scale Effects on the In-Situ Tensile Strength and Fracture of Ice. Part I: Large Grained Freshwater Ice at Spray Lakes Reservoir, Alberta. Int. J. Fract., vol. 95, nos. 1–4, 1999, pp. 325–345.
6. Dempsey, J.P.; Adamson, R.M.; and Mulmule, S.V.: Scale Effects on the In-Situ Tensile Strength and Fracture of Ice. Part II: First-Year Sea Ice at Resolute, NWT. Int. J. Fract., vol. 95, nos. 1–4, 1999, pp. 347–366.
7. Nixon, W.A.; and Schulson, E.M.: A Micromechanical View of the Fracture-Toughness of Ice. J. de Physique, vol. 48, (C–1), 1987, pp. 313–319.
8. Weber, L.J.; and Nixon, W.A.: Fracture Toughness of Freshwater Ice. 1. Experimental Technique and Results. Trans. ASME J. Offshore Mechanics Arctic Engineering, vol. 118, no. 2, 1996, pp. 135–140.
9. Uchida, T.; and Kusumoto, S.: Effects of Test Conditions on Fracture Toughness and Fracture Morphology of Polycrystalline Ice. JSME International Journal Series A—Solid Mechanics and Material Engineering, vol. 42, no. 4, 1999, pp. 601–609.
10. Dutta, Piyush K.: Compressive Failure of Polycrystalline Ice Under Impact. Proceedings of the Third International Offshore and Polar Engineering Conference, 1993, pp. 573–580.
11. Jones, Stephen J.: High Strain-Rate Compression Tests on Ice. J. Phys. Chem. B, vol. 101, no. 32, 1997, pp. 6099–6101.
12. Dutta, Piyush K., et al.: A Fracture Study of Ice Under High Strain Rate Loading. Proceedings of the Thirteenth International Offshore and Polar Engineering Conference, 2003, pp. 465–472.
13. Schulson, E.M.: Brittle Compressive Fracture of Ice. Acta Metall. Mater., vol. 38, no. 10, 1990, pp. 1963–1976.
14. St. John, J.W.; and Daley, C.: Shipboard Measurement of Ice Pressures in the Bering, Chukchi, and Beaufort Seas. Proceedings of the International Offshore Mechanics and Arctic Engineering Symposium, vol. 3, 1984, pp. 260–266.
15. Graff, Karl F.: Wave Motion in Elastic Solids. Dover Publications, New York, NY, 1991.
16. Haberman, Richard: Applied Partial Differential Equations: With Fourier Series and Boundary Value Problems. Fourth ed., Pearson/Prentice Hall, Upper Saddle River, NJ, 2004.
17. Carter, Donald: Lois et Mécanismes de l'apparente Fracture Fragile de la Glace de Rivière et du Lac. Thèse (de dectorat), Université Laval, 1971.
18. Petrovic, J.J.: Mechanical Properties of Ice and Snow. J. Mater. Sci., vol. 38, no. 1, 2003.
19. Davies, E.D.H.; and Hunter, S.C.: The Dynamic Compression Testing of Solids by the Method of the Split Hopkinson Pressure Bar. J. Mech. Phys. Solids, vol. 11, no. 3, 1963, pp. 155–179.
20. Weinong, Chen; and Ravichandran, G.: Dynamic Failure Behavior of Ceramics Under Multiaxial Compression. Ph.D. Thesis, California Institute of Technology, 1995.
21. Sarva, S.; Nemat-Nasser, S.: Dynamic Compressive Strength of Silicon Carbide Under Uniaxial Compression. Mater. Sci. Eng. A, vol. 317, nos. 1–2, 2001, pp. 140–144.
22. Shan, Renliang; Jiang, Yusheng; and Li, Baoqiang: Obtaining Dynamic Complete Stress-Strain Curves for Rock Using the Split Hopkinson Pressure Bar Technique. Int. J. Rock. Mech. Min. Sci., vol. 37, no. 6, 2000, pp. 983–992.
23. Standard Test Methods of Compression Testing of Metallic Materials at Room Temperature. ASTM Designation E9–89a (Reapproved 2000), American Society for Testing and Materials Annual Book of Standards, vol. 03.01, ASTM International, West Conshohocken, PA, 2004, pp. 110–118.
24. Kuhn, H.A.: Uniaxial Compression Testing. ASM Handbook, vol. 8, ASM, Materials Park, OH, 2000.
25. Maeno, N., et al.: Ice-Ice Friction Measurements, and Water Lubrication and Adhesion-Shear Mechanisms. Canad. J. Phys., vol. 81, nos. 1–2, 2003, pp. 241–249.
26. Maeno, Norikazu; and Arakawa, Masahiko: Adhesion Shear Theory of Ice Friction at Low Sliding Velocities, Combined With Ice Sintering. J. Appl. Phys., vol. 95, no. 1, 2004, pp. 134–139.

27. Schulson, E.M.; Iliescu, D.; and Renshaw, C.E.: On the Initiation of Shear Faults During Brittle Compressive Failure: A New Mechanism. J. Geoph. Res., vol. 104 (B1), 1999, pp. 695–705.
28. Hobbs, Peter V.: Ice Physics. Clarendon Press, Oxford, 1974.

Appendix A
Symbols

A	cross-sectional area of incident and transmitted bars of SHPB apparatus
C	longitudinal wave speed in ice
c_b	longitudinal wave speed in bar
D	specimen diameter
E	Young's modulus
f	function representing pressure wave traveling to right
f	frictional stress
g	function representing pressure wave traveling to left
h	function representing wave traveling to right
P	force on sample face
T	specimen thickness
t	time
u	displacement
$\dot{u}$	displacement rate
x	axial position along sample
ε	strain
$\dot{\varepsilon}$	strain rate
ρ	specimen density
σ	stress

Subscripts

a	axial
b	bar
equil	equilibrium
i	incident
o	original
r	reflected
rr	radial
s	average
t	transmitted
1	left end of sample
2	right end of sample

Appendix B
Experimental Results for 6SX Series

Results for the single-crystal ice samples tested with a modified split Hopkinson pressure bar apparatus at –10 °C are presented here in figures 27 through 51.

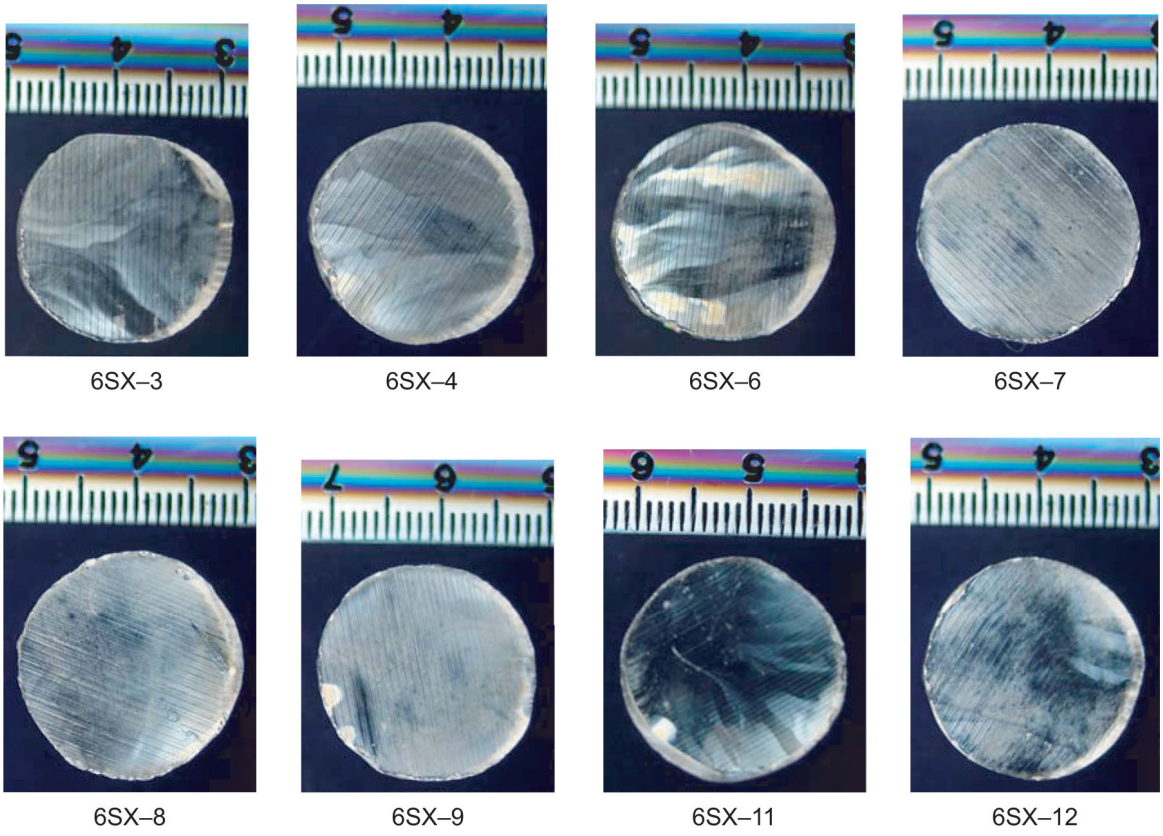

Figure 27.—Crystal structure of 6SX series single-crystal ice specimens supplied by Dartmouth College (Hanover, NH).

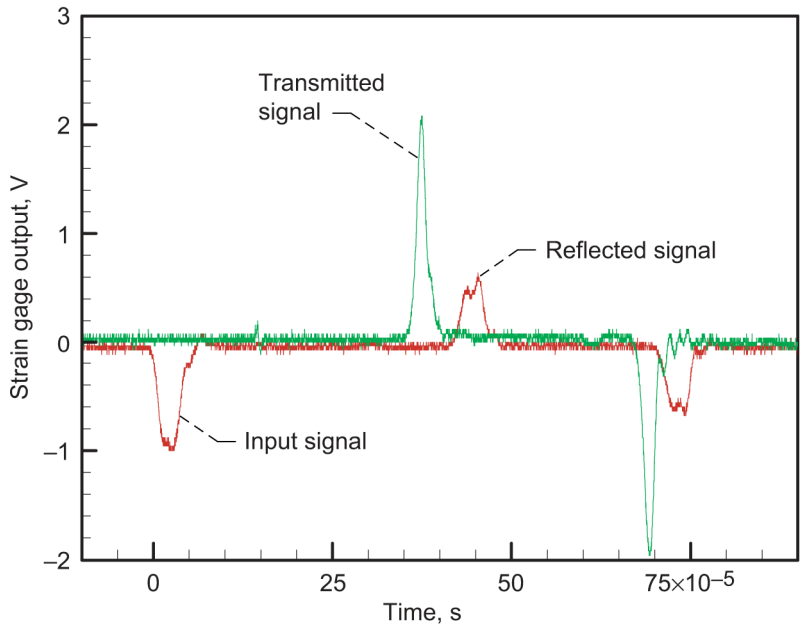

Figure 28.—Strain gage signals for experiment 6SX–3 on single-crystal ice at –10 °C.

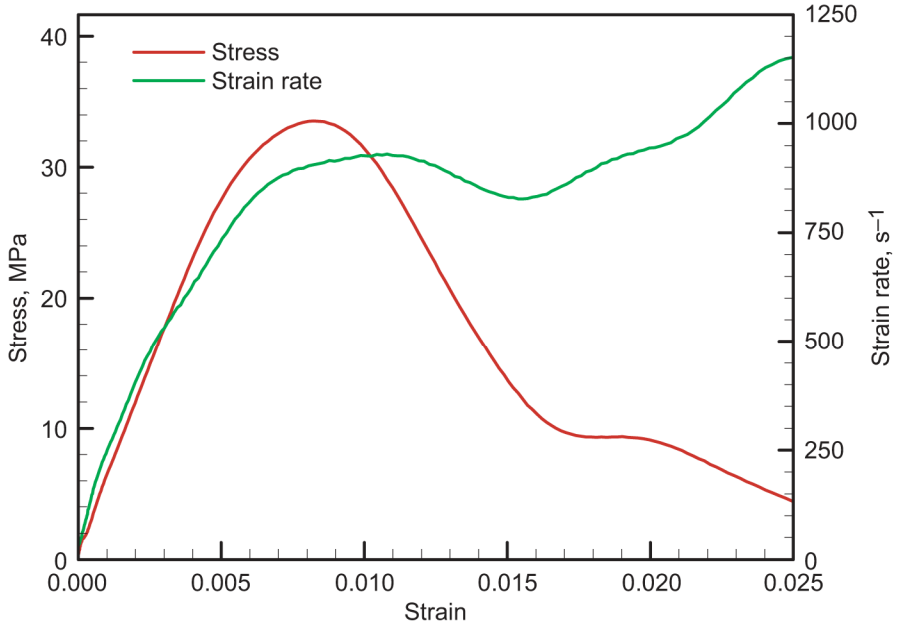

Figure 29.—Stress and strain rate versus strain curves for experiment 6SX–3 on single-crystal ice at –10 °C.

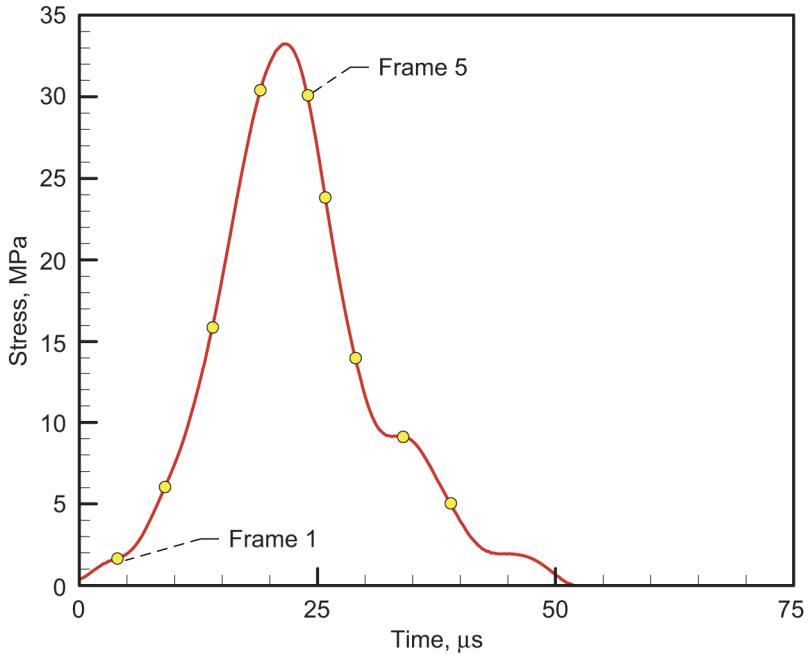

Figure 30.—Stress-time diagram for experiment 6SX–3 on single-crystal ice at –10 °C. Frame numbers correspond to those in figure 31.

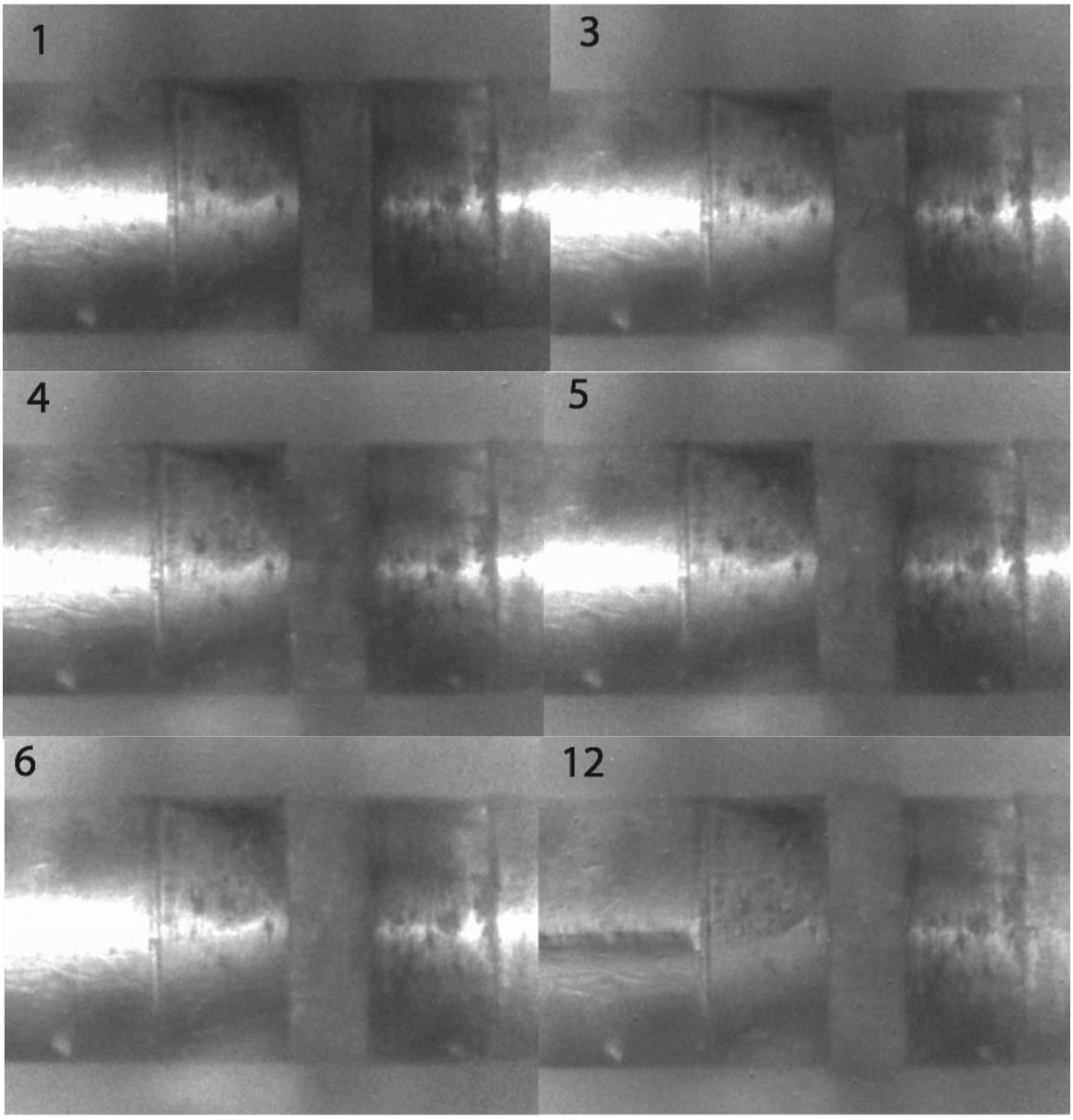

Figure 31.—High-speed camera images for experiment 6SX–3 on single-crystal ice at –10 °C with frame numbers identified.

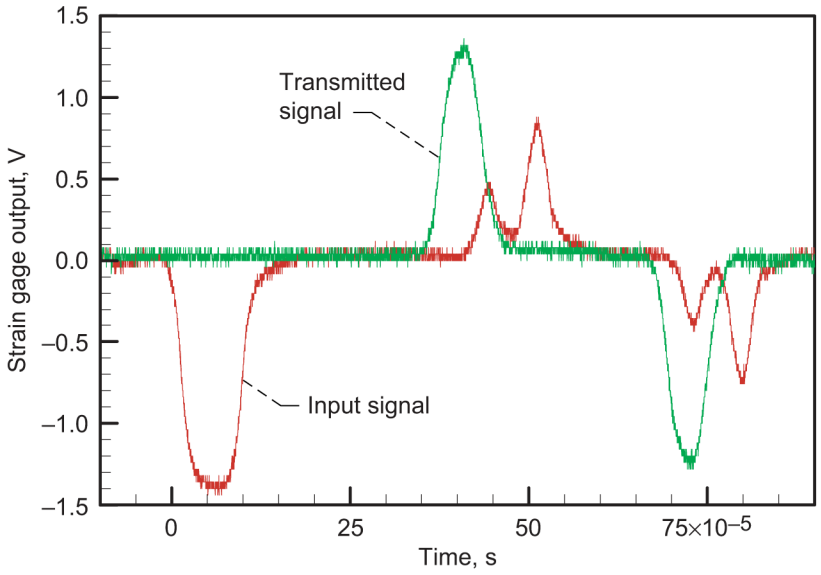

Figure 32.—Strain gage signals for experiment 6SX–4 on single-crystal ice at –10 °C.

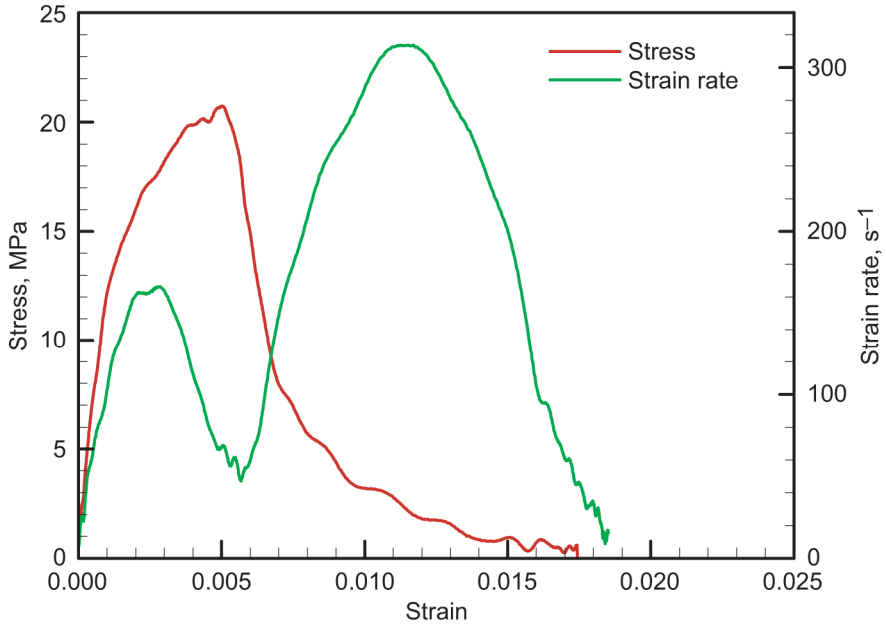

Figure 33.—Stress and strain rate versus strain curves for experiment 6SX–4 on single-crystal ice at –10 °C.

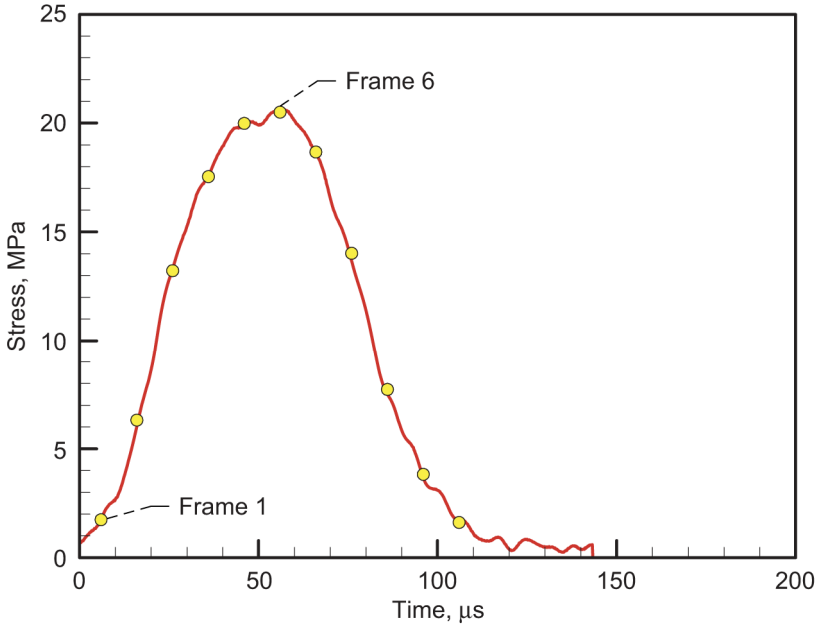

Figure 34.—Stress-time diagram for experiment 6SX–4 on single-crystal ice at –10 °C. Frame numbers correspond to those in figure 35.

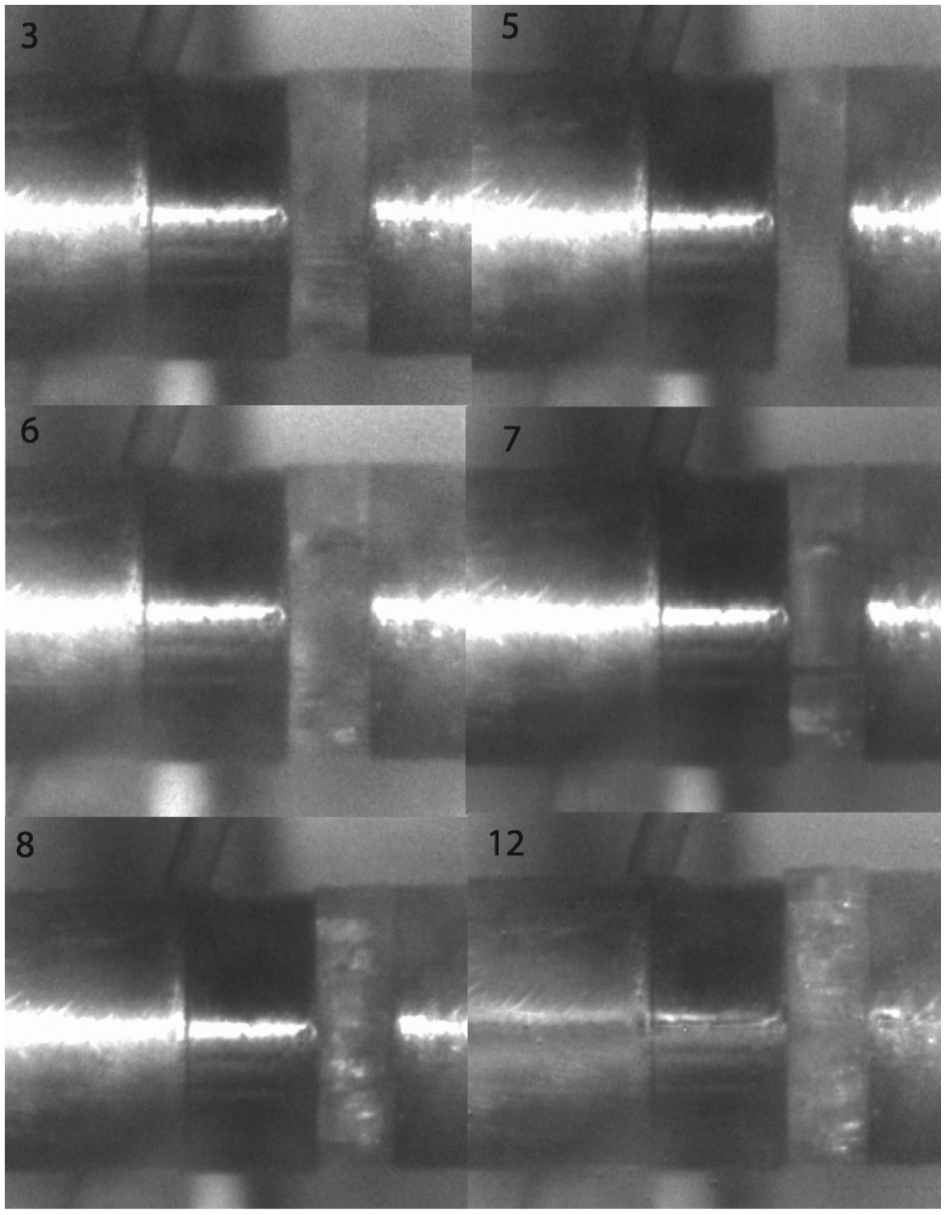

Figure 35.—High-speed camera images for experiment 6SX–4 on single-crystal ice at –10 °C with frame numbers indicated.

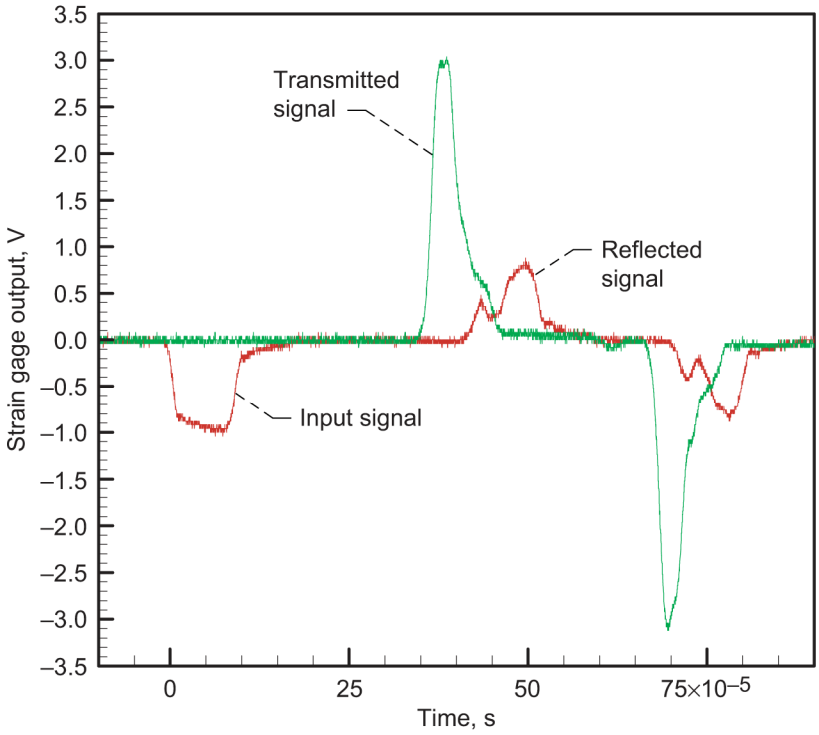

Figure 36.—Strain gage signals for experiment 6SX–6 on single-crystal ice at –10 °C.

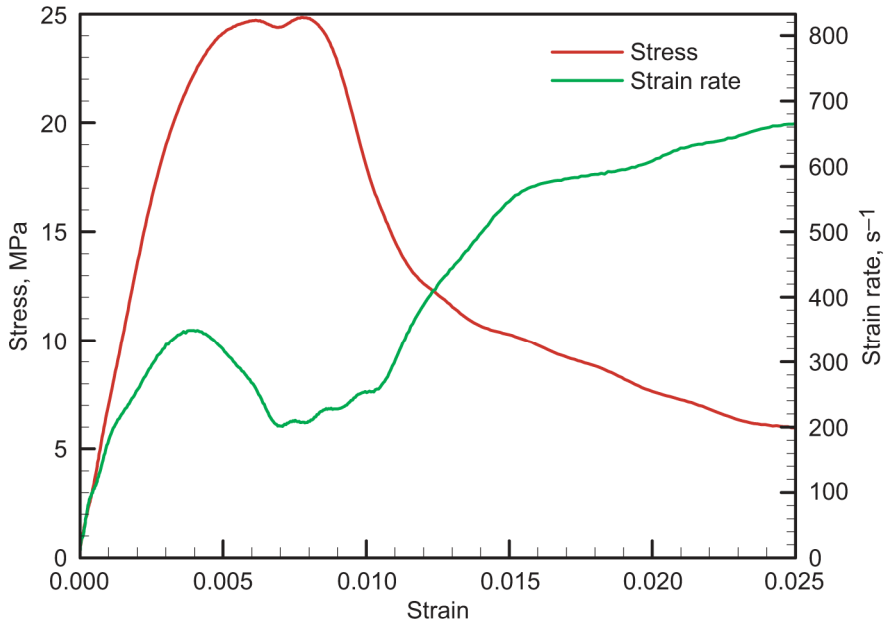

Figure 37.—Stress and strain rate versus strain curves for experiment 6SX–6 on single-crystal ice at –10 °C.

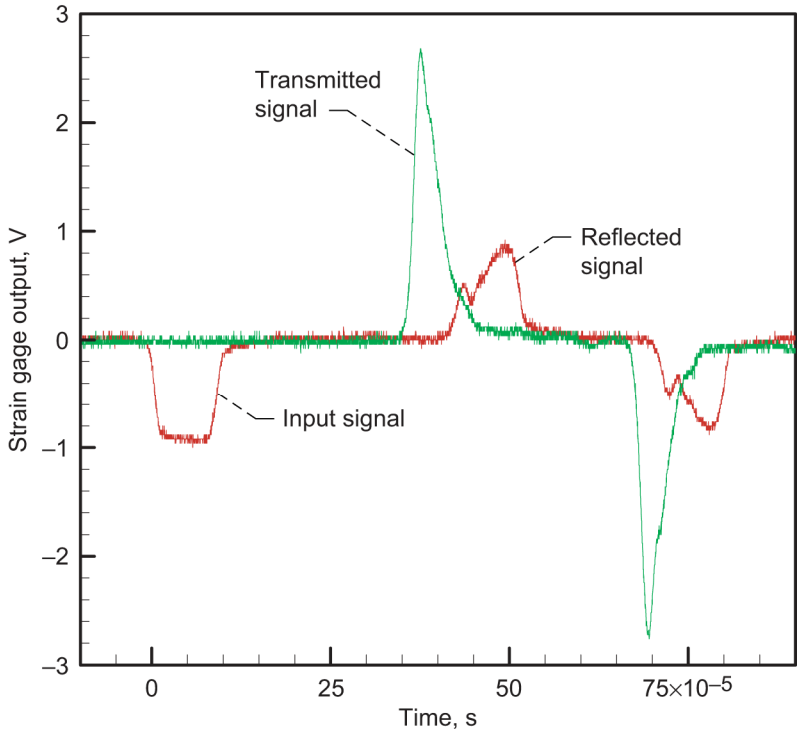

Figure 38.—Strain gage signals for experiment 6SX–7 on single-crystal ice at –10 °C.

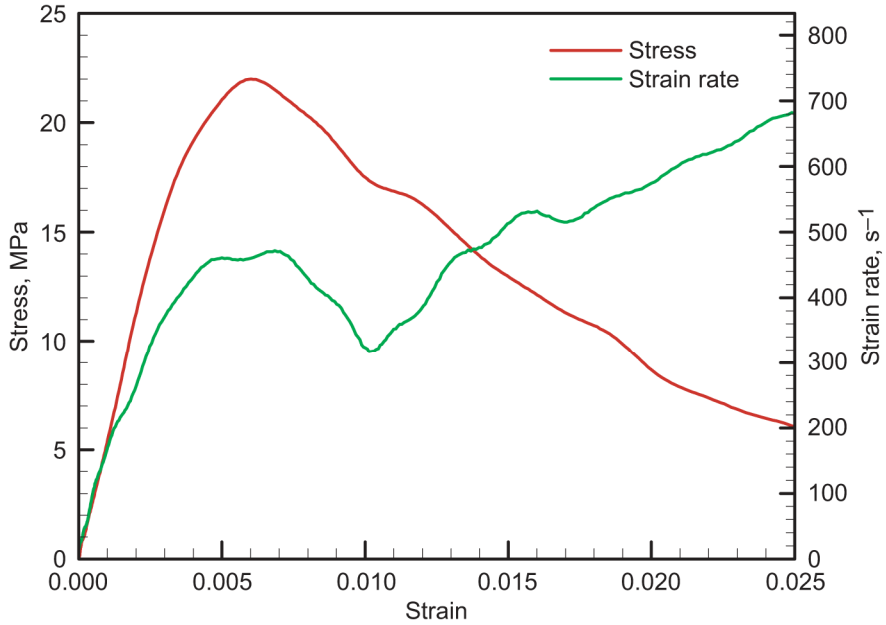

Figure 39.—Stress and strain rate versus strain curves for experiment 6SX–7 on single-crystal ice at –10 °C.

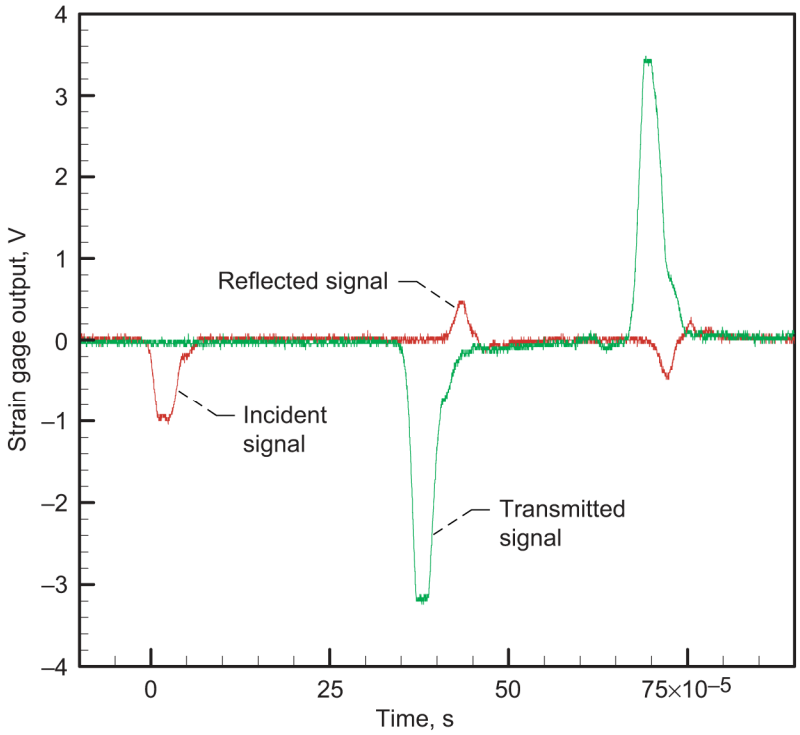

Figure 40.—Strain gage signals for experiment 6SX–8 on single-crystal ice at –10 °C.

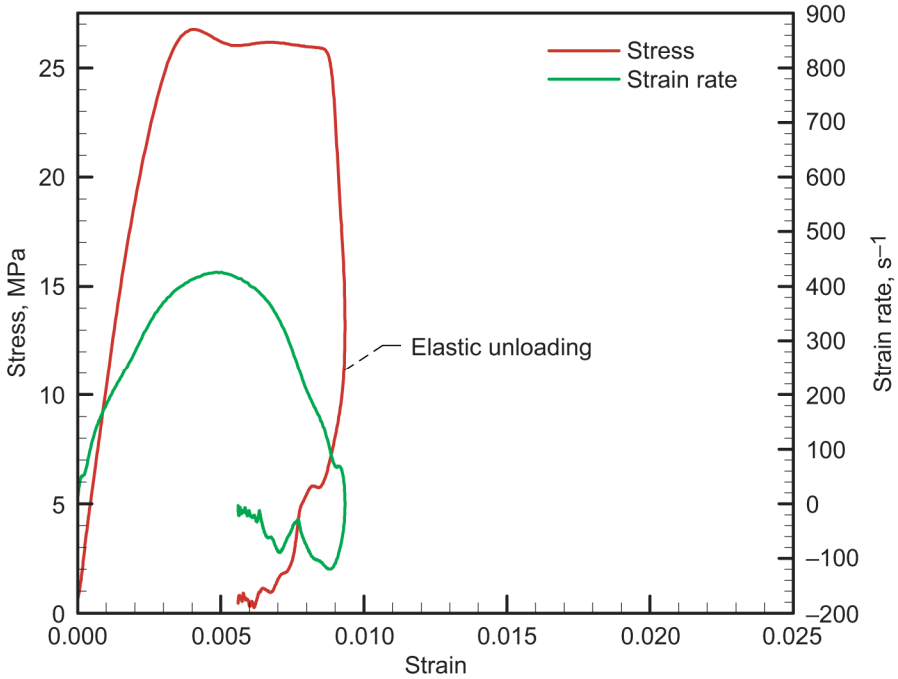

Figure 41.—Stress and strain rate versus strain curves for experiment 6SX–8 on single-crystal ice at –10 °C.

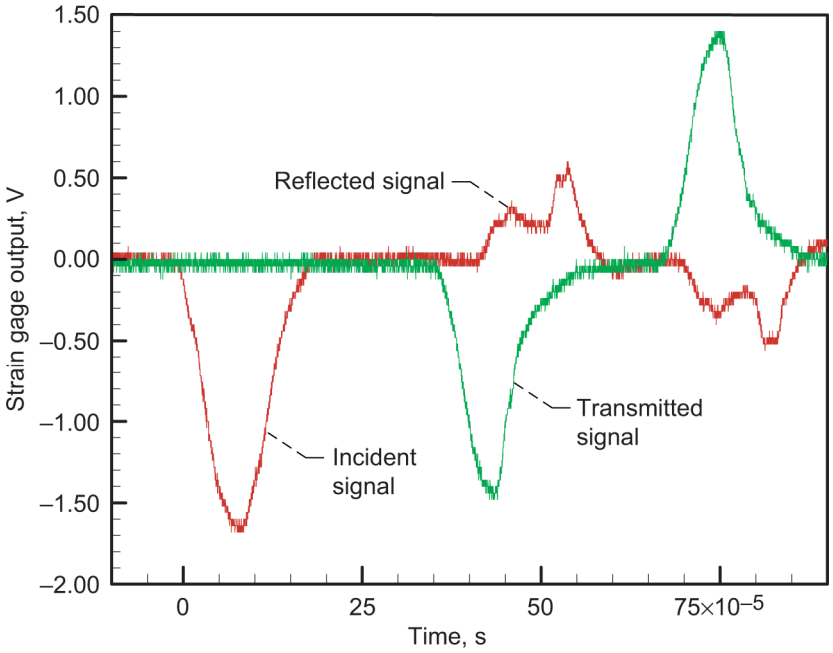

Figure 42.—Strain gage signals for experiment 6SX–9 on single-crystal ice at –10 °C.

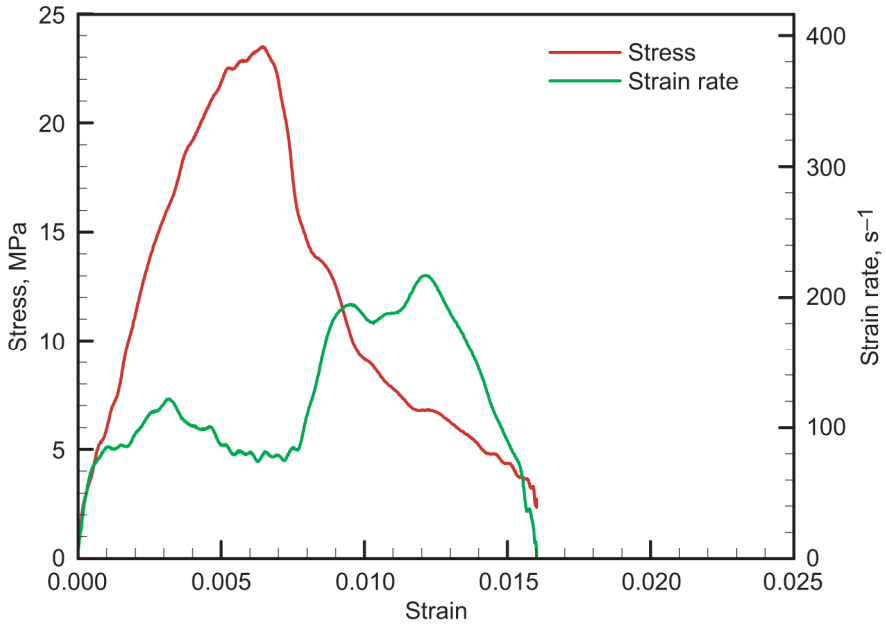

Figure 43.—Stress and strain rate versus strain curves for experiment 6SX–9 on single-crystal ice at –10 °C.

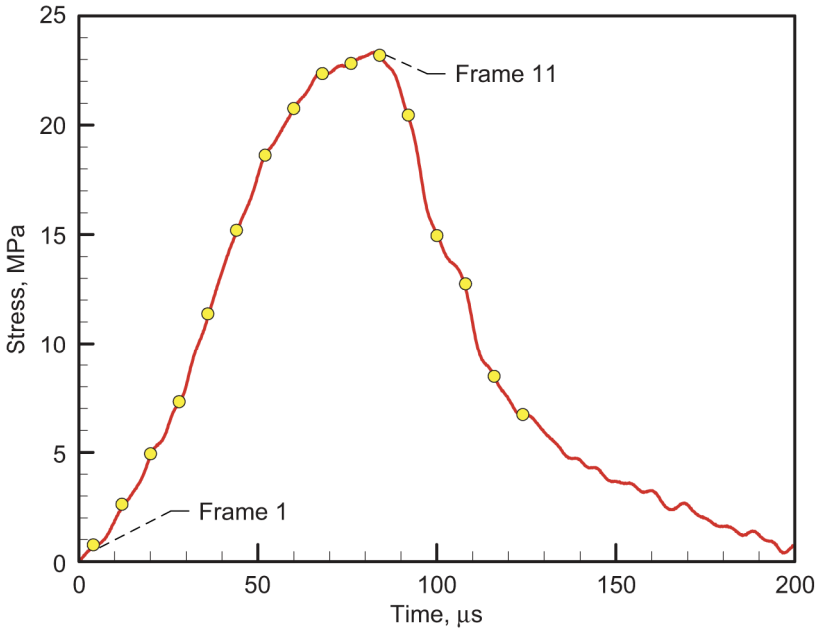

Figure 44.—Stress-time diagram for experiment 6SX–9 on single-crystal ice at –10 °C. Frame numbers correspond to those in figure 45.

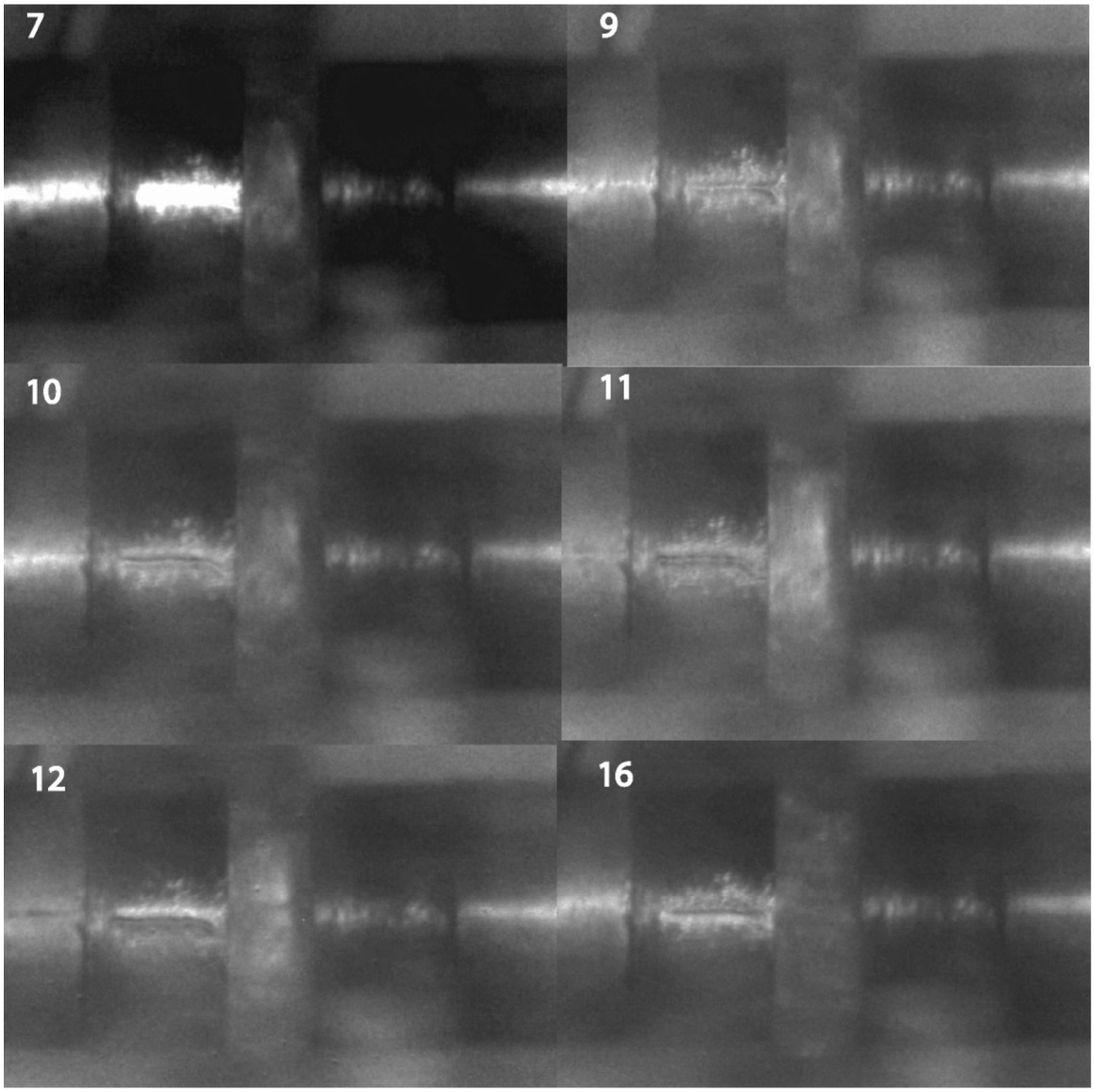

Figure 45.—High-speed camera images for experiment 6SX–9 on single-crystal ice at –10 °C with frame numbers indicated.

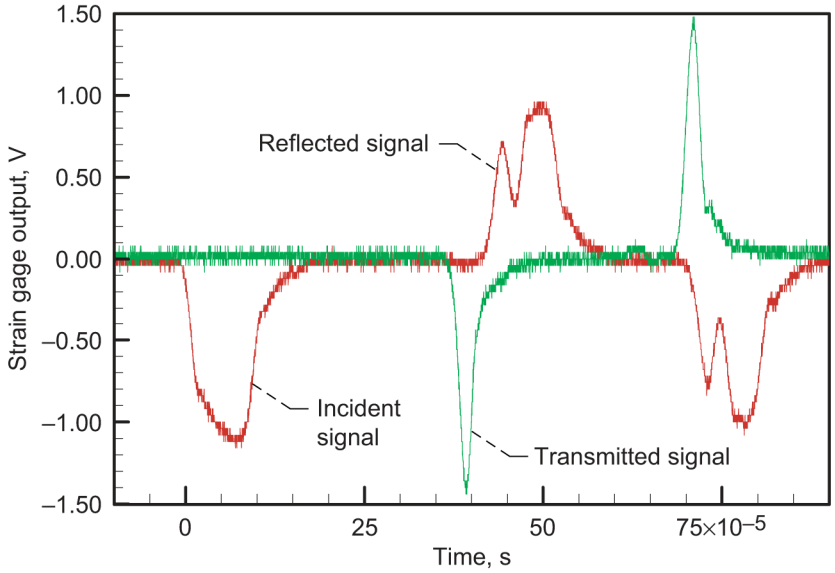

Figure 46.—Strain gage signals for experiment 6SX–11 on single-crystal ice at –10 °C.

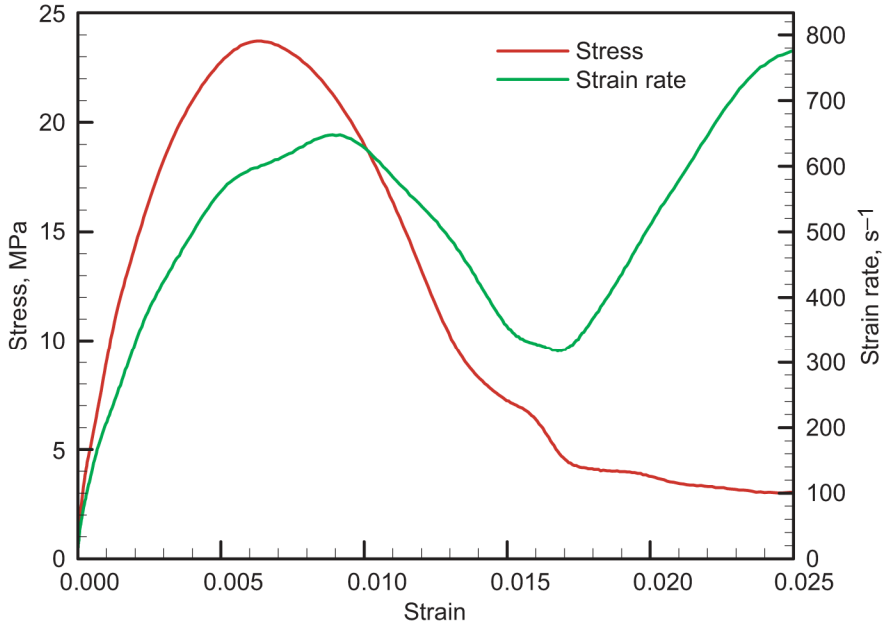

Figure 47.—Stress and strain rate versus strain curves for experiment 6SX–11 on single-crystal ice at –10 °C.

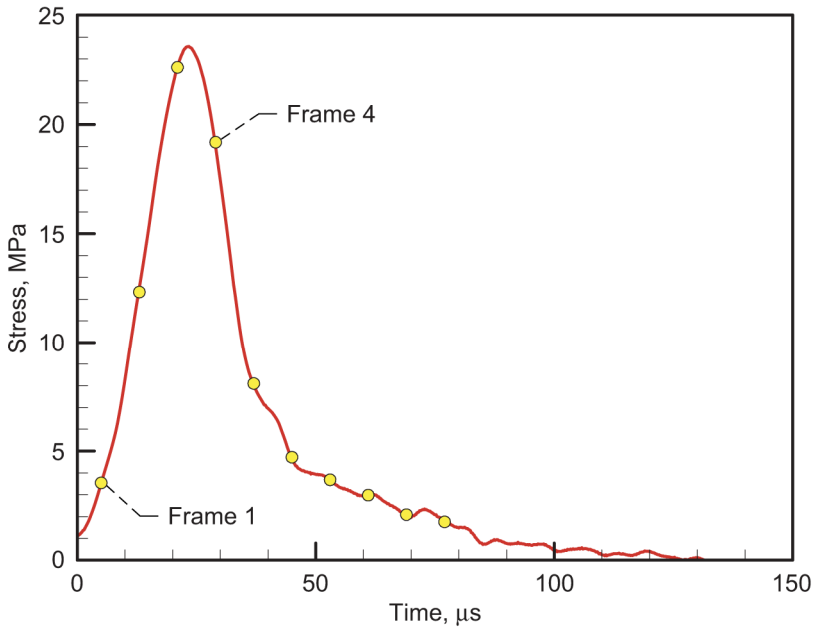

Figure 48.—Stress-time diagram for experiment 6SX–11 on single-crystal ice at –10 °C. Frame numbers correspond to those in figure 49.

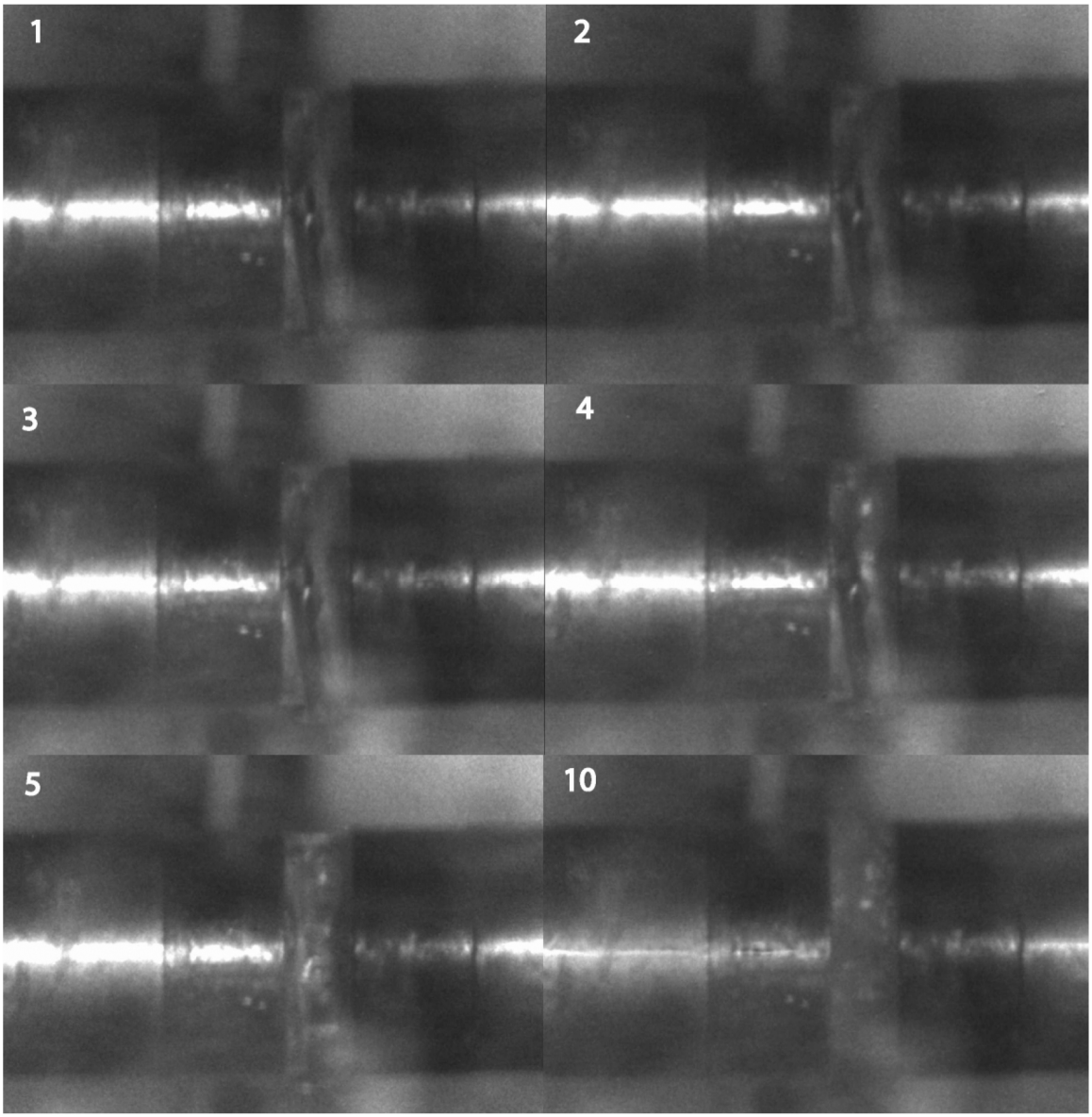

Figure 49.—High-speed camera images for experiment 6SX–11 on single-crystal ice at –10 °C with frame numbers indicated.

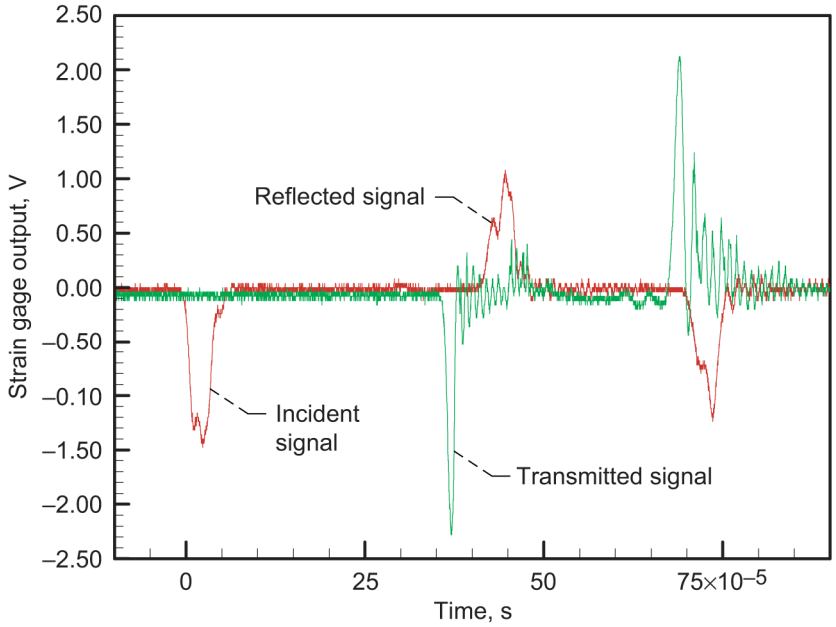

Figure 50.—Strain gage signals for experiment 6SX–12 on single-crystal ice at –10 °C.

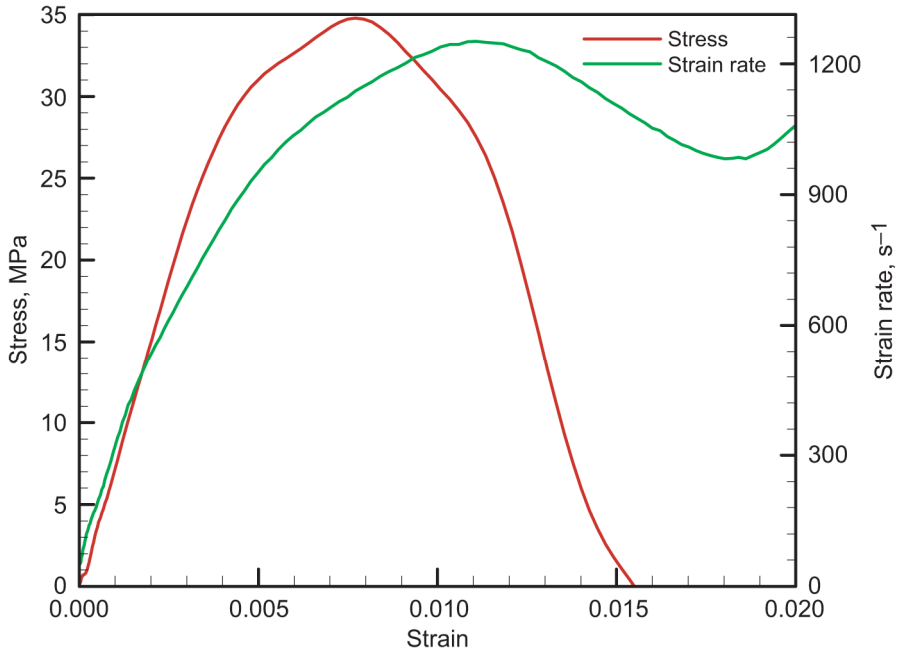

Figure 51.—Stress and strain rate versus strain curves for experiment 6SX–12 on single-crystal ice at –10 °C.

Appendix C
Experimental Results for HMD Series

Results for the multigrained ice samples tested with a modified split Hopkinson pressure bar apparatus at –10 °C are presented here in figures 52 through 85.

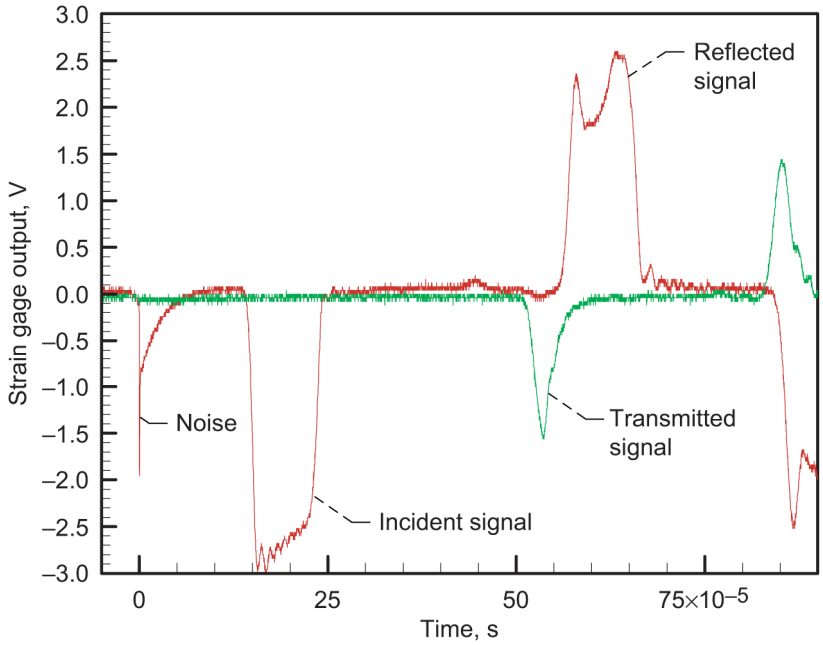

Figure 52.—Strain gage signals for experiment HMD003 on multigrained ice at –10 °C.

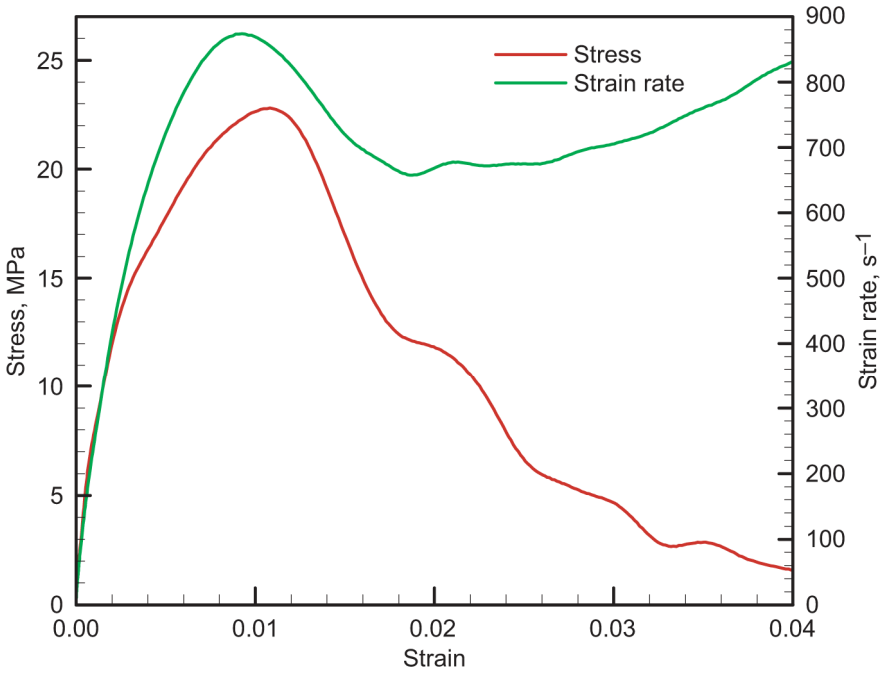

Figure 53.—Stress and strain rate versus strain curves for experiment HMD003 on multigrained ice at –10 °C.

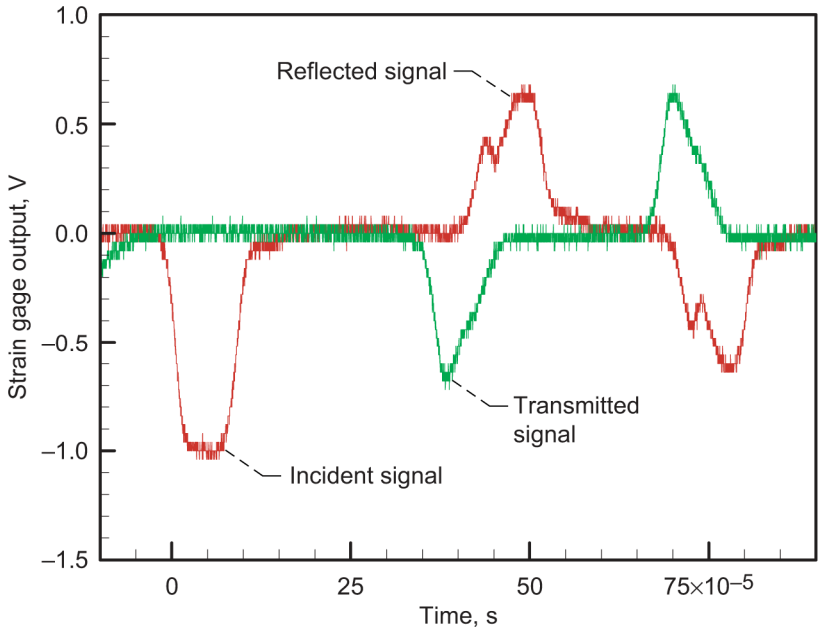

Figure 54.—Strain gage signals for experiment HMD006 on multigrained ice at –10 °C.

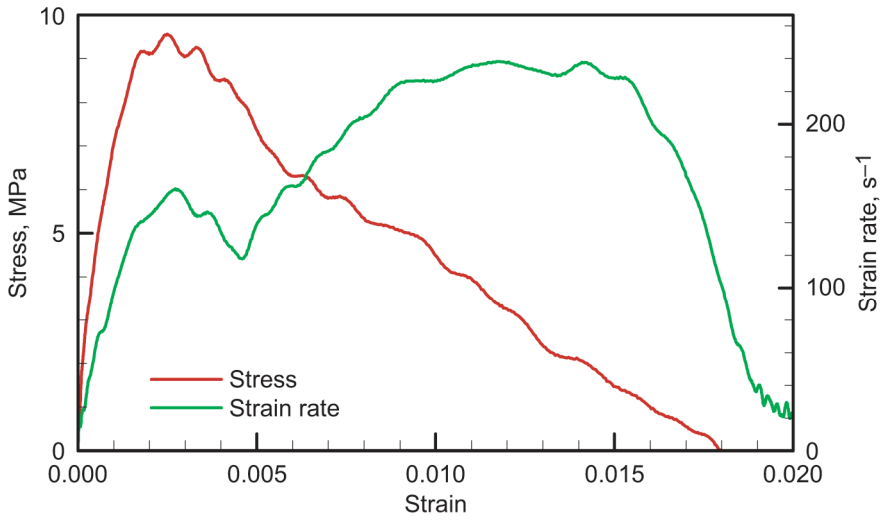

Figure 55.—Stress and strain rate versus strain curves for experiment HMD006 on multigrained ice at –10 °C.

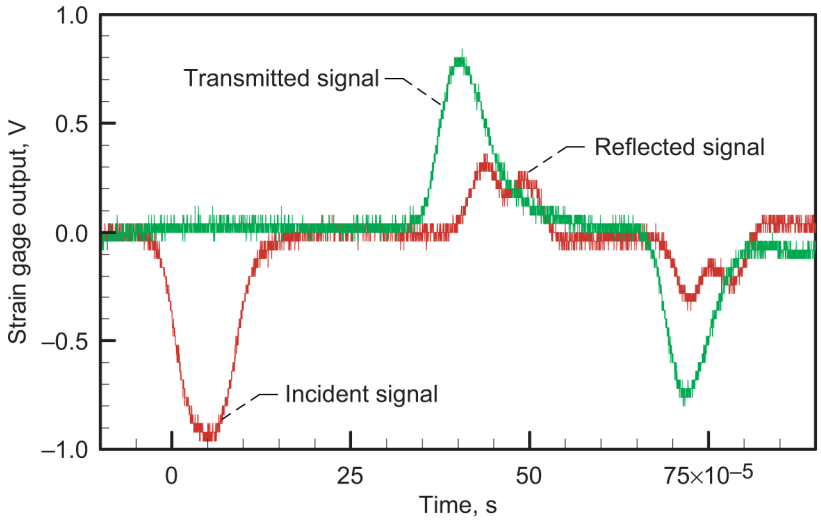

Figure 56.—Strain gage signals for experiment HMD008 on multigrained ice at –10 °C.

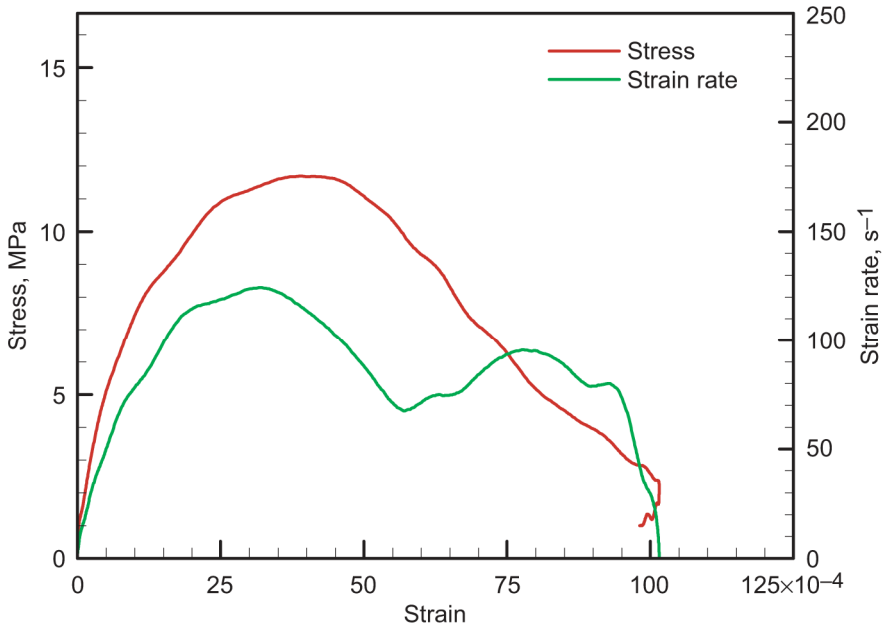

Figure 57.—Stress and strain rate versus strain curves for experiment HMD008 on multigrained ice at –10 °C.

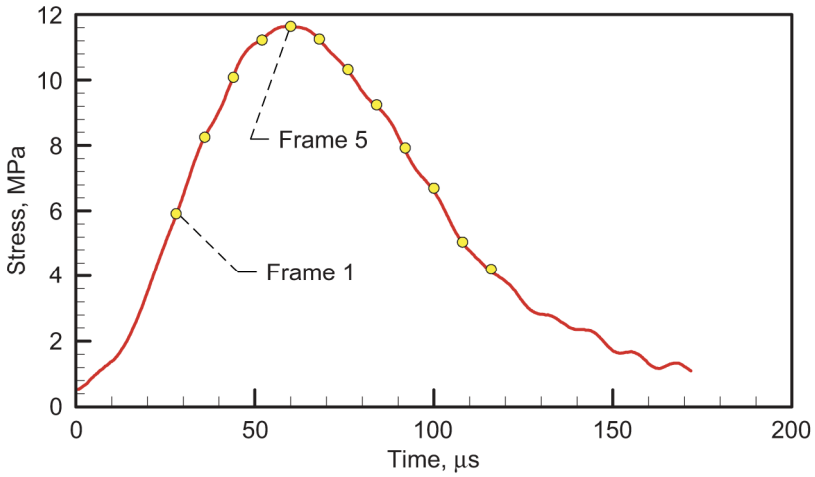

Figure 58.—Stress-time diagram for experiment HMD008 on multigrained ice at –10 °C. Frame numbers correspond to those in figure 59.

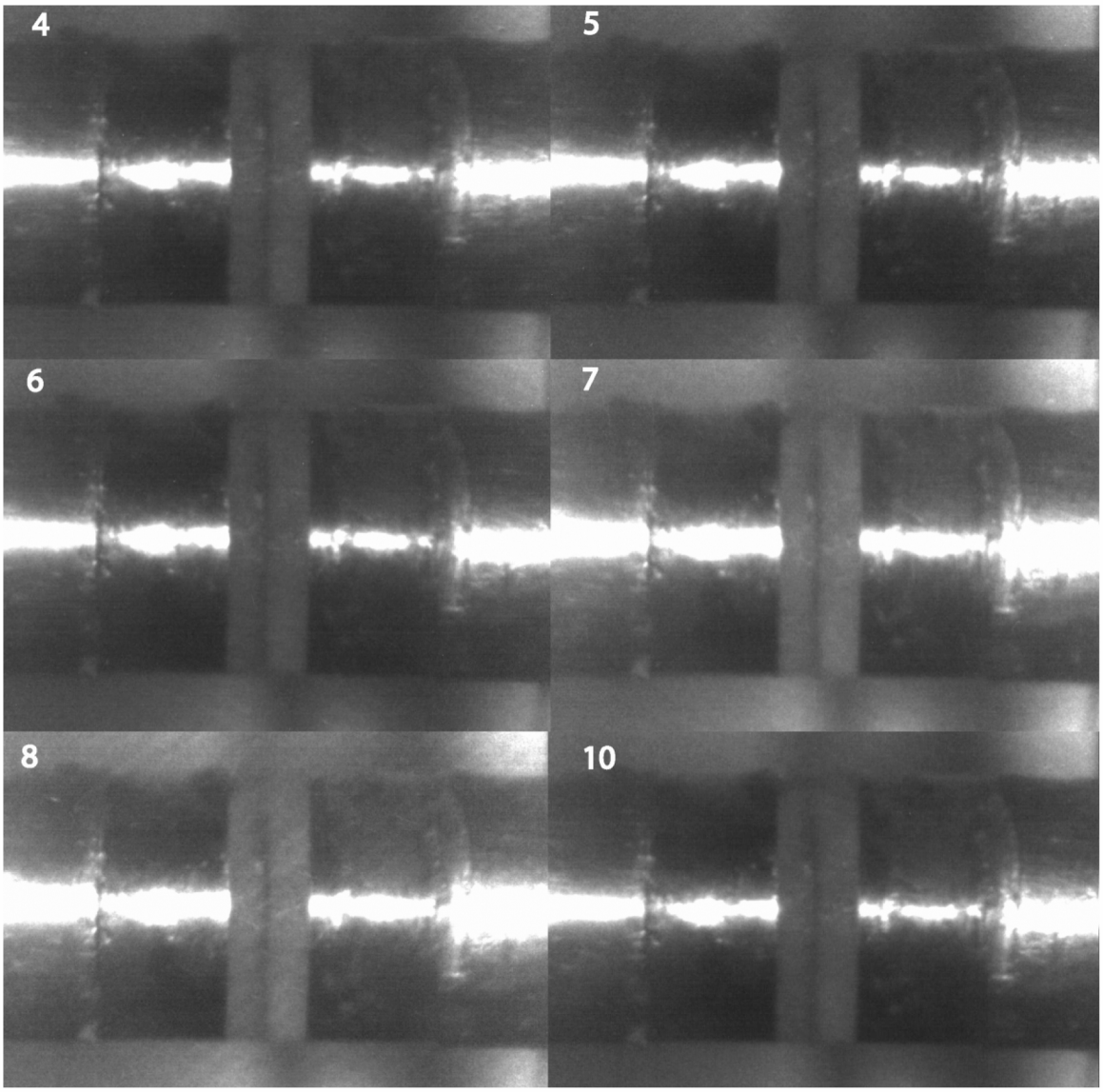

Figure 59.—High-speed camera images for experiment HMD008 on multigrained ice at –10 °C with frame numbers indicated.

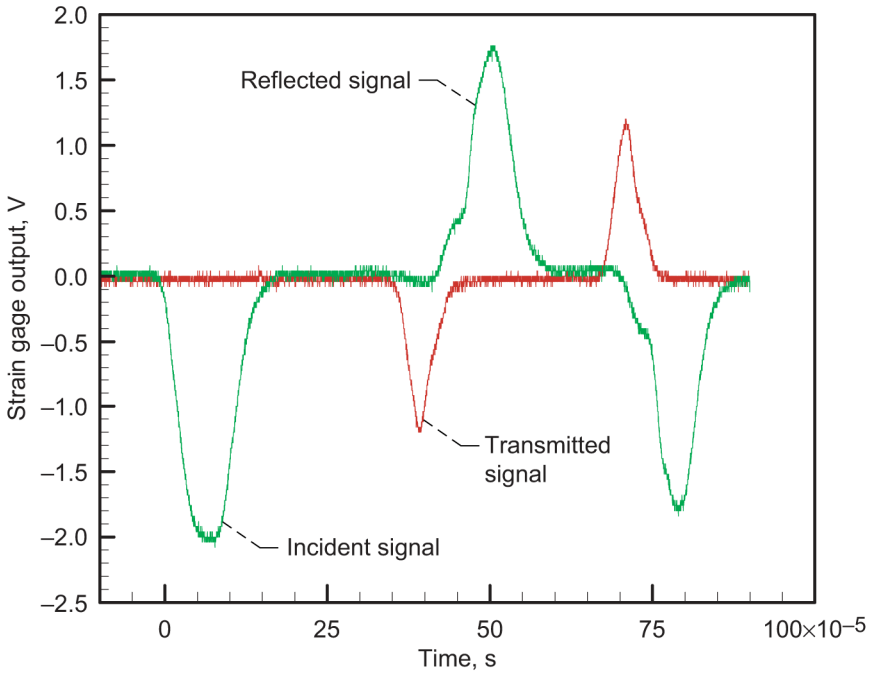

Figure 60.—Strain gage signals for experiment HMD016 on multigrained ice at –10 °C.

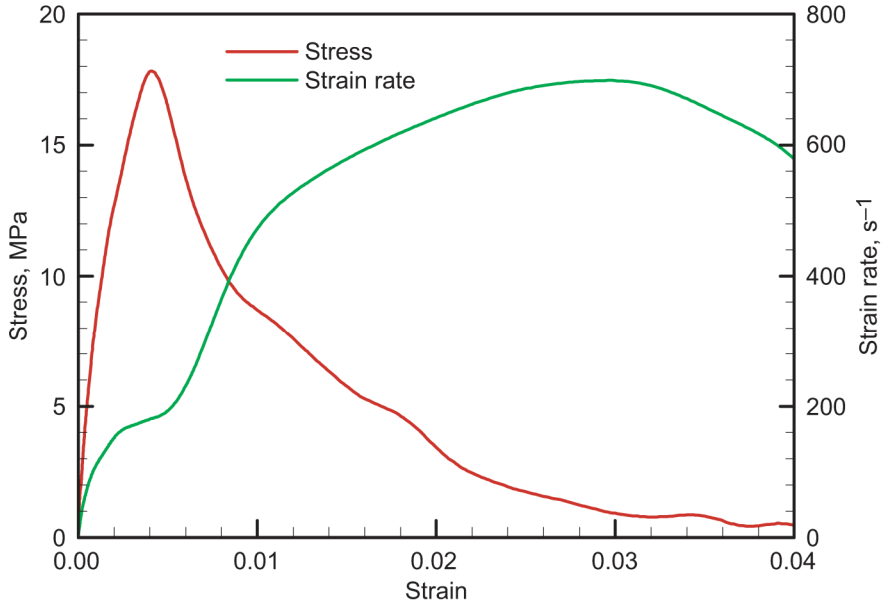

Figure 61.—Stress and strain rate versus strain curves for experiment HMD016 on multigrained ice at –10 °C.

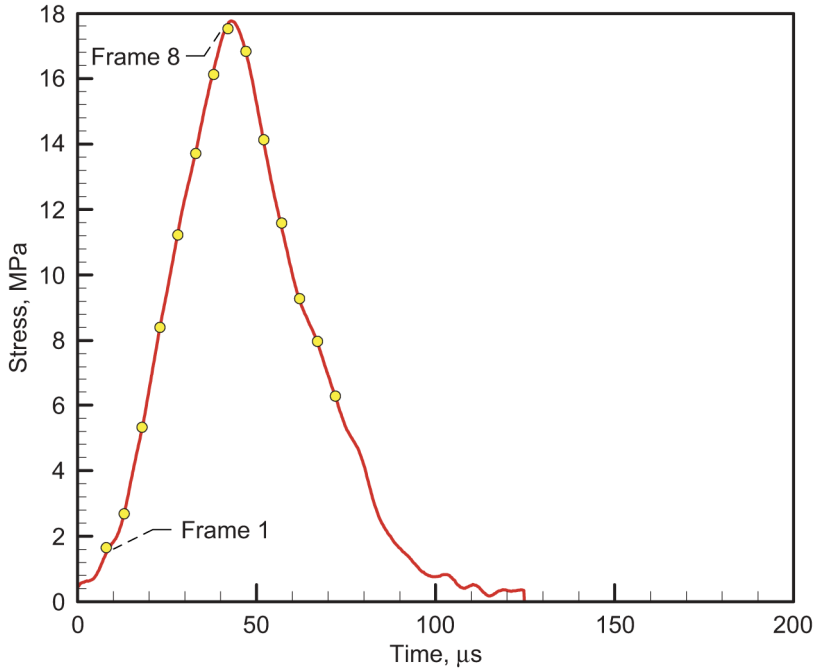

Figure 62.—Stress-time diagram for experiment HMD016 on multigrained ice at –10 °C. Frame numbers correspond to those in figure 63.

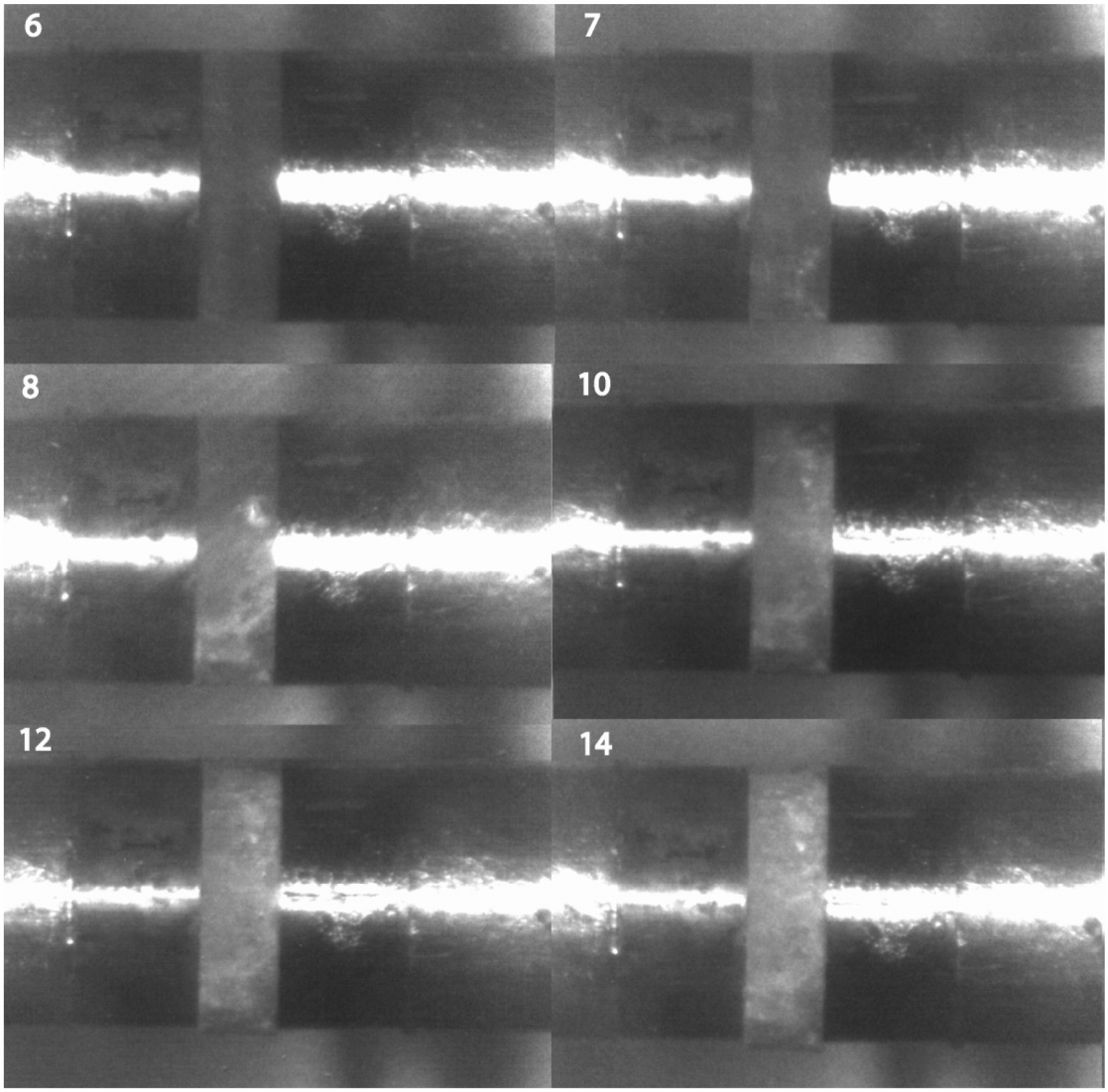

Figure 63.—High-speed camera images for experiment HMD016 on multigrained ice at –10 °C with frame numbers indicated.

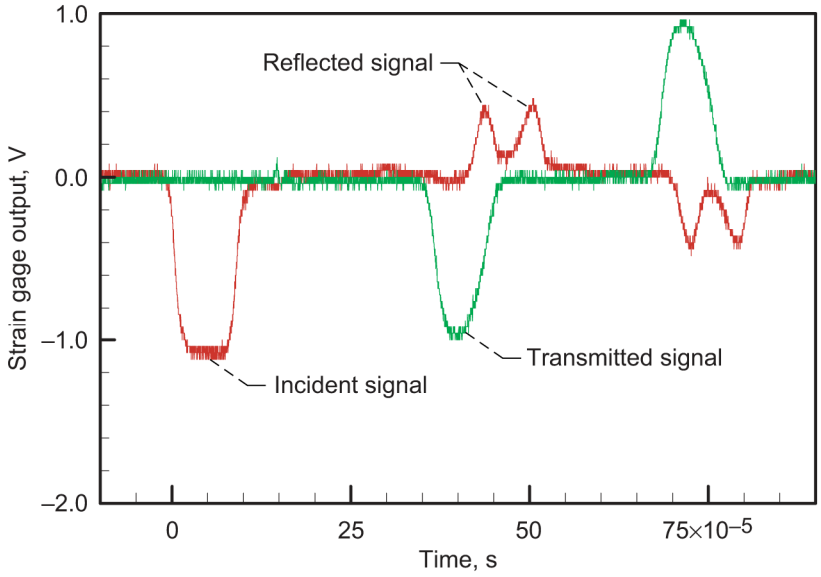

Figure 64.—Strain gage signals for experiment HMD0010 on multigrained ice at –10 °C.

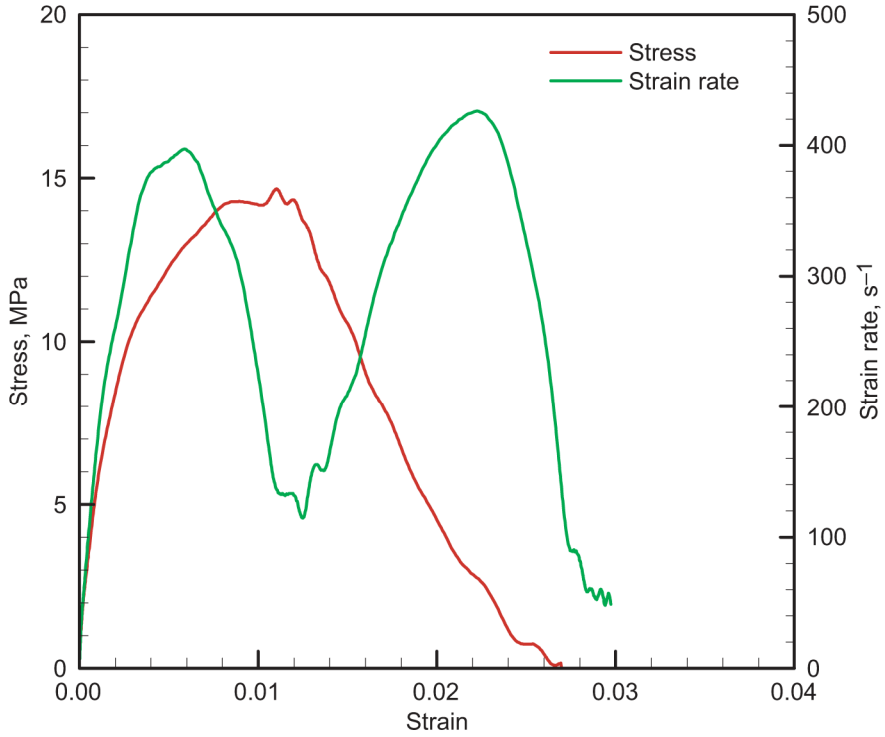

Figure 65.—Stress and strain rate versus strain curves for experiment HMD010 on multigrained ice at –10 °C.

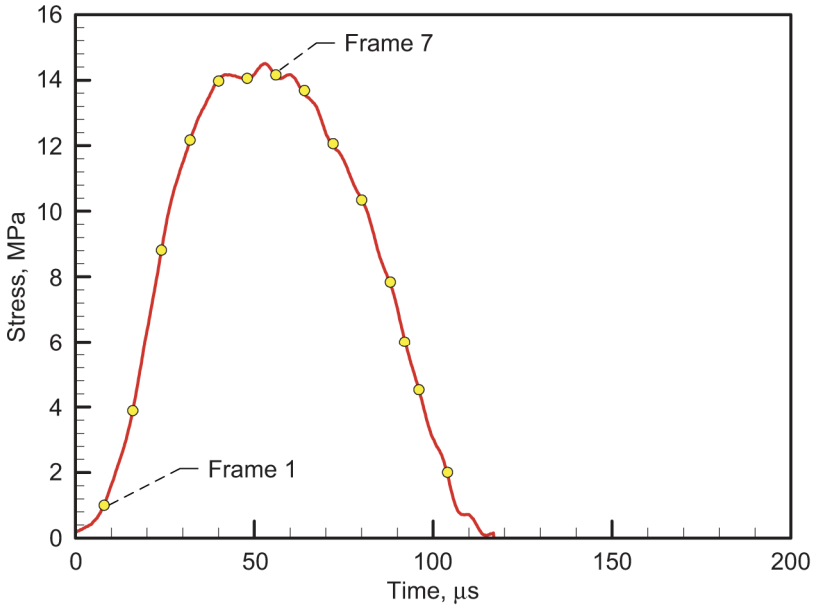

Figure 66.—Stress-time diagram for experiment HMD010 on multigrained ice at –10 °C. Frame numbers correspond to those in figure 67.

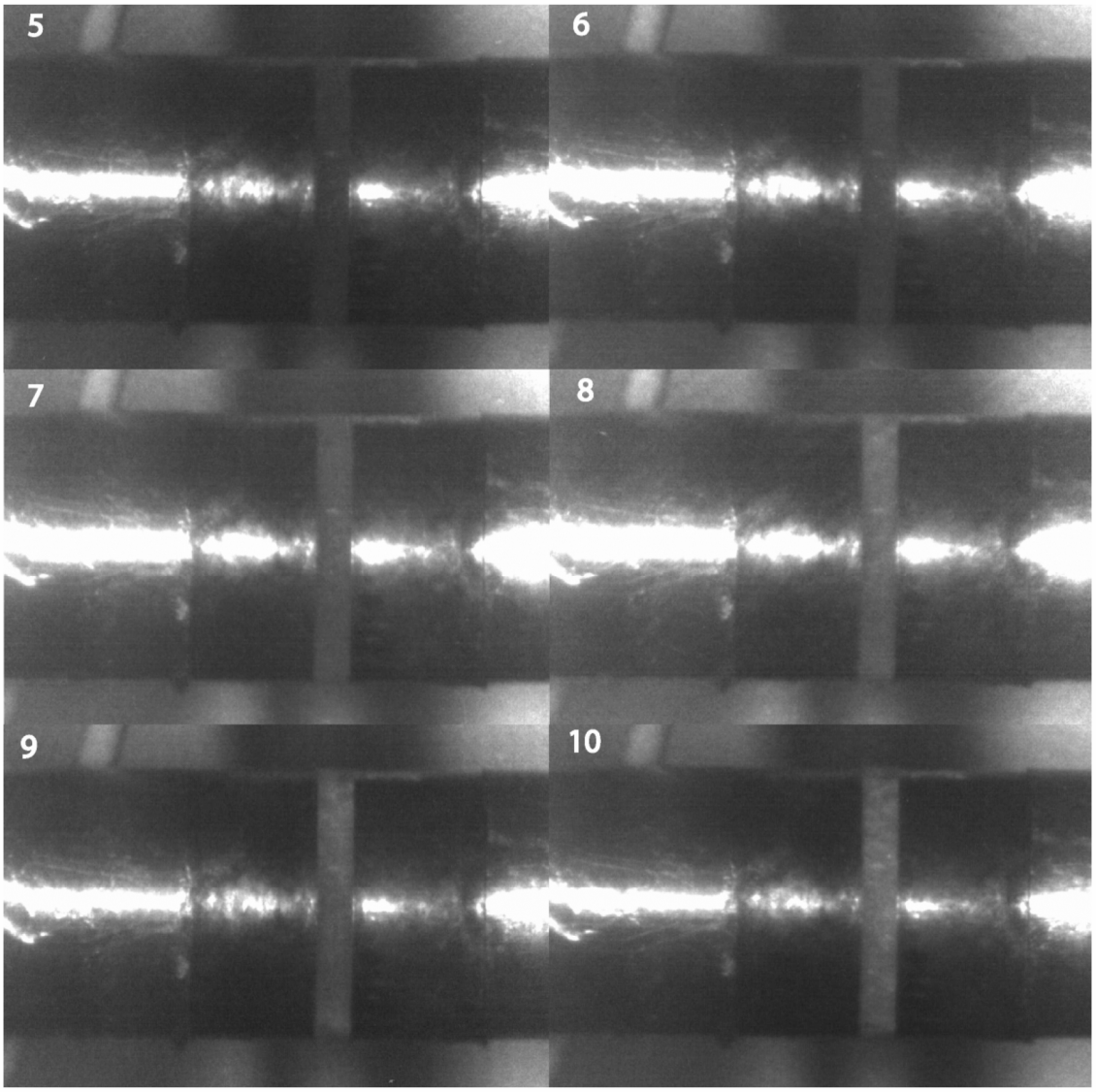

Figure 67.—High-speed camera images for experiment HMD010 on multigrained ice at –10 °C with frame numbers indicated.

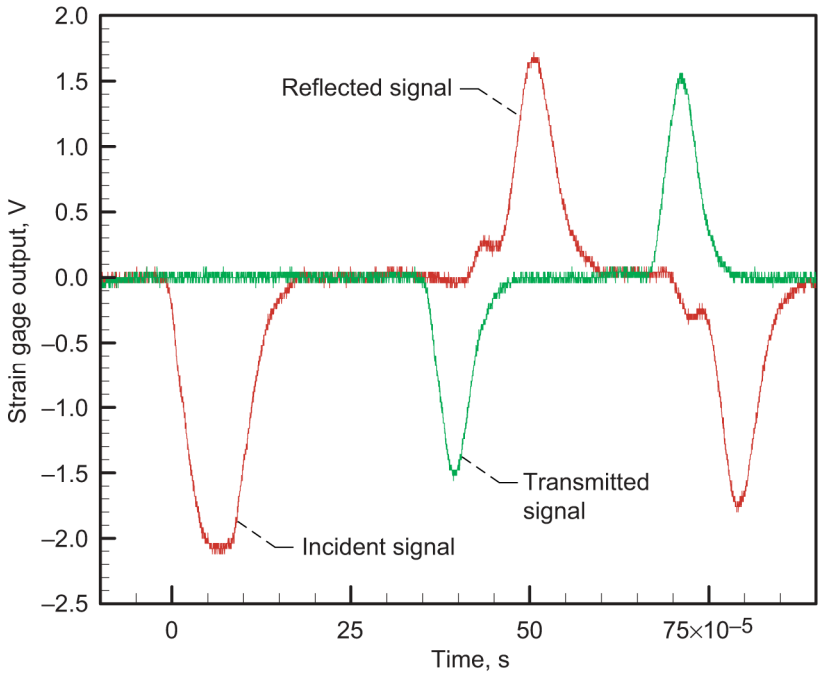

Figure 68.—Strain gage signals for experiment HMD011 on multigrained ice at –10 °C.

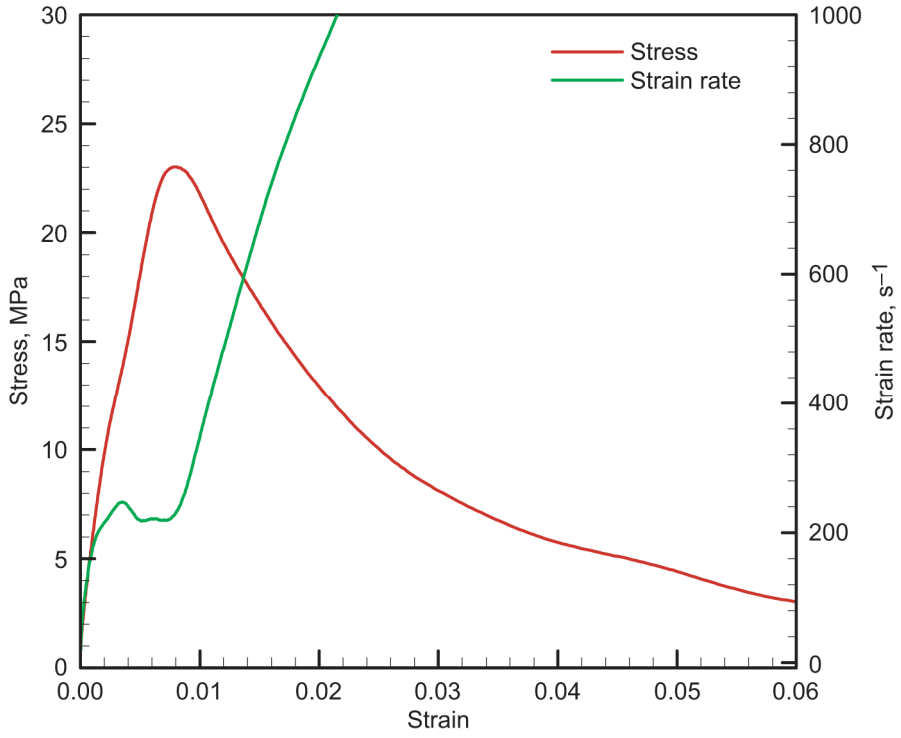

Figure 69.—Stress and strain rate versus strain curves for experiment HMD011 on multigrained ice at –10 °C.

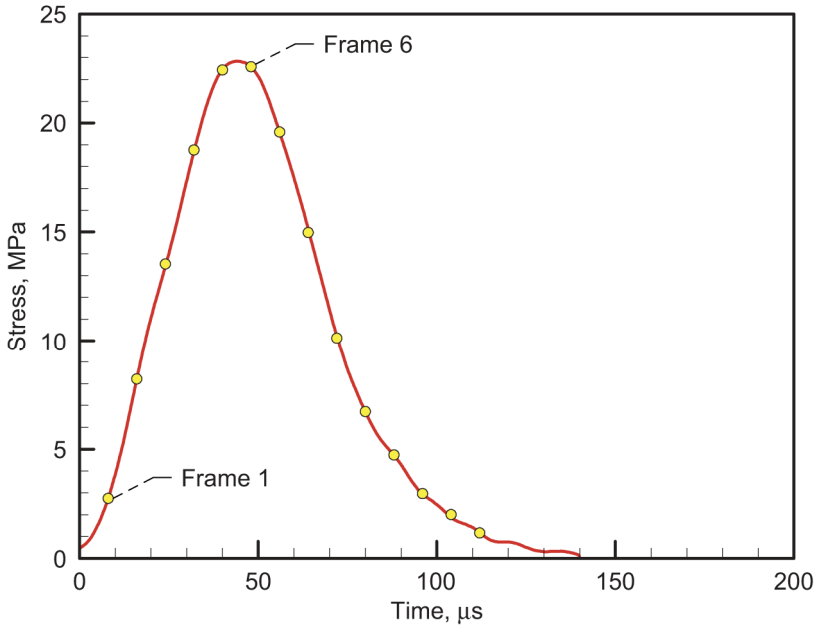

Figure 70.—Stress-time diagram for experiment HMD011 on multigrained ice at –10 °C. Frame numbers correspond to those in figure 71.

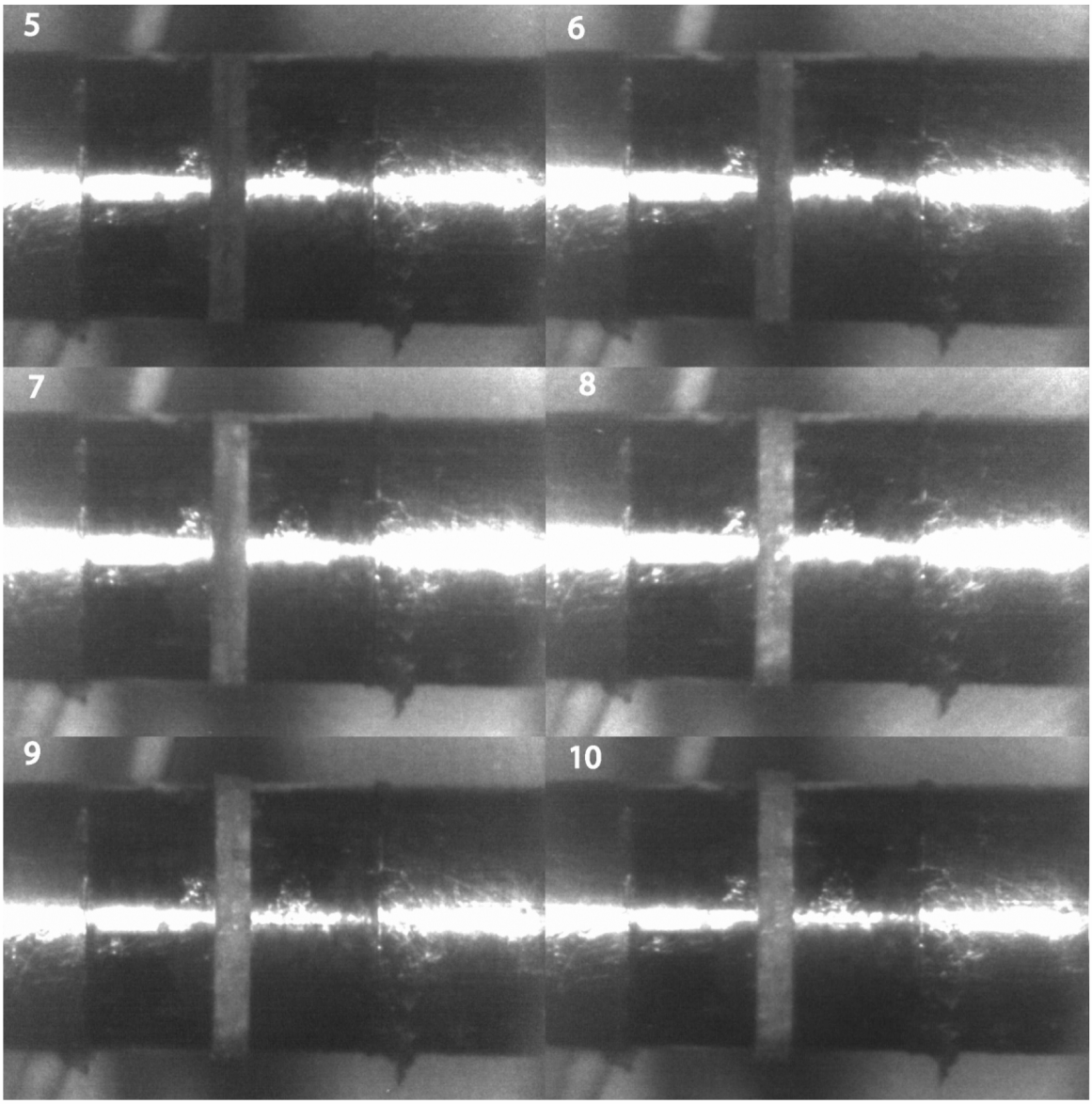

Figure 71.—High-speed camera images for experiment HMD011 on multigrained ice at –10 °C with frame numbers indicated.

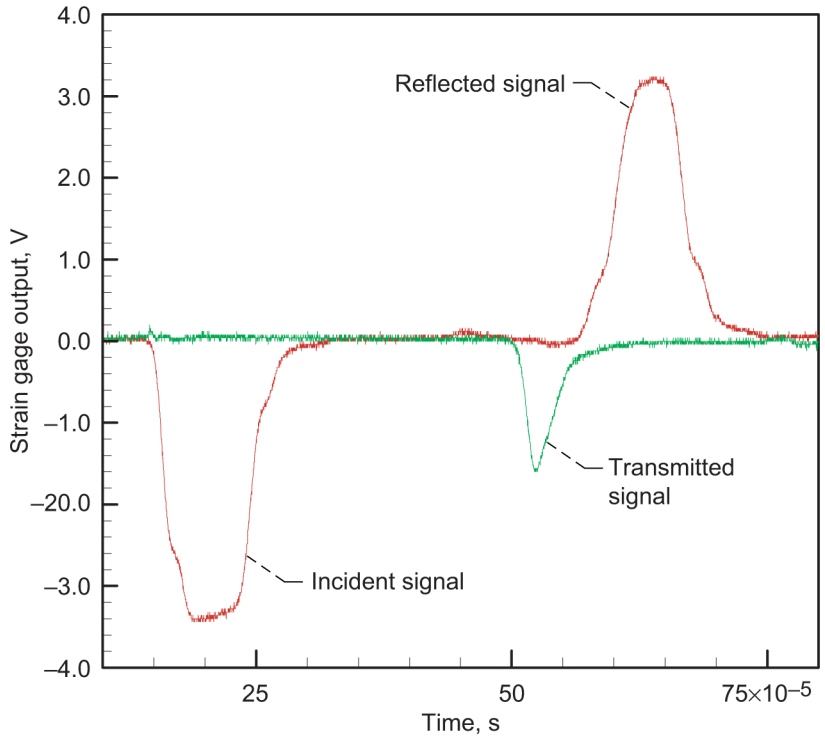

Figure 72.—Strain gage signals for experiment HMD014 on multigrained ice at –10 °C.

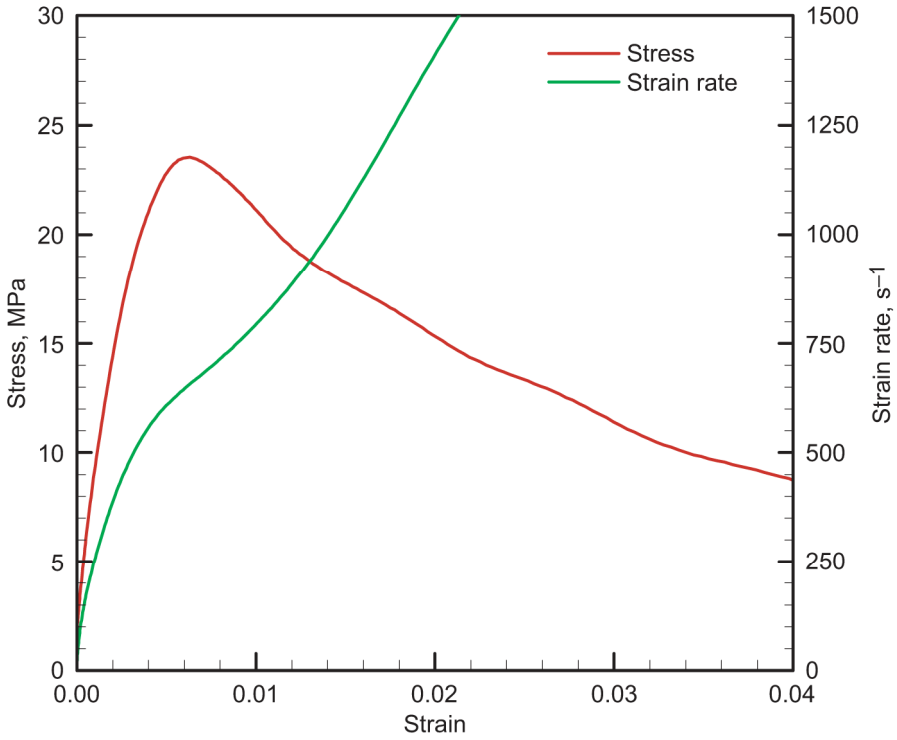

Figure 73.—Stress and strain rate versus strain curves for experiment HMD014 on multigrained ice at –10 °C.

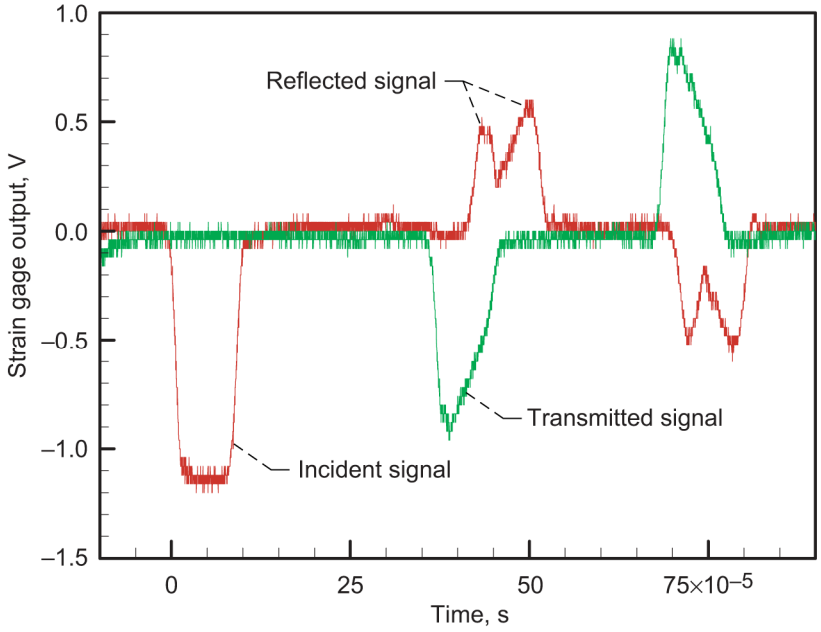

Figure 74.—Strain gage signals for experiment HMD018 on multigrained ice at –10 °C.

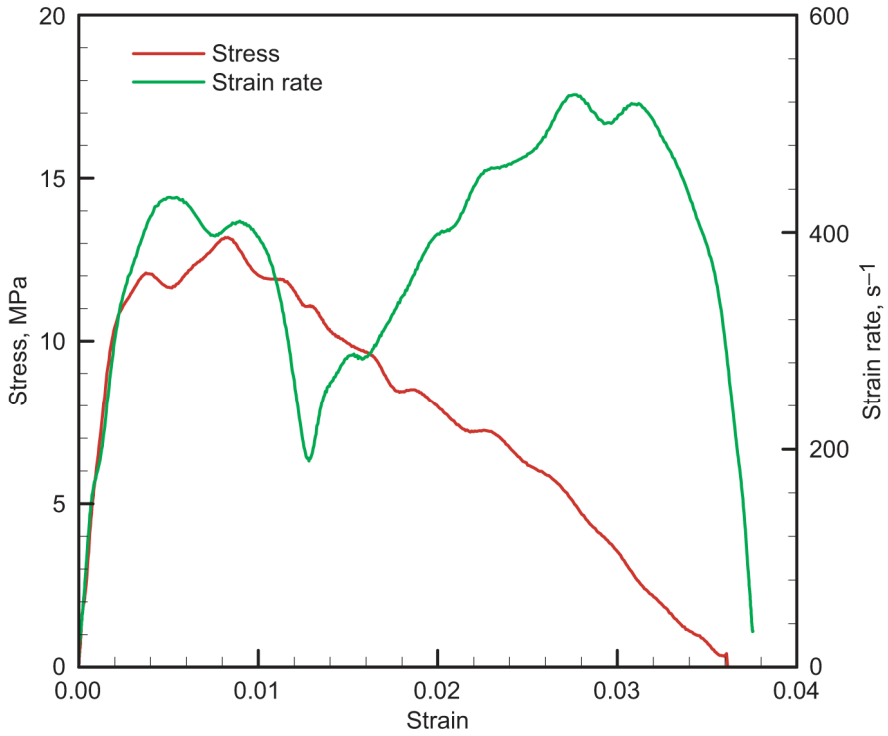

Figure 75.—Stress and strain rate versus strain curves for experiment HMD018 on multigrained ice at –10 °C.

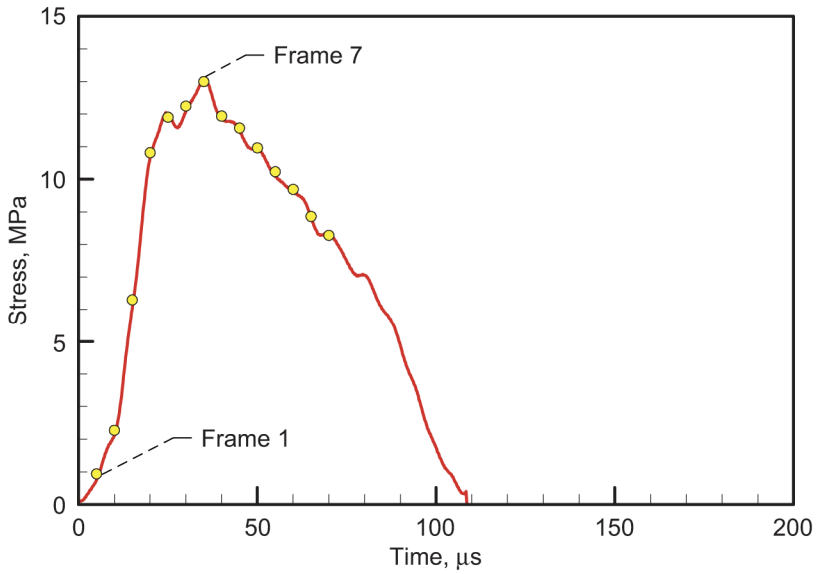

Figure 76.—Stress-time diagram for experiment HMD018 on multigrained ice at –10 °C. Frame numbers correspond to those in figure 77.

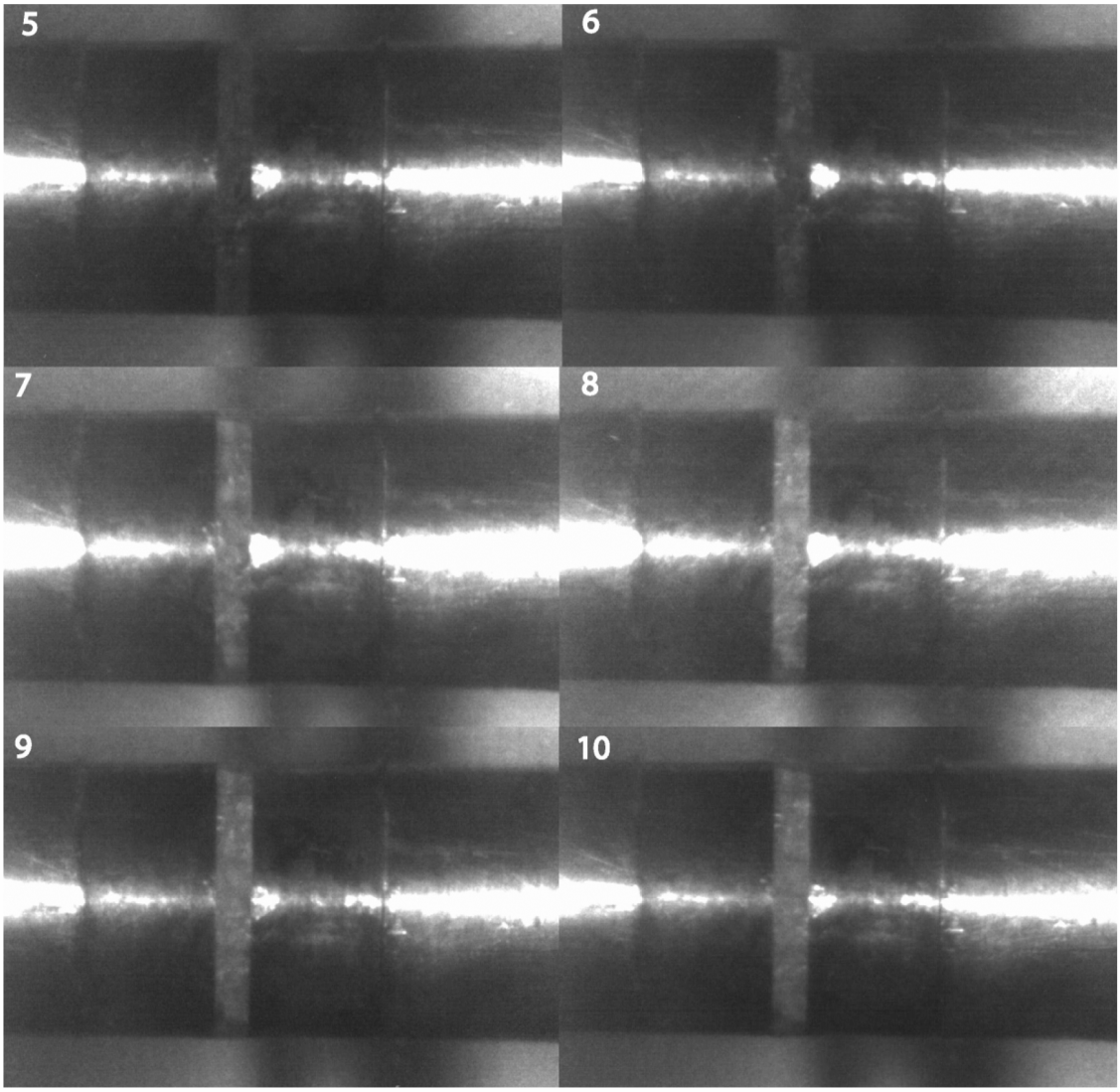

Figure 77.—High-speed camera images for experiment HMD018 on multigrained ice at –10 °C with frame numbers indicated.

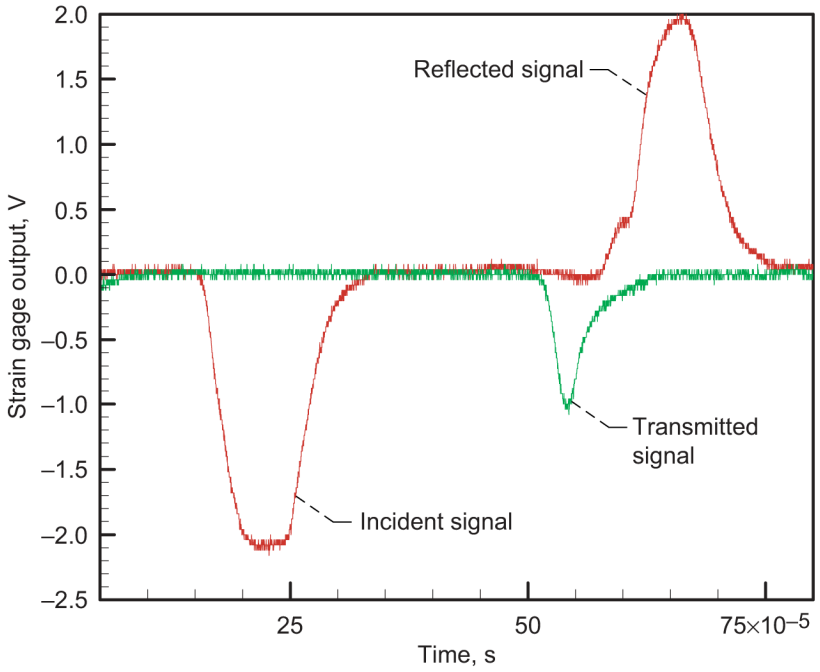

Figure 78.—Strain gage signals for experiment HMD019 on multigrained ice at –10 °C.

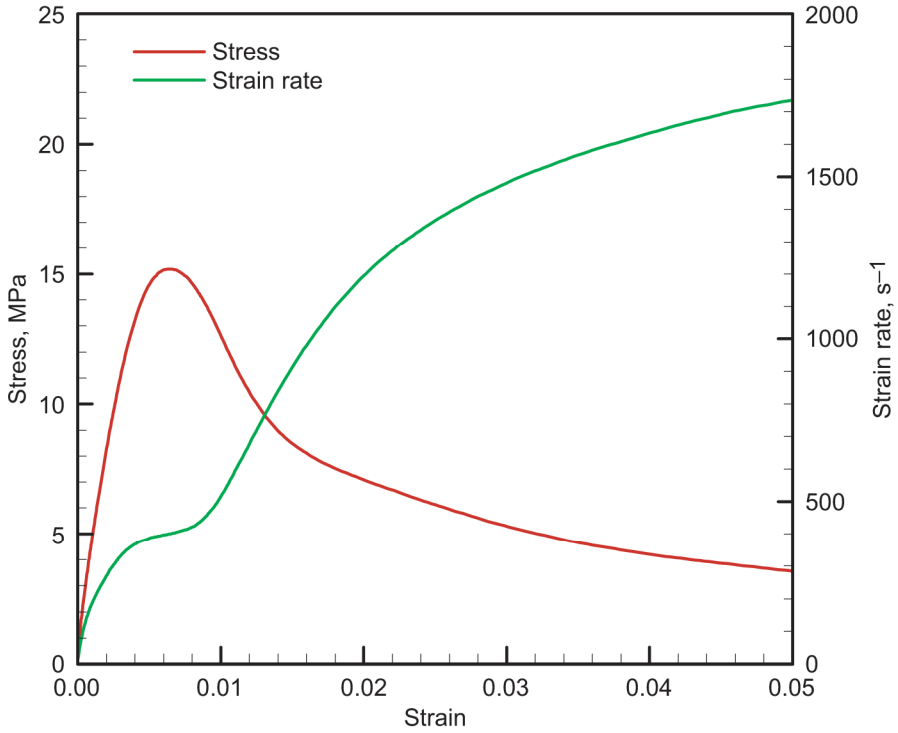

Figure 79.—Stress and strain rate versus strain curves for experiment HMD019 on multigrained ice at –10 °C.

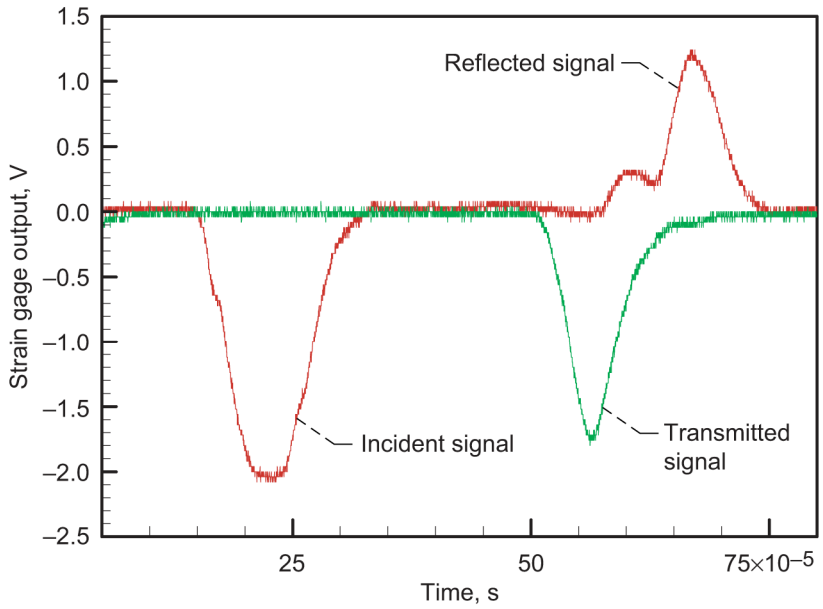

Figure 80.—Strain gage signals for experiment HMD022 on multigrained ice at –10 °C.

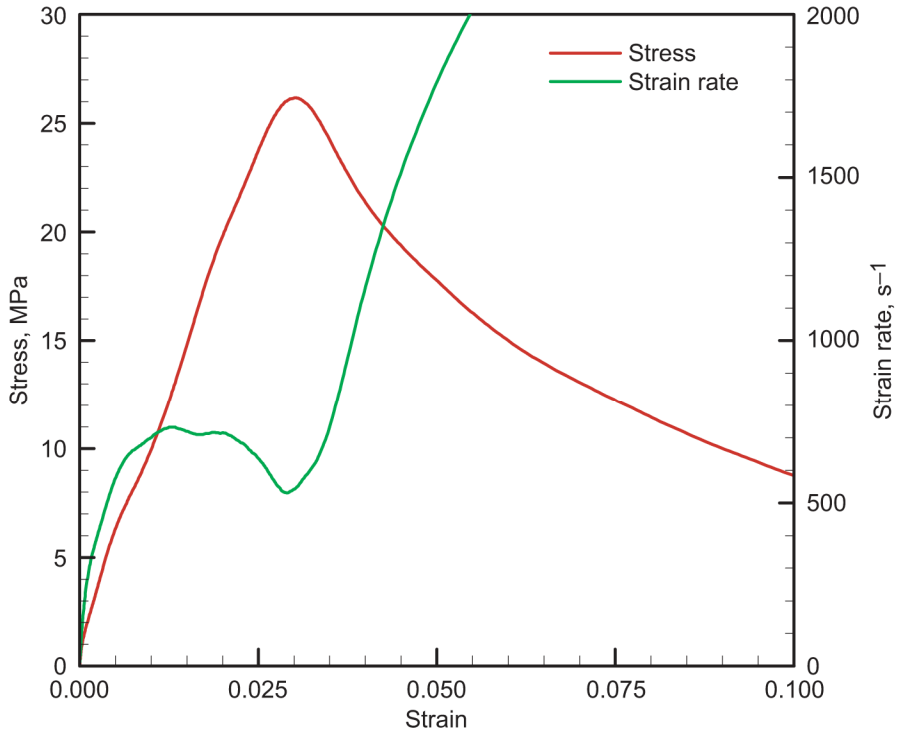

Figure 81.—Stress and strain rate versus strain curves for experiment HMD022 on multigrained ice at –10 °C.

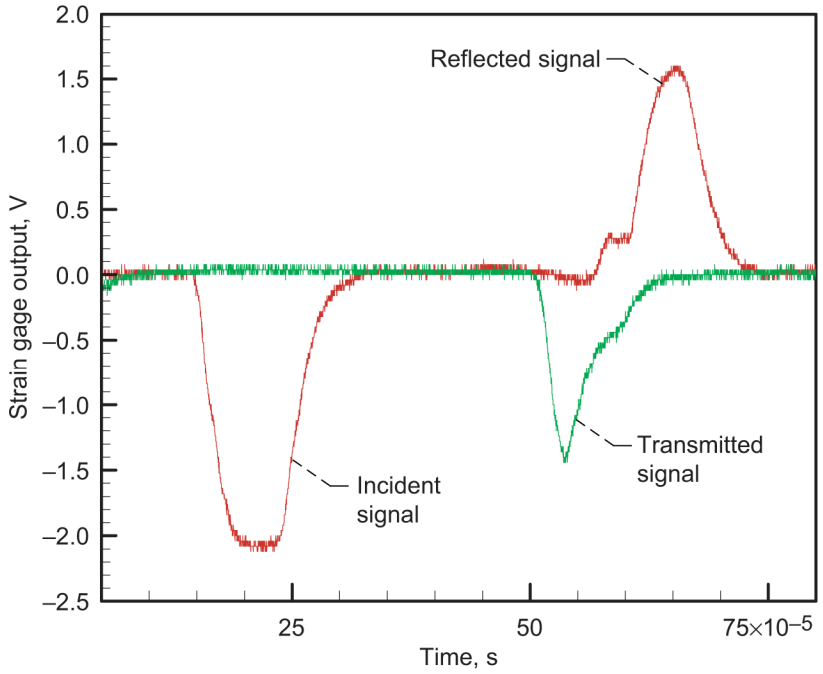

Figure 82.—Strain gage signals for experiment HMD024 on multigrained ice at –10 °C.

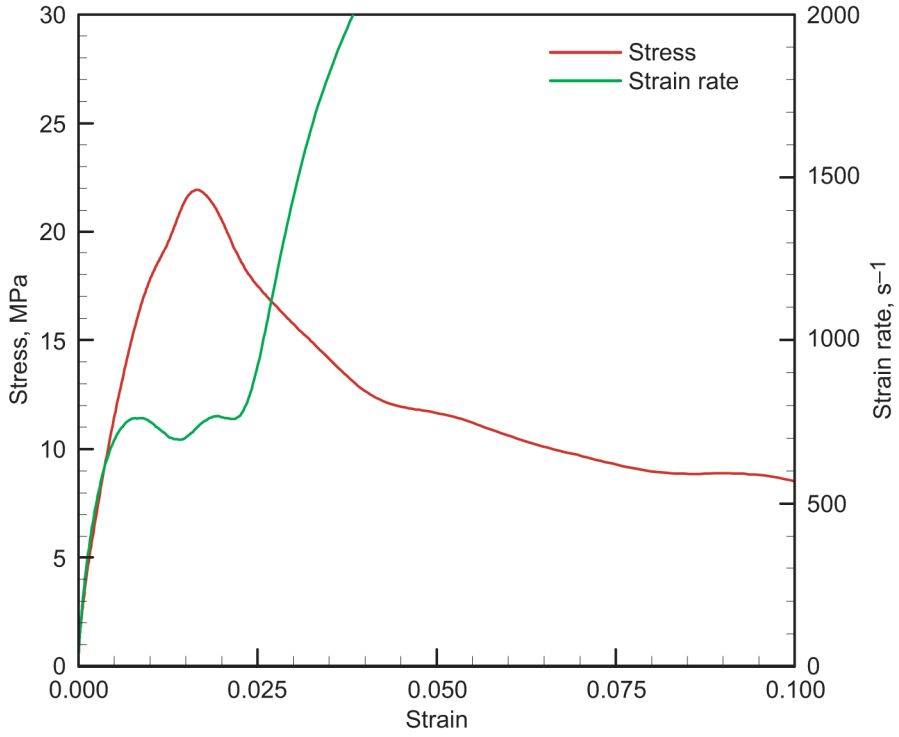

Figure 83.—Stress and strain rate versus strain curves for experiment HMD024 on multigrained ice at –10 °C.

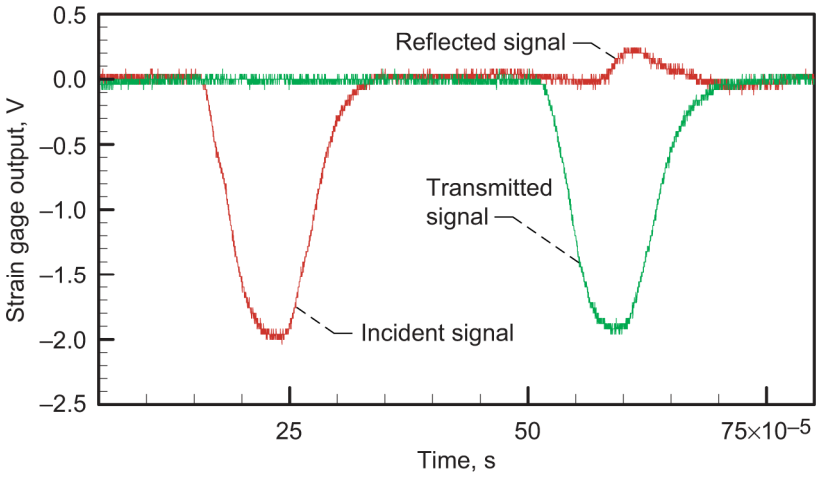

Figure 84.—Strain gage signals for experiment HMD027 on multigrained ice at –10 °C.

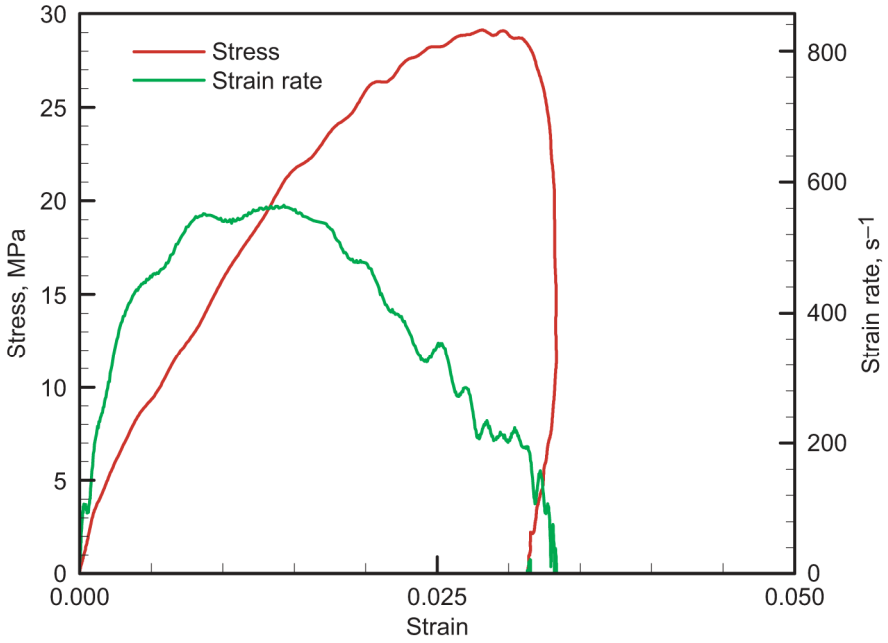

Figure 85.—Stress and strain rate versus strain curves for experiment HMD027 on multigrained ice at –10 °C.

Appendix D
Experimental Results for 14SX Series

Results for the multigrained ice samples tested with a modified split Hopkinson pressure bar apparatus at –10 °C investigating end constraints are presented here in figures 86 through 97.

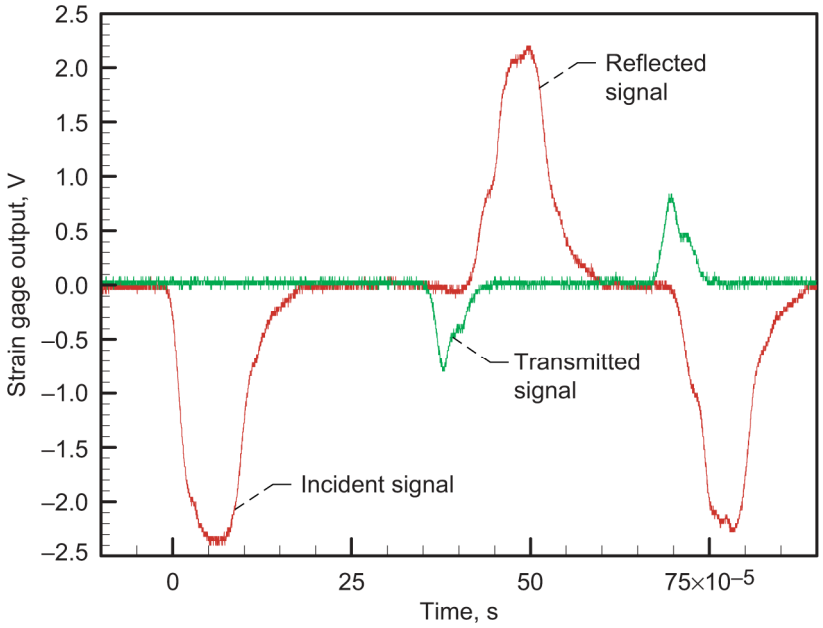

Figure 86.—Strain gage signals for experiment 14SX–02 on multigrained ice with constrained ends at –10 °C.

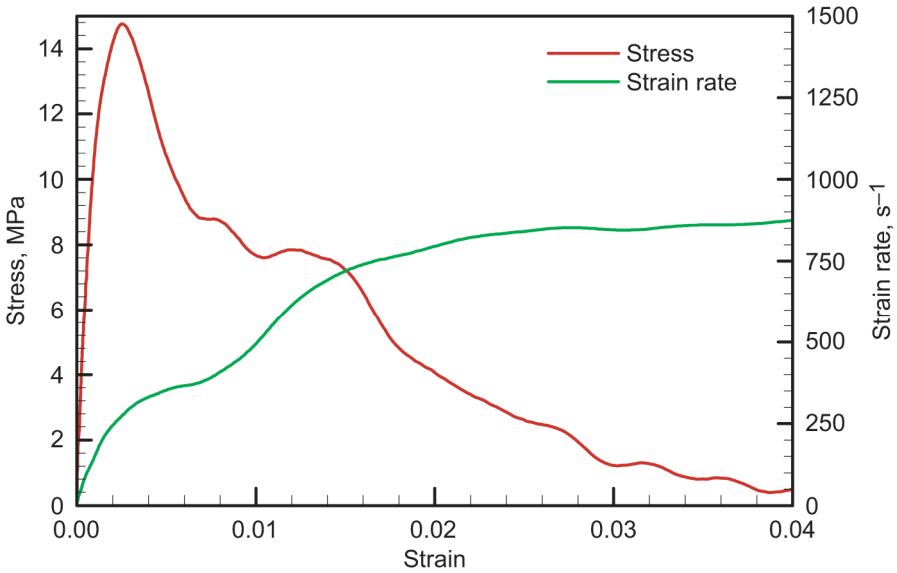

Figure 87.—Stress and strain rate versus strain curves for experiment 14SX–02 on multigrained ice with constrained ends at –10 °C.

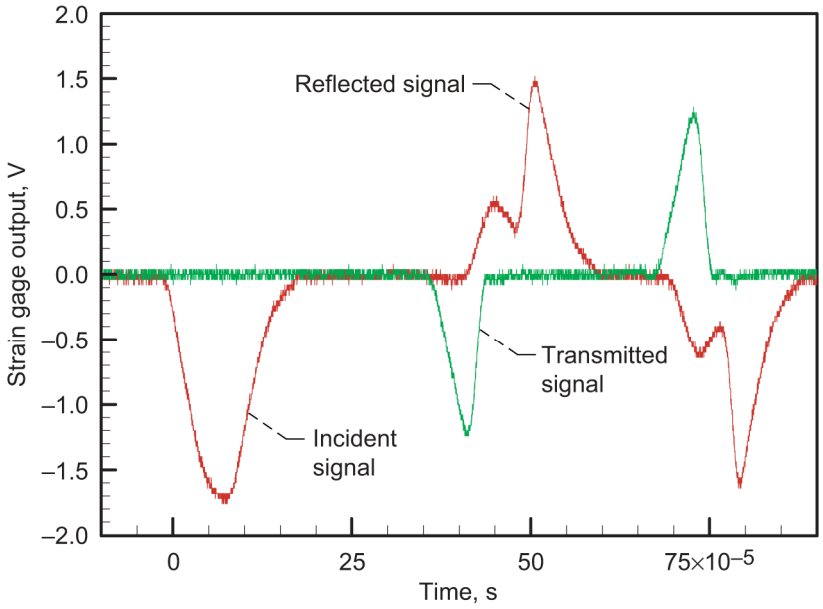

Figure 88.—Strain gage signals for experiment 14SX–03 on multigrained ice with constrained ends at –10 °C.

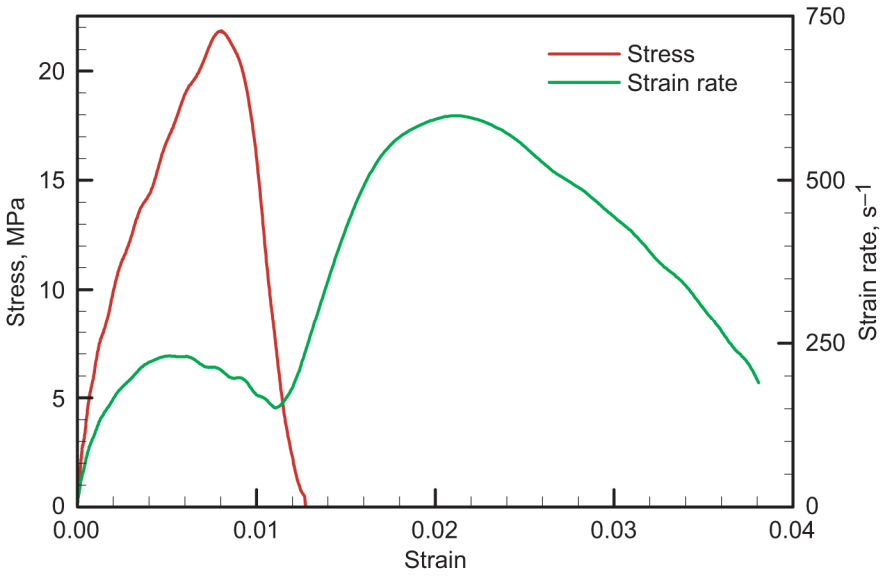

Figure 89.—Stress and strain rate versus strain curves for experiment 14SX–03 on multigrained ice with constrained ends at –10 °C.

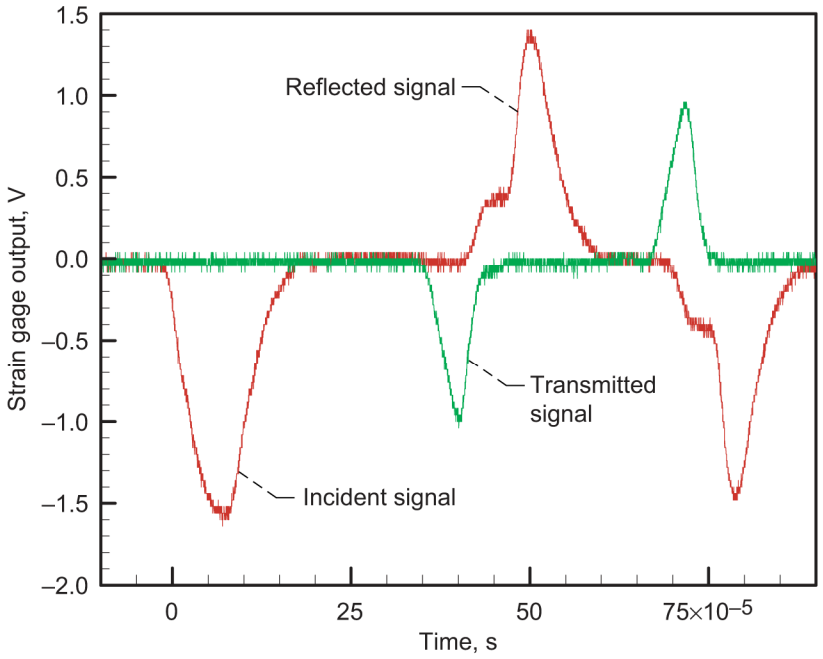

Figure 90.—Strain gage signals for experiment 14SX–06 on multigrained ice with constrained ends at –10 °C.

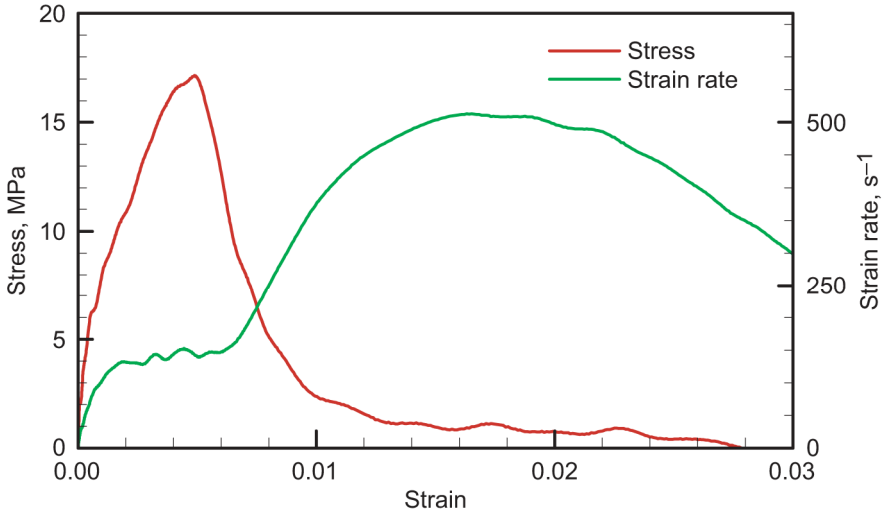

Figure 91.—Stress and strain rate versus strain curves for experiment 14SX–06 on multigrained ice with constrained ends at –10 °C.

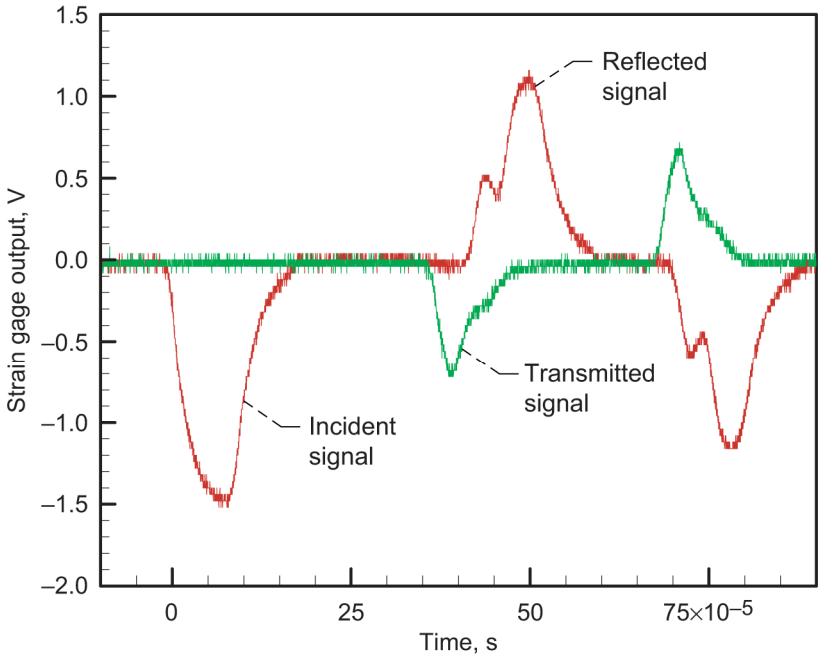

Figure 92.—Strain gage signals for experiment 14SX–07 on multigrained ice with constrained ends at –10 °C.

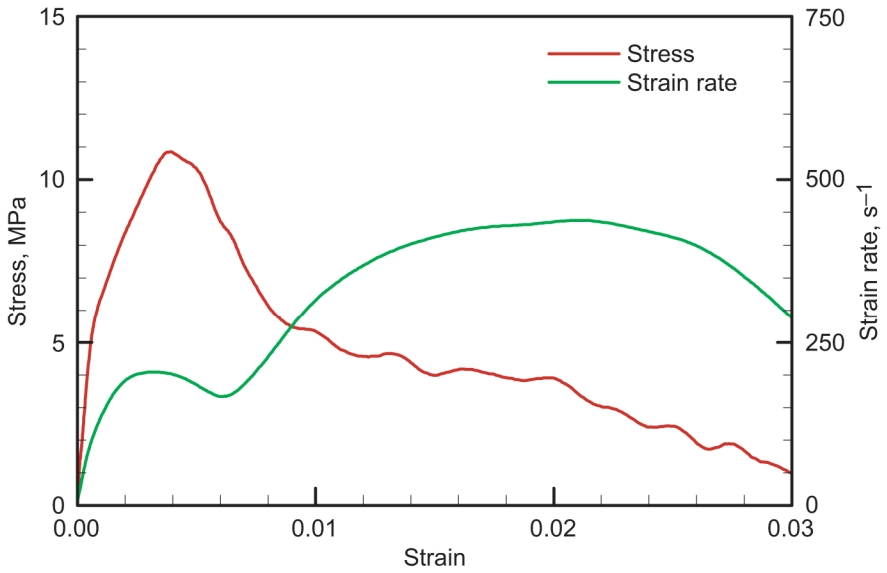

Figure 93.—Stress and strain rate versus strain curves for experiment 14SX–07 on multigrained ice with constrained ends at –10 °C.

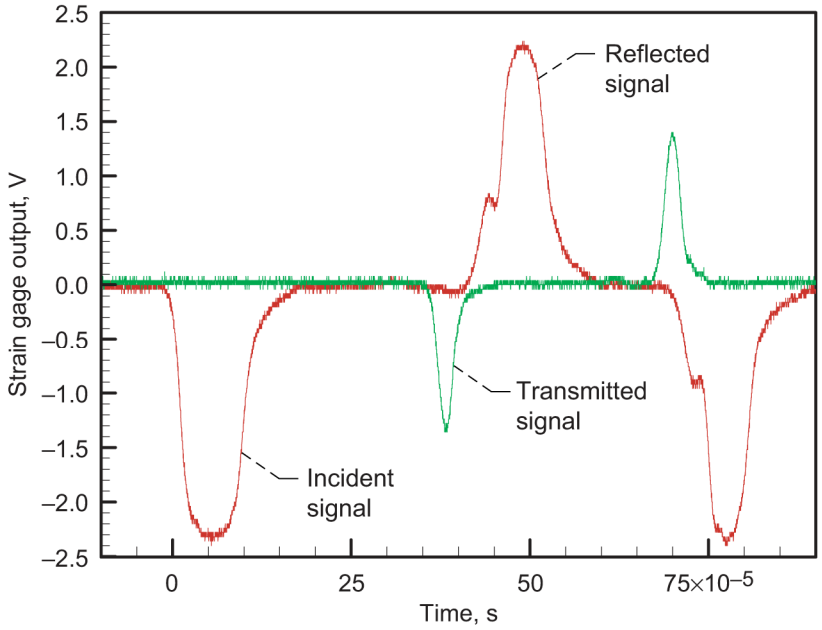

Figure 94.—Strain gage signals for experiment 14SX–09 on multigrained ice with constrained ends at –10 °C.

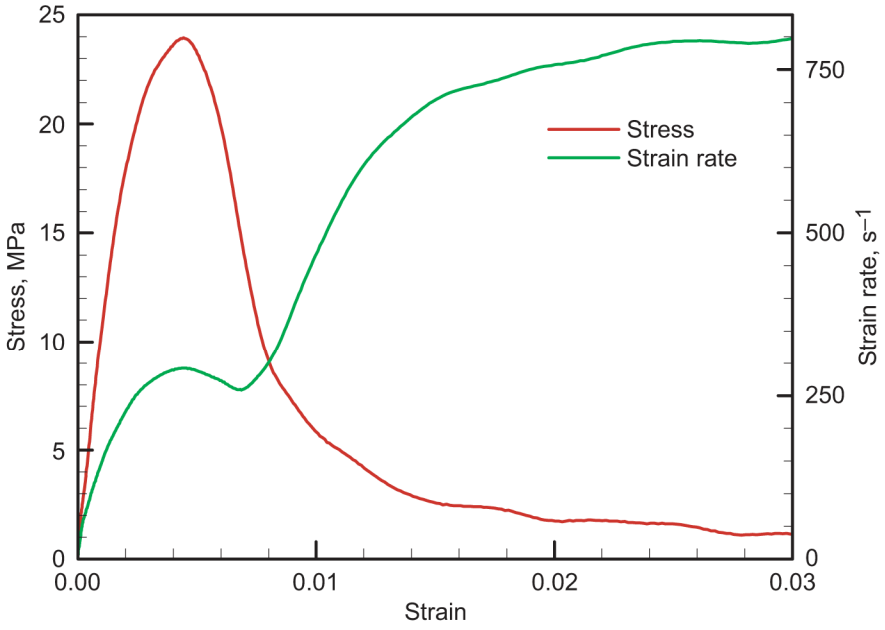

Figure 95.—Stress and strain rate versus strain curves for experiment 14SX–09 on multigrained ice with constrained ends at –10 °C.

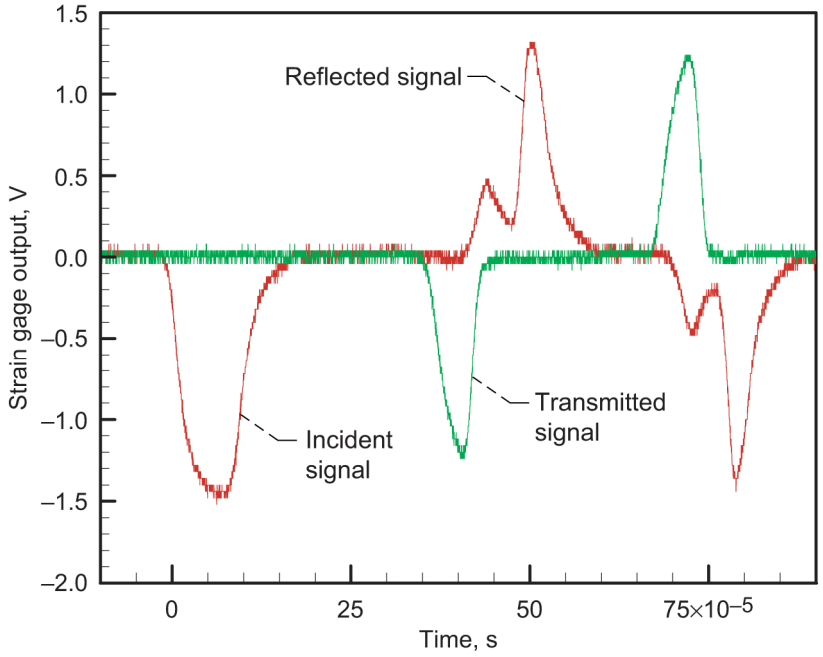

Figure 96.—Strain gage signals for experiment 14SX–18 on multigrained ice with constrained ends at –10 °C.

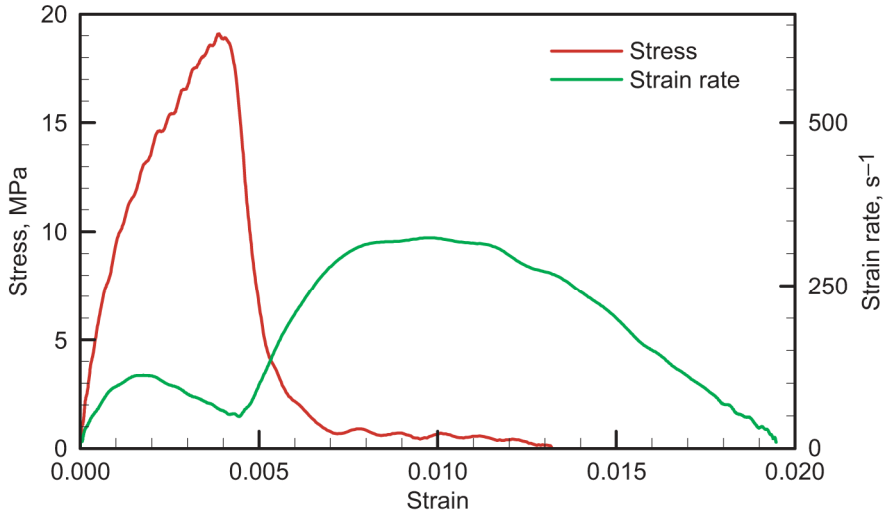

Figure 97.—Stress and strain rate versus strain curves for experiment 14SX–18 on multigrained ice with constrained ends at –10 °C.

Appendix E
Experimental Results for Specimens Tested at –30 °C

Results for the multigrained ice samples tested with a modified split Hopkinson pressure bar apparatus at –30 °C are presented here in figures 98 through 123.

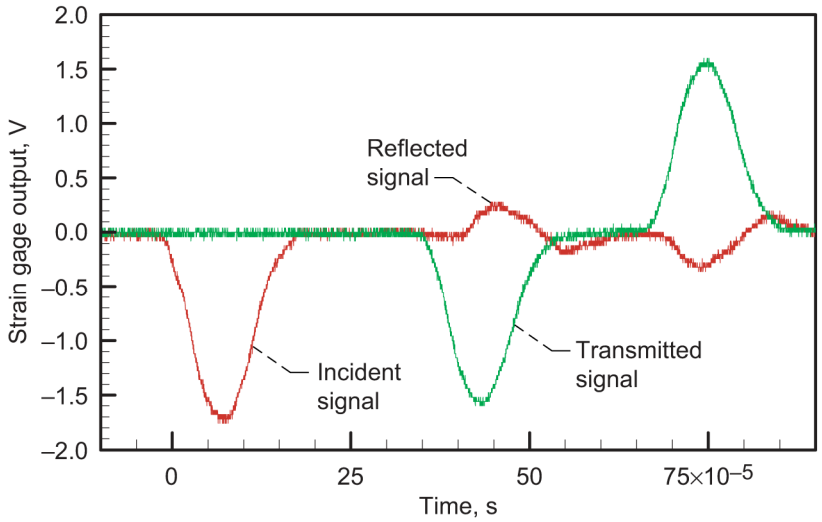

Figure 98.—Strain gage signals for experiment Test 1 on multigrained ice at –30 °C.

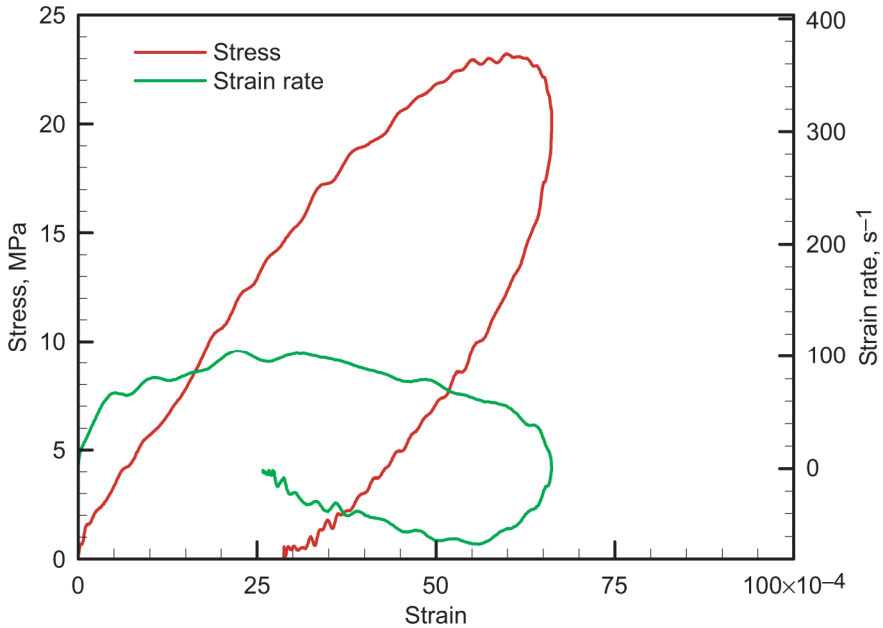

Figure 99.—Stress and strain rate versus strain curves for experiment Test 1 on multigrained ice at –30 °C.

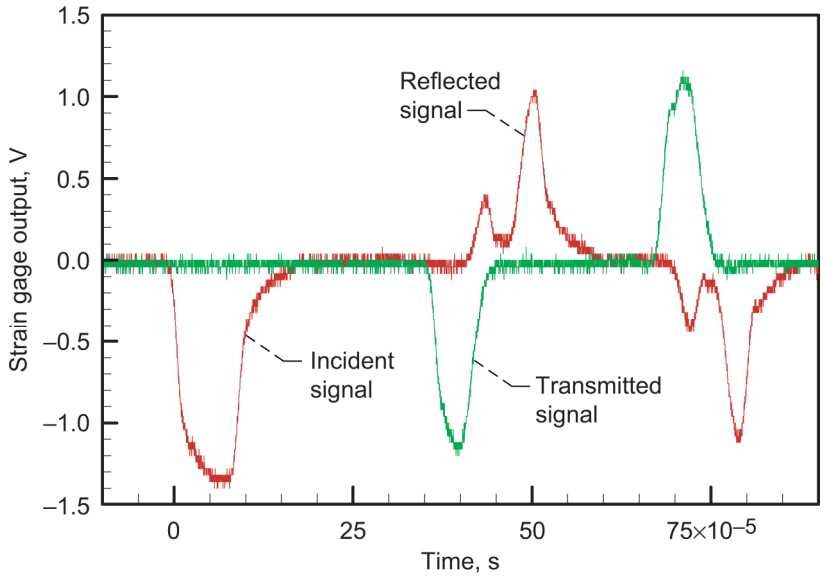

Figure 100.—Strain gage signals for experiment Test 5 on multigrained ice at –30 °C.

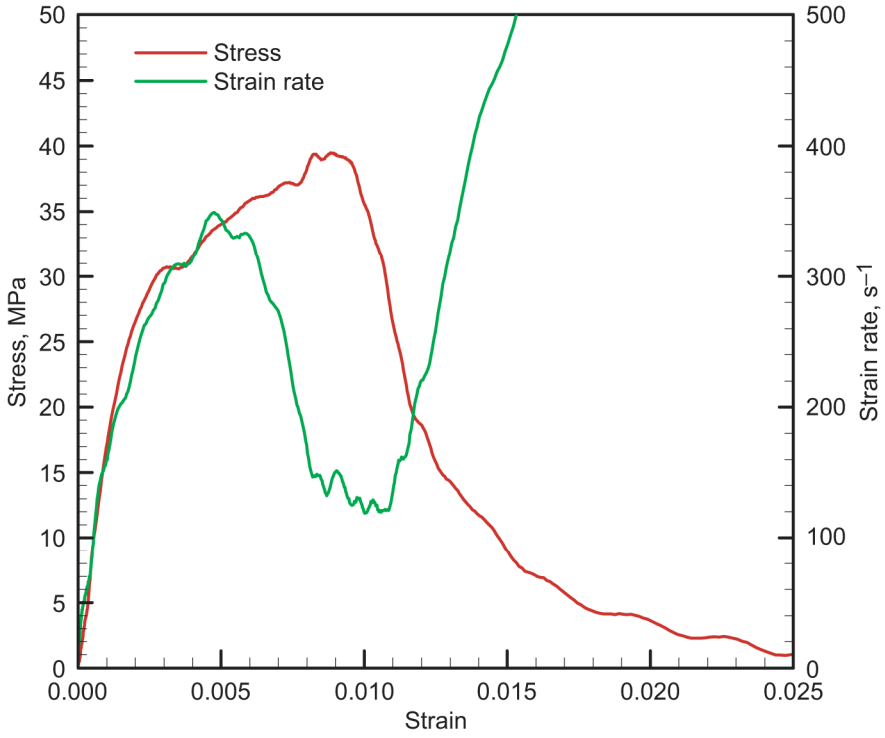

Figure 101.—Stress and strain rate versus strain curves for experiment Test 5 on multigrained ice at –30 °C.

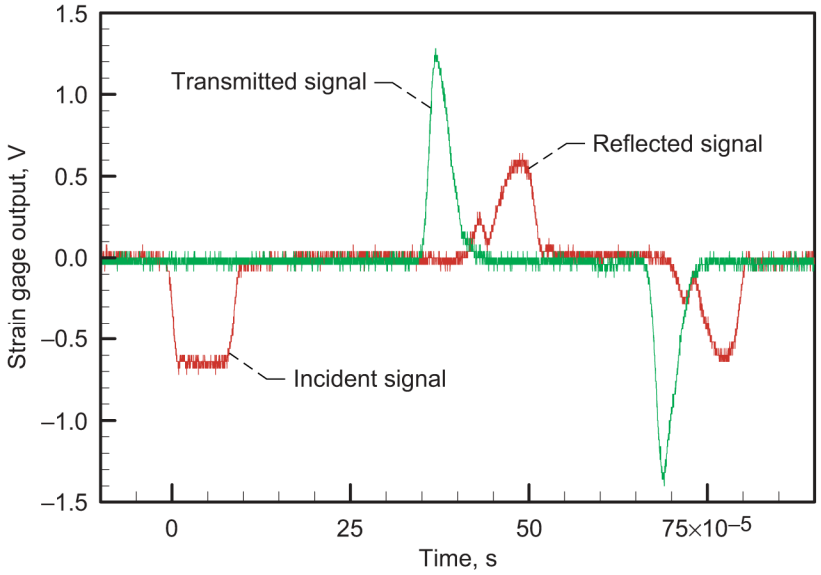

Figure 102.—Strain gage signals for experiment Test 6 on multigrained ice at –30 °C.

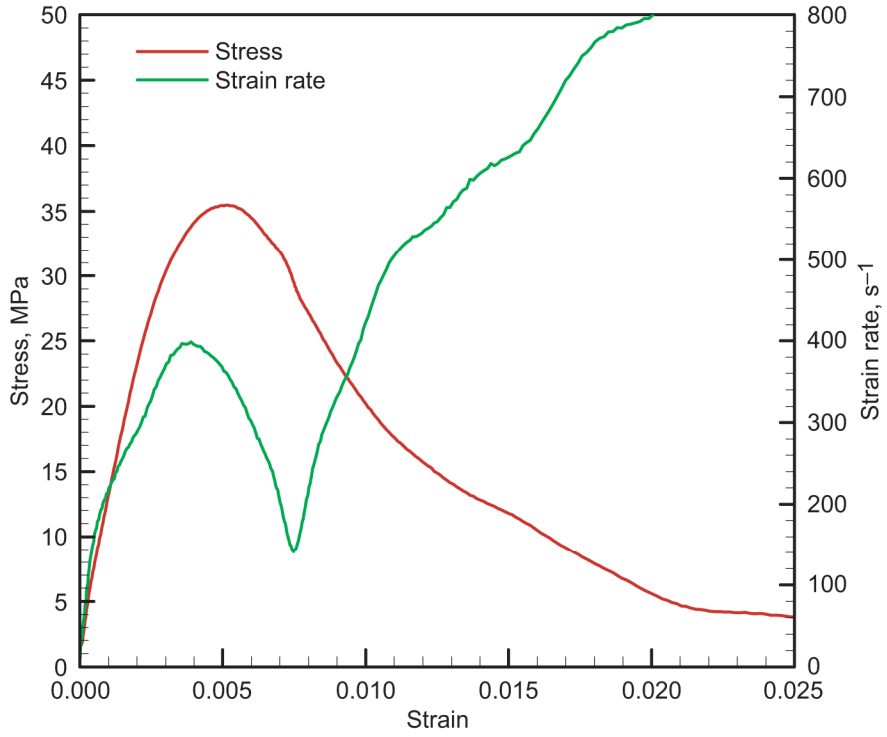

Figure 103.—Stress and strain rate versus strain curves for experiment Test 6 on multigrained ice at –30 °C.

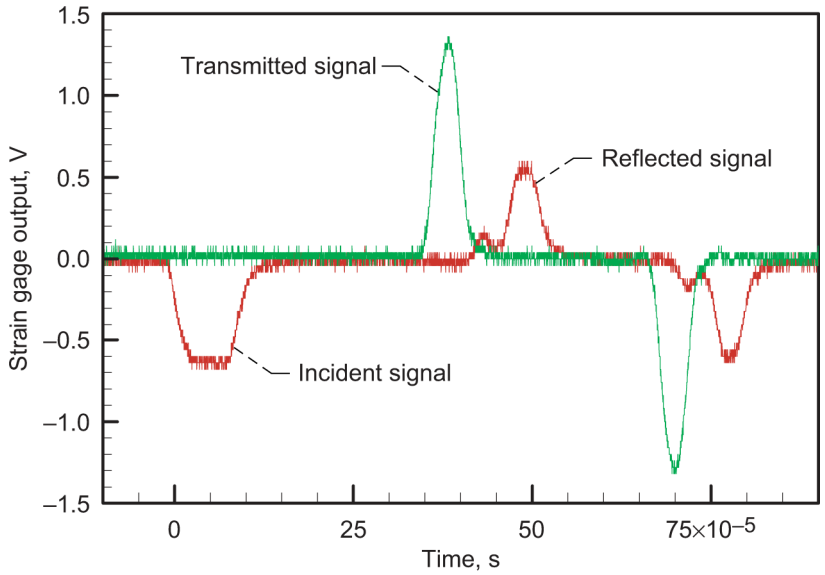

Figure 104.—Strain gage signals for experiment Test 8 on multigrained ice at –30 °C.

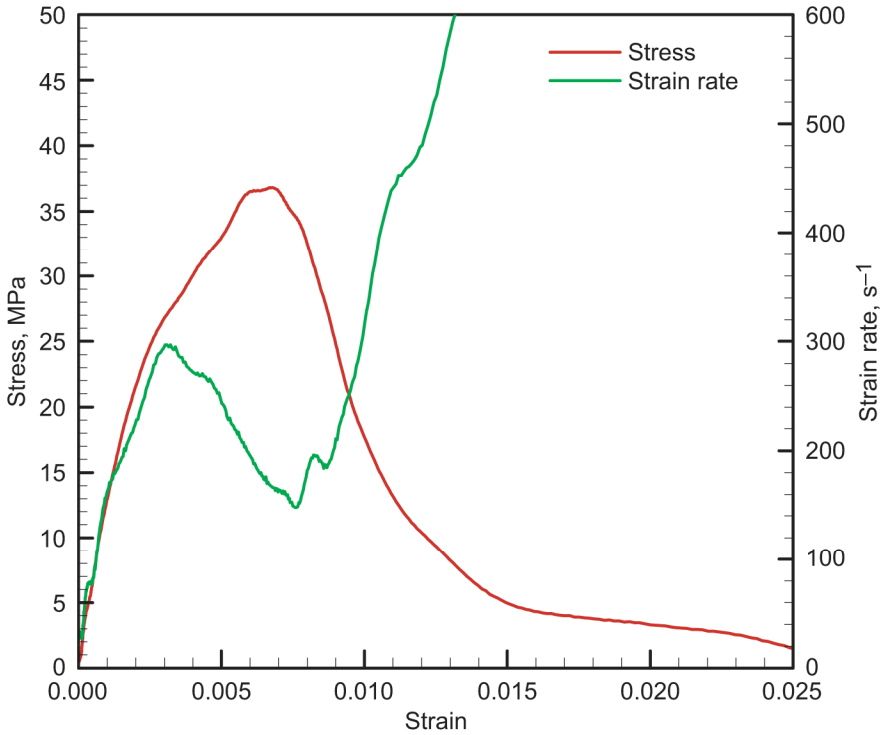

Figure 105.—Stress and strain rate versus strain curves for experiment Test 8 on multigrained ice at –30 °C.

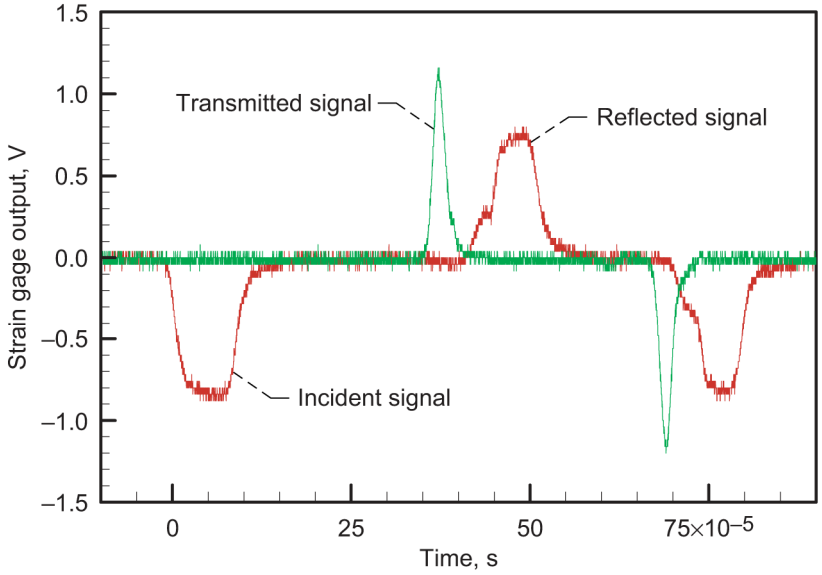

Figure 106.—Strain gage signals for experiment Test 9 on multigrained ice at –30 °C.

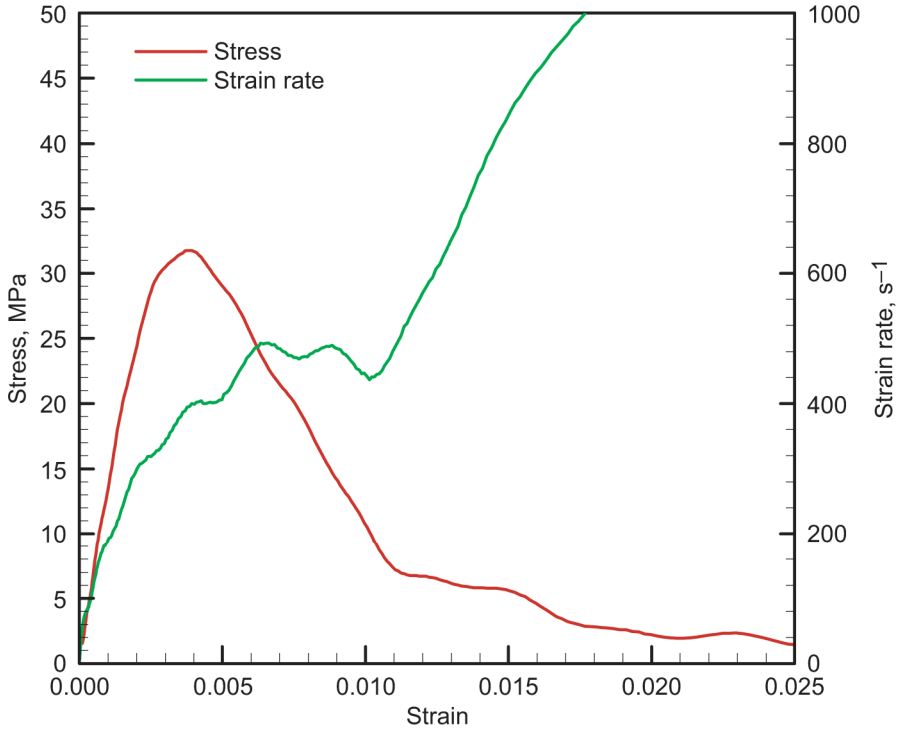

Figure 107.—Stress and strain rate versus strain curves for experiment Test 9 on multigrained ice at –30 °C.

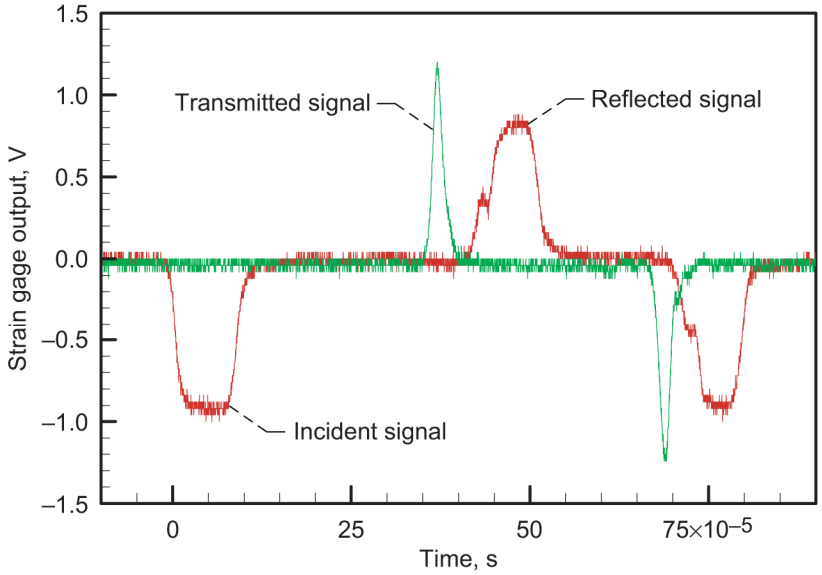

Figure 108.—Strain gage signals for experiment Test 10 on multigrained ice at –30 °C.

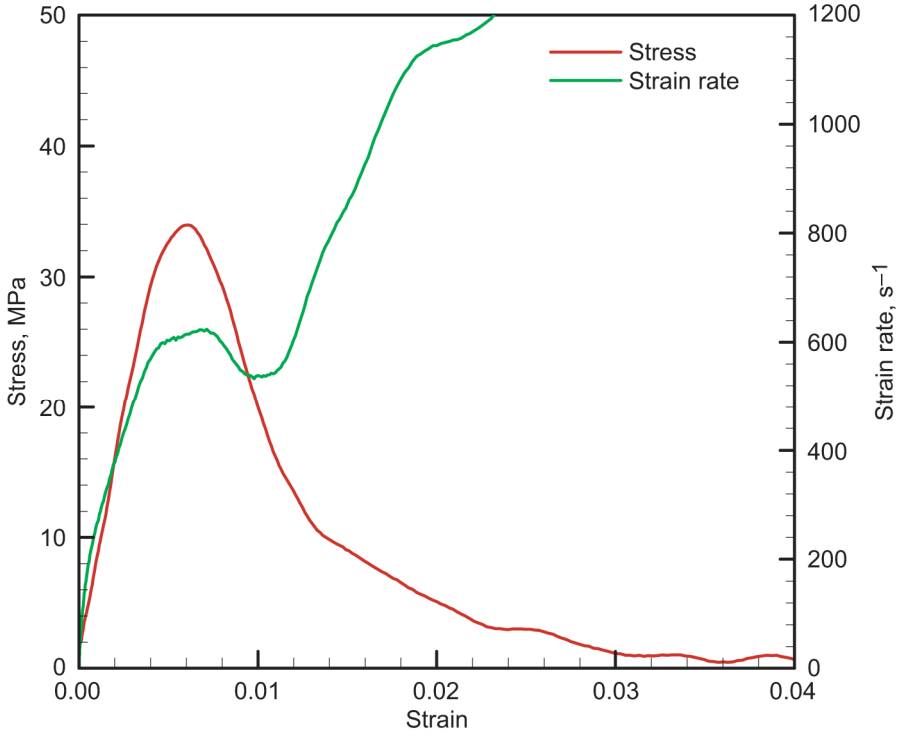

Figure 109.—Stress and strain rate versus strain curves for experiment Test 10 on multigrained ice at –30 °C.

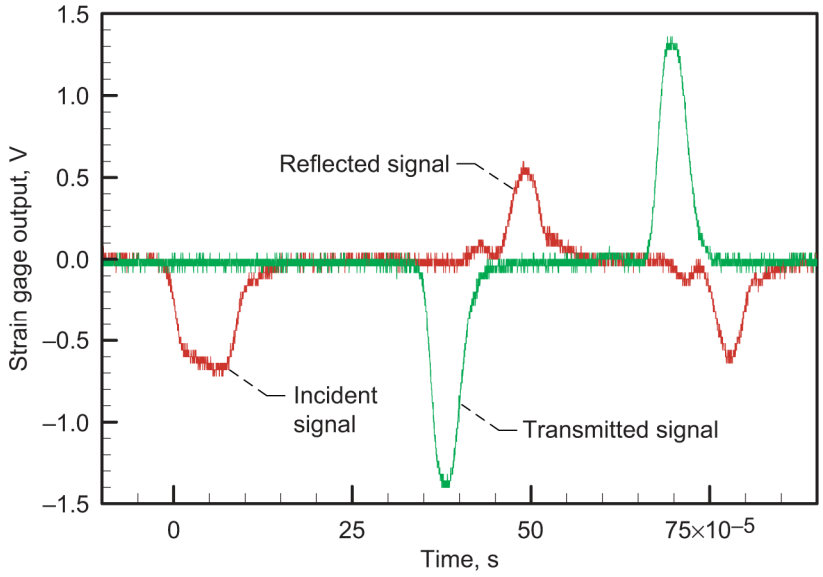

Figure 110.—Strain gage signals for experiment Test 11 on multigrained ice at –30 °C.

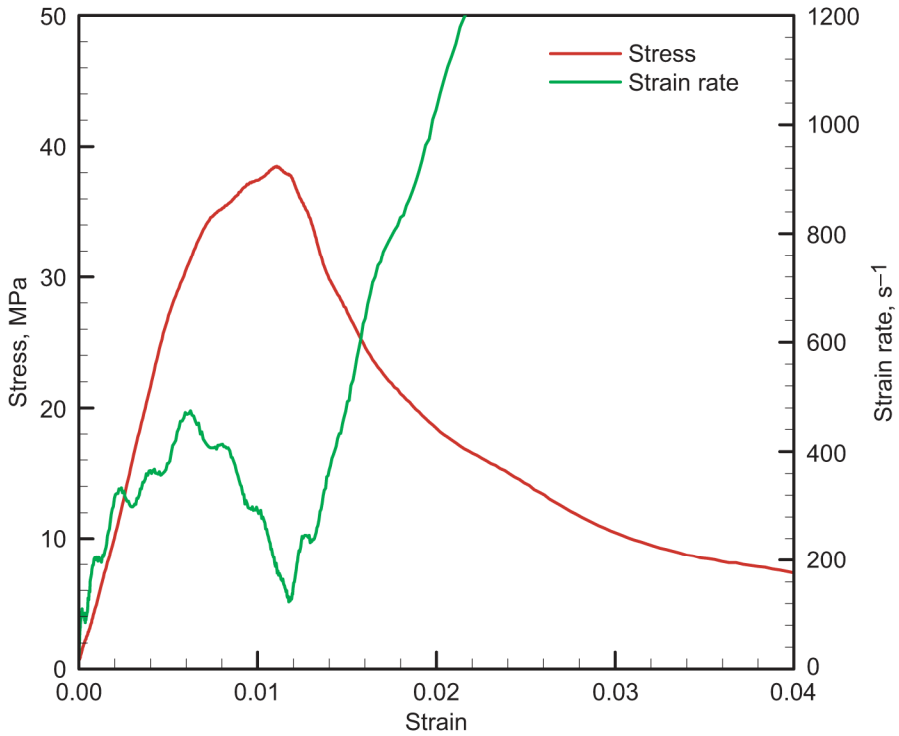

Figure 111.—Stress and strain rate versus strain curves for experiment Test 11 on multigrained ice at –30 °C.

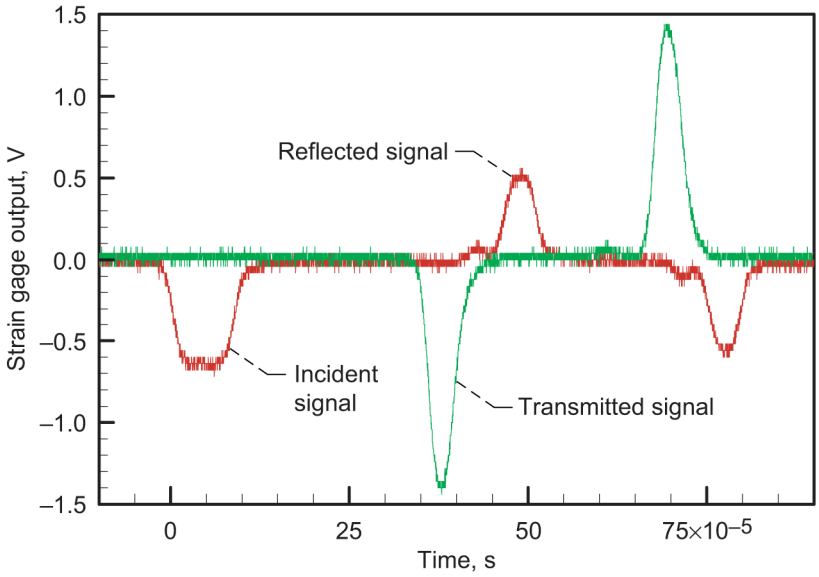

Figure 112.—Strain gage signals for experiment Test 12 on multigrained ice at –30°C.

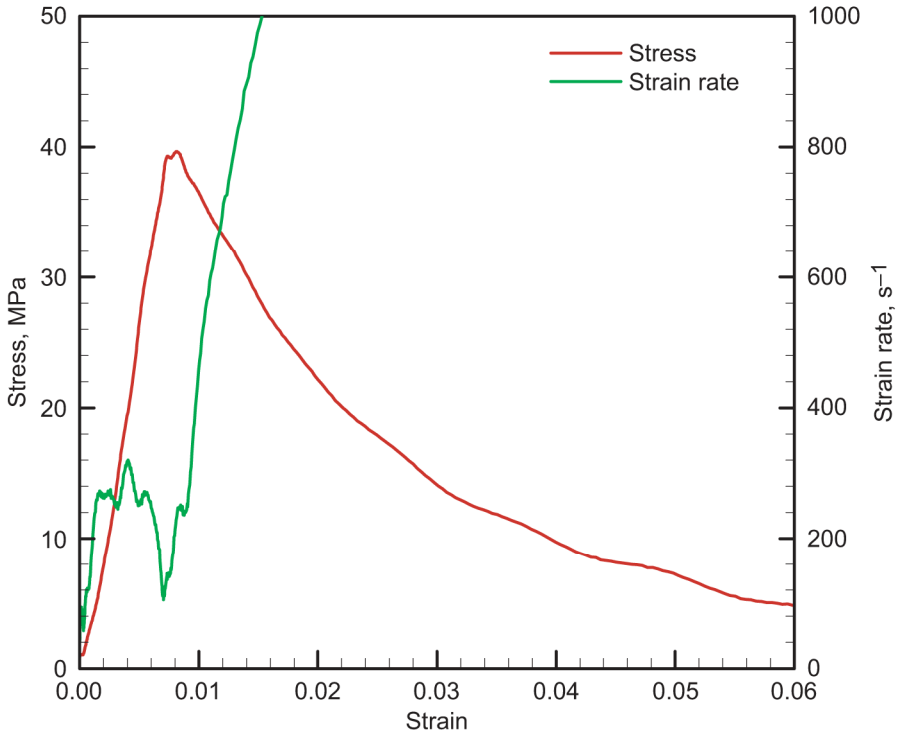

Figure 113.—Stress and strain rate versus strain curves for experiment Test 12 on multigrained ice at –30 °C.

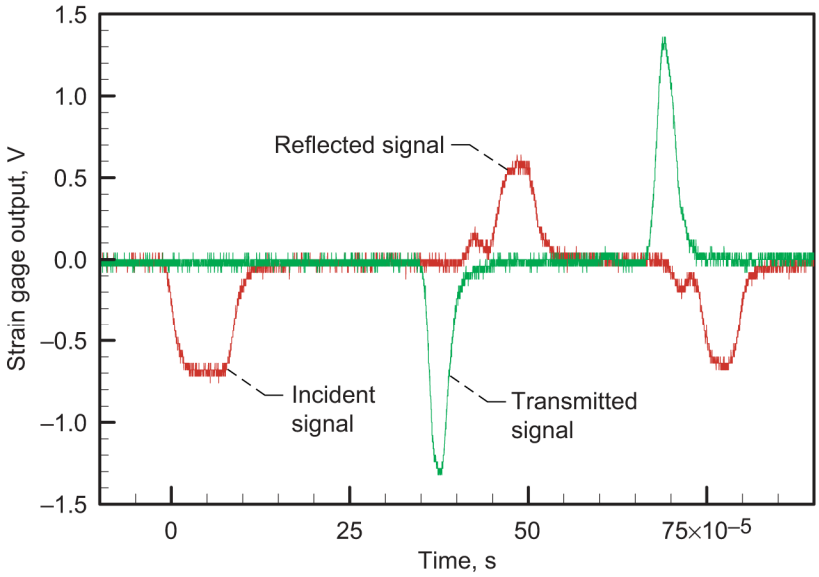

Figure 114.—Strain gage signals for experiment Test 14 on multigrained ice at –30 °C.

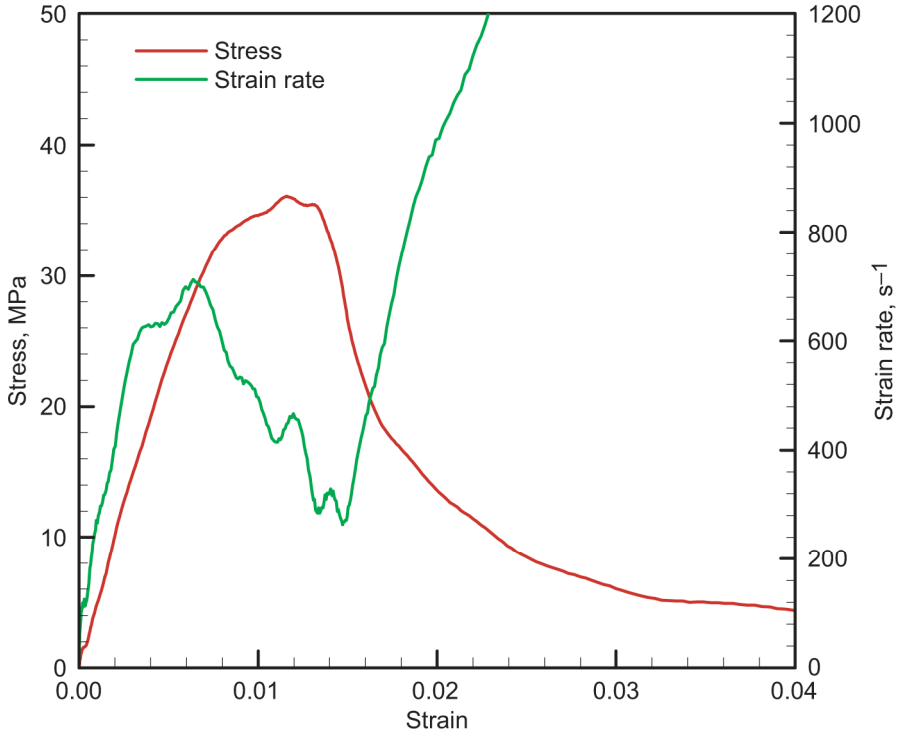

Figure 115.—Stress and strain rate versus strain curves for experiment Test 14 on multigrained ice at –30 °C.

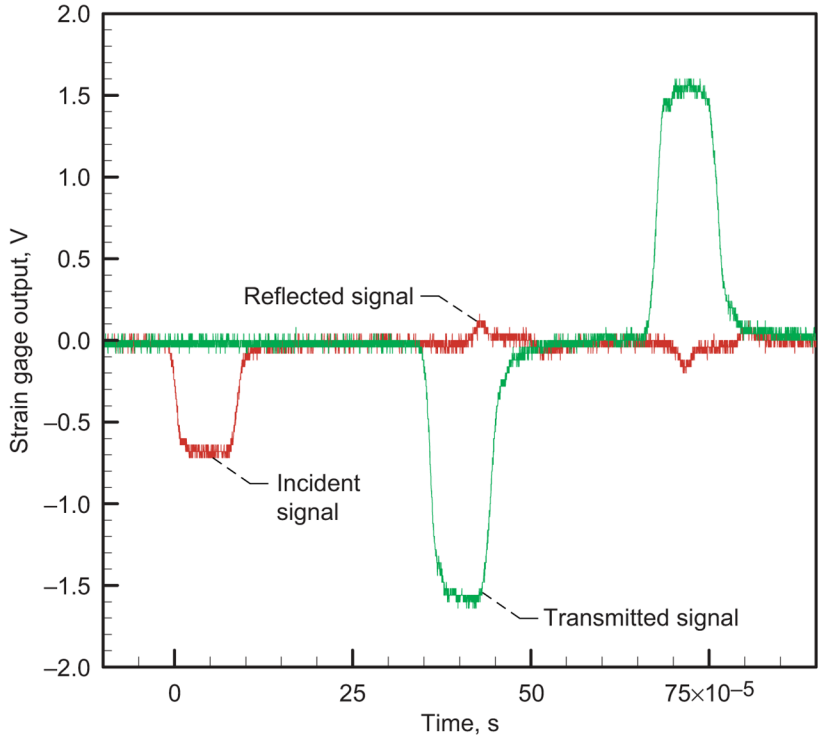

Figure 116.—Strain gage signals for experiment Test 16 on multigrained ice at –30 °C.

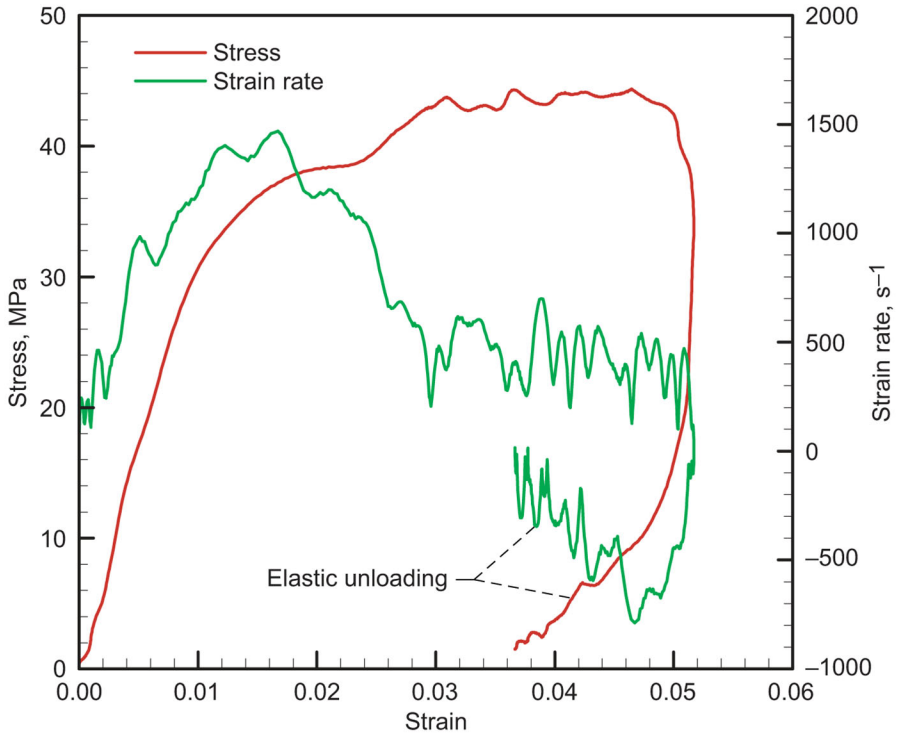

Figure 117.—Stress and strain rate versus strain curves for experiment Test 16 on multigrained ice at –30 °C.

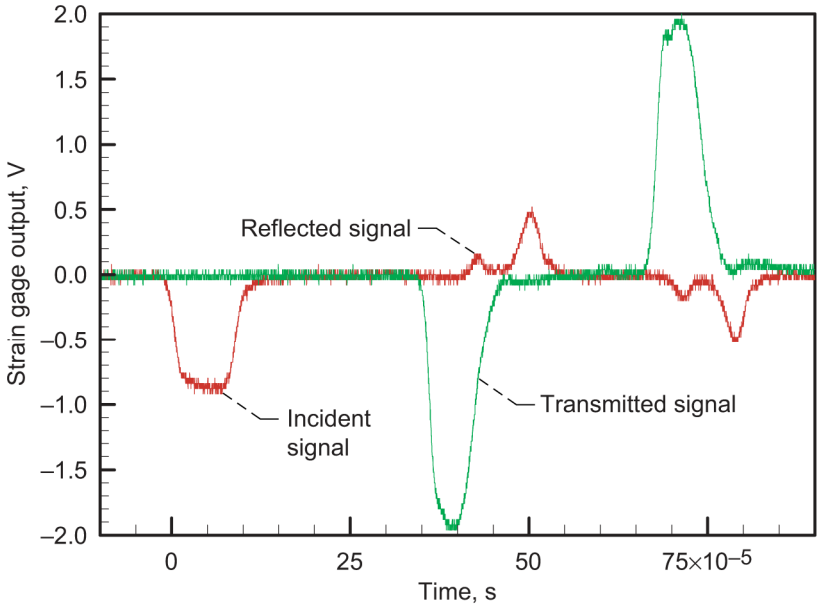

Figure 118.—Strain gage signals for experiment Test 17 on multigrained ice at –30 °C.

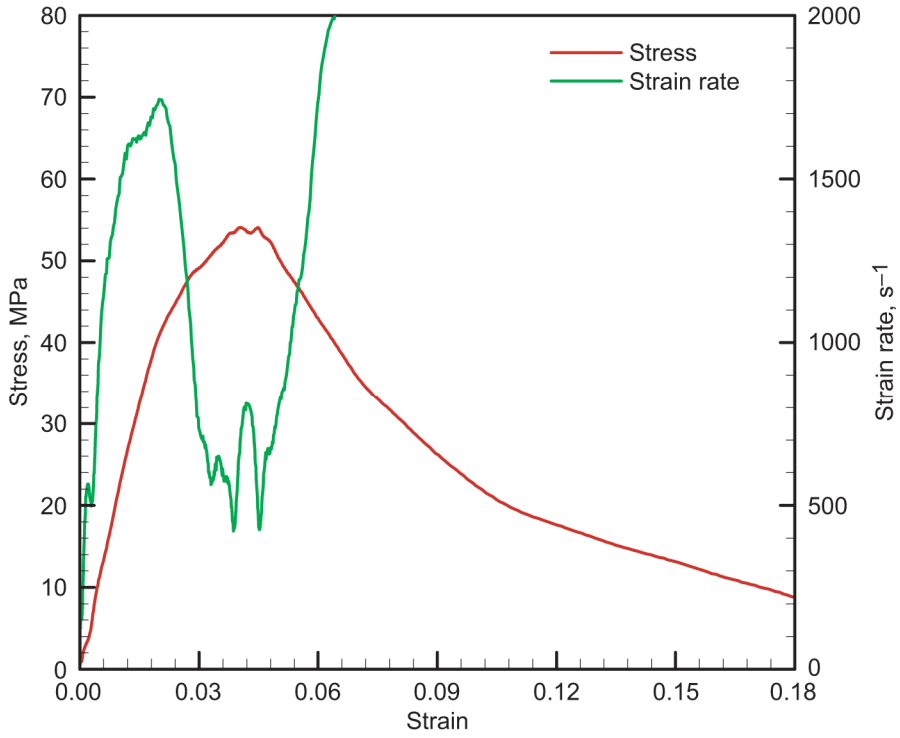

Figure 119.—Stress and strain rate versus strain curves for experiment Test 17 on multigrained ice at –30 °C.

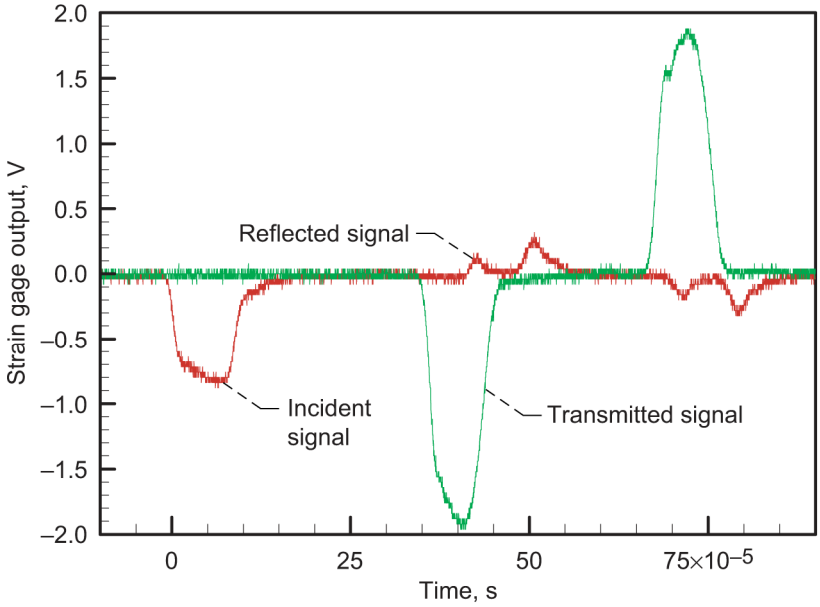

Figure 120.—Strain gage signals for experiment Test 19 on multigrained ice at –30 °C.

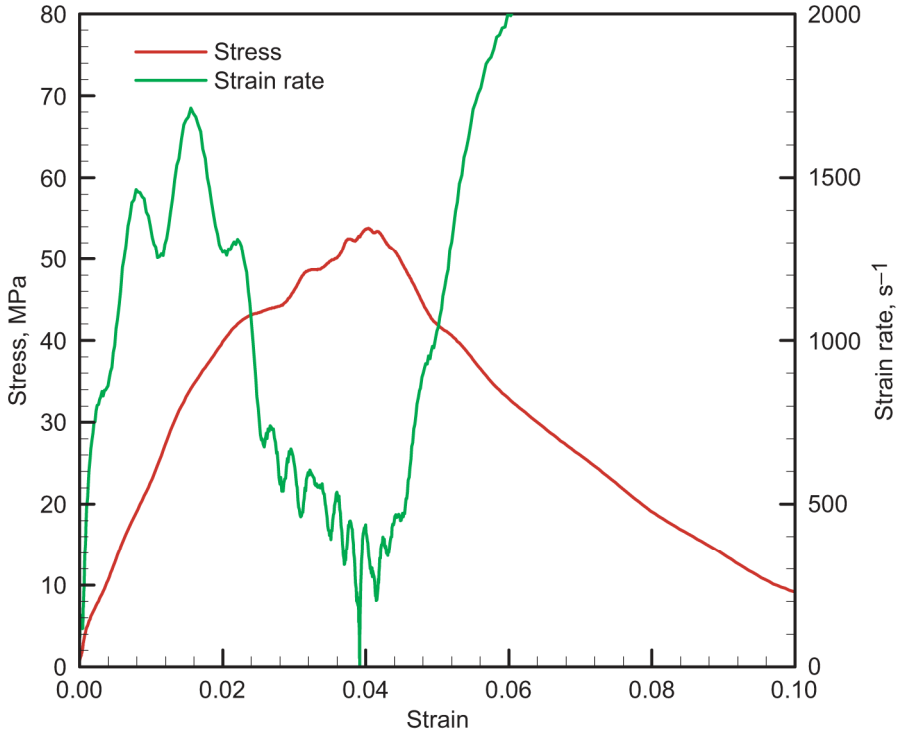

Figure 121.—Stress and strain rate versus strain curves for experiment Test 19 on multigrained ice at –30 °C.

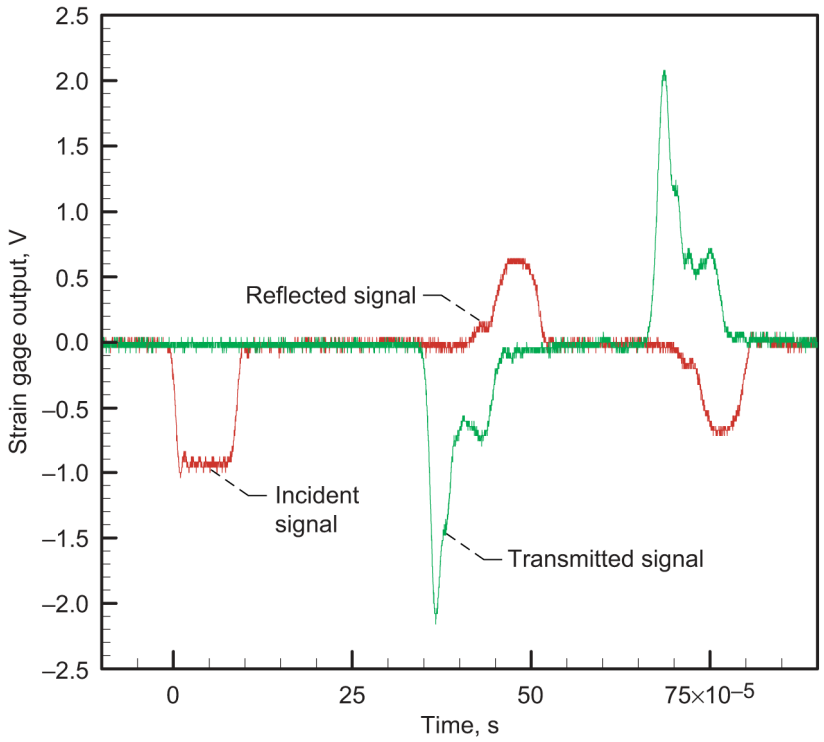

Figure 122.—Strain gage signals for experiment Test 20 on multigrained ice at –30 °C.

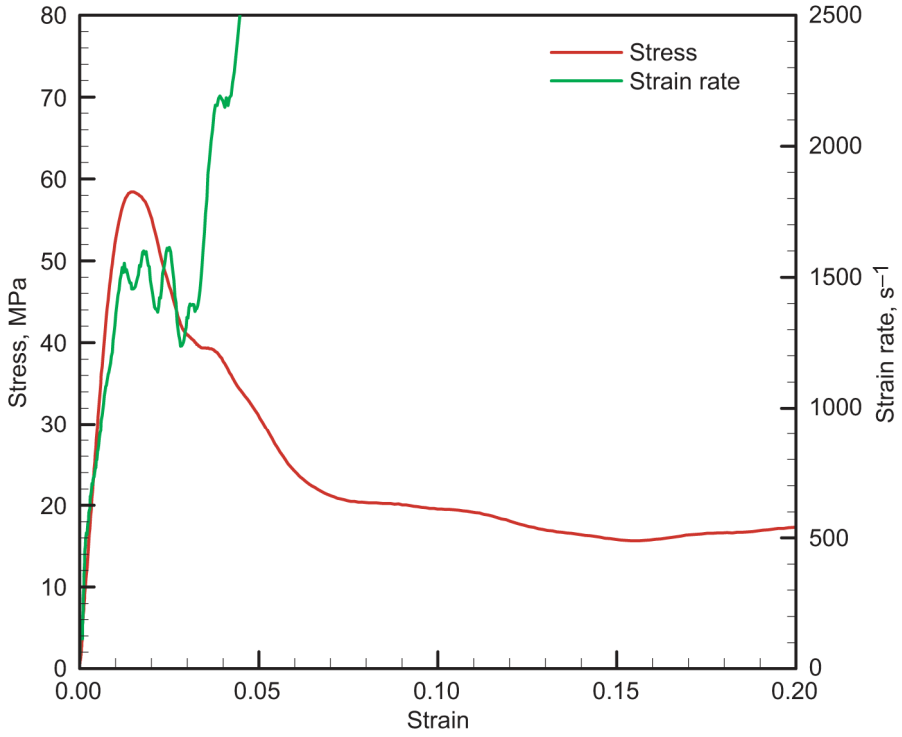

Figure 123.—Stress and strain rate versus strain curves for experiment Test 20 on multigrained ice at –30 °C.

REPORT DOCUMENTATION PAGE

Form Approved
OMB No. 0704-0188

1. AGENCY USE ONLY (*Leave blank*)	2. REPORT DATE	3. REPORT TYPE AND DATES COVERED
	January 2006	Technical Memorandum

4. TITLE AND SUBTITLE

High-Strain-Rate Compression Testing of Ice

5. FUNDING NUMBERS

WBS–22–376–10–30–04

6. AUTHOR(S)

Mostafa Shazly, Vikas Prakash, and Bradley A. Lerch

7. PERFORMING ORGANIZATION NAME(S) AND ADDRESS(ES)

National Aeronautics and Space Administration
John H. Glenn Research Center at Lewis Field
Cleveland, Ohio 44135–3191

8. PERFORMING ORGANIZATION REPORT NUMBER

E–15282

9. SPONSORING/MONITORING AGENCY NAME(S) AND ADDRESS(ES)

National Aeronautics and Space Administration
Washington, DC 20546–0001

10. SPONSORING/MONITORING AGENCY REPORT NUMBER

NASA TM—2006-213966

11. SUPPLEMENTARY NOTES

Mostafa Shazly and Vikas Prakash, Case Western Reserve University, 10075 East Blvd., Cleveland, Ohio 44106; and Bradley A. Lerch, NASA Glenn Research Center. Responsible person, Bradley A. Lerch, organization code RSL, 216–433–5522.

12a. DISTRIBUTION/AVAILABILITY STATEMENT

Unclassified - Unlimited
Subject Category: 27

Available electronically at http://gltrs.grc.nasa.gov

This publication is available from the NASA Center for AeroSpace Information, 301–621–0390.

12b. DISTRIBUTION CODE

13. ABSTRACT ***(Maximum 200 words)***

In the present study a modified split Hopkinson pressure bar (SHPB) was employed to study the effect of strain rate on the dynamic material response of ice. Disk-shaped ice specimens with flat, parallel end faces were either provided by Dartmouth College (Hanover, NH) or grown at Case Western Reserve University (Cleveland, OH). The SHPB was adapted to perform tests at high strain rates in the range 60 to 1400 s^{-1} at test temperatures of –10 and –30 °C. Experimental results showed that the strength of ice increases with increasing strain rates and this occurs over a change in strain rate of five orders of magnitude. Under these strain rate conditions the ice microstructure has a slight influence on the strength, but it is much less than the influence it has under quasi-static loading conditions. End constraint and frictional effects do not influence the compression tests like they do at slower strain rates, and therefore the diameter/thickness ratio of the samples is not as critical. The strength of ice at high strain rates was found to increase with decreasing test temperatures. Ice has been identified as a potential source of debris to impact the shuttle; data presented in this report can be used to validate and/or develop material models for ice impact analyses for shuttle Return to Flight efforts.

14. SUBJECT TERMS

Ice; Compression tests; Strain rate; Microstructure; Space shuttles; Impact damage

15. NUMBER OF PAGES

95

16. PRICE CODE

17. SECURITY CLASSIFICATION OF REPORT	18. SECURITY CLASSIFICATION OF THIS PAGE	19. SECURITY CLASSIFICATION OF ABSTRACT	20. LIMITATION OF ABSTRACT
Unclassified	Unclassified	Unclassified	